1986

A study of the ('2)H(p,2p)n reaction at intermediate energy

Vina Alkesh Punjabi
College of William & Mary - Arts & Sciences

Punjabi, Vina Alkesh

A STUDY OF THE DEUTERIUM(P,2P)N REACTION AT INTERMEDIATE ENERGY

The College of William and Mary in Virginia PH.D. 1986

A STUDY OF THE $^{2}H(p,2p)n$ REACTION AT INTERMEDIATE ENERGY

A Dissertation

Presented to

The Faculty of the Department of Physics

The College of William and Mary in Virginia

In Partial Fulfillment

Of the Requirements for the Degree of

Doctor of Philosophy

---

by

Vina Punjabi

February 1986

APPROVAL SHEET

This dissertation is submitted in partial fulfillment of

the requirements for the degree of

Doctor of Philosophy

Vina A. Punjabi

Vina A. Punjabi

Approved, February 1986

Charles F. Perdrisat

John M. Finn

Herbert O. Funsten

William L. Bynum
Department of Computer Science

Wim T.H. van Oers
University of Manitoba

ABSTRACT

Exclusive cross sections for the $^{2}H(p,2p)n$ reaction at beam energies of 507 and 508 MeV have been measured at various kinematics. The results are compared with the predictions of the impulse approximation and of a calculation of the 6 lowest order terms of a multiple scattering expansion of the t-matrix. At small internal momenta the data are systematically lower than theory. At internal momenta larger than 200 MeV/c a drastic deviation from theory is confirmed. Possible causes for these results are discussed.

ACKNOWLEDGEMENTS

I would like to express deep appreciation to my thesis advisor Professor Charles F. Perdrisat for his guidance, encouragement and instructions during the years of my research.

I would like to thank all the participants in the experiment at TRIUMF, especially Martin Epstein for his continuing interest. Also the staff of TRIUMF for all their help during the experiment.

I also want to thank William Bynum, Mike Finn, Herb Funsten and Wim Van Oers for a critical reading of my thesis and accepting to be on my committee.

I thank the Physics Department for providing me with opportunity to continue my studies in physics in a congenial environment and the William and Mary Computer Center staff for their limitless patience. Also the National Science Foundation for financial support over the last three years.

I appreciate the help and material made available by R.A. Arndt for the NN phase-shifts, Jon M. Wallace for the multiple scattering calculation and Harold Fearing for the NN off-shell amplitudes.

I am very thankful to Murshed Hossain for all his help with my studies and encouragement in difficult times.

I am very much tankful to my husband Alkesh for his encouragement and understanding throughout my graduate studies and for his help in producing some of the figures of my thesis.

Finally, I express my deepest appreciation to my son Parth for having much patience and understanding for a long six years.

TABLE OF CONTENTS

Chapter I

INTRODUCTION

The primary interest in one-nucleon knock-out reactions such as (p, 2p) and (e, e'p) on light nuclei at intermediate energy is to study the single nucleon momentum distribution of a bound nucleon in a nuclear system. Such reactions provide information on the structure of the nucleus and on the interaction of the nucleons in the initial and final states. In the impulse approximation (IA) description the momentum of a nucleon in the nucleus before the interaction, $\vec{q}$, is related to the momentum of the residual nucleus, $\vec{p}_R$, by the expression $\vec{q} = -\vec{p}_R$. According to the original definition of Chew and Wick (Ch-52), the assumption of the IA are I) the incident particle interacts only with a single nucleon at a time, II) the incident wave falling on each constituent is not attenuated and, III) the binding force has a negligeable effect during the interval of strong interaction. As a consequence of these assumptions, the cross section can be factorized in the form (Ja-66)

$$d^5\sigma/d\Omega_3\, d\Omega_4\, dT_3 = K\, d\sigma/d\Omega\, |\Phi(q)|^2 \qquad (1.1)$$

where the labels 3 and 4 refer to the two detected protons (see fig. 1.1), K is a kinematic factor, $d\sigma/d\Omega$ is the cross section for free, nucleon-nucleon or electron-nucleon scattering and Φ (q) is the single nucleon wave function in momentum space. Measuring the cross section allows to obtain the momentum density $|\Phi(q)|^2$ from eqn. (1.1).

However, the IA picture needs to be corrected for effects such as half-off-shell amplitudes, meson exchange currents, rescattering of the two nucleons, final state interactions (FSI) and on- or off-shell nucleon isobars.

The fact that the deuteron is a loosely bound nucleus and that its two constituent nucleons spend a large fraction of their time far away from each other, is favorable for the IA validity in the ^{2}H (p, 2p)n reaction. This reaction offers the simplest possible medium to study differences between experiment and the prediction of a plane wave impulse approximation (PWIA), which can be corrected to second order by estimating rescattering and FSI graphs. Past atomic number 3 this approach becomes too cumbersome.

The results of several investigations of the ^{2}H (p, 2p)n reaction ((Pe-69), (Wi-75), (Fe-76)) have all shown two distinct but definite deviations from the PWIA: (a) at neutron recoil momenta larger than about 200 MeV/c, the momentum distribution stops decreasing with increasing recoil momentum, and (b) at neutron recoil momenta smaller than 200 MeV/c the normalization of the momentum distribution is smaller than expected (see table 1.1) on the basis of realistic deuteron wave functions such as those resulting from the Paris (La-81) and Bonn (Ma-84) potentials even, as in the case of data of Perdrisat et al (Pe-69), after correction for all single NN rescattering graphs and FSI effects (Wa-72).

In contrast with the ^{2}H (p, 2p)n situation, the case of the ^{2}H (e, e'p)n reaction studied by Bernheim et al (Be-81) shows no discon-

tinuity in the shape of the internal momentum distribution, but does show a similar missing strength (see table 1.1). Subsequent calculation of various corrections by Arenhovel (Ar-82) including FSI effects, rescattering, meson exchange and isobaric degrees of freedom have largely eliminated the missing strength, although the data remain symptomatically lower than theoretical predictions for neutron momenta smaller than 50 MeV/c. Recent electron data extend to 500 MeV/c (Tu-84) and 645 MeV/c (Me-84).

TABLE 1.1

Ratios R Of Experimental to Theoretical Momentum Densities in Momentum Range 0 to 200 MeV/c

Reaction	Incidents energy (MeV)	Max. Recoil (MeV/c)	R	Reference
(p, 2p)	600	370	0.84±0.04 (≤25%)*	Perdrisat et al. (Pe-69)
(p, 2p)	585	425	0.87 (unknown)	Witten et al. (Wi-75)
(p, 2p)	800	350	0.89±0.04 (±10%)	Felder et al. (Fe-76)
(e,e'p)	500	340	0.82±0.02 (±10%)	Bernheim et al. (Be-81)
(p, 2p)**	508	674	0.93±0.004 (±1.8%)	Present experiment

*Systematic uncertainty.

**In this case the Paris momentum density is used; all other data are being compared to the Hulthen density; the latter density is smaller than the former by 1% at q = 0.

Breakup of the deuteron by virtual photons in electron scattering leads to a two nucleon continuum state. In the (p, 2p) reaction the hadronic probe introduces a third nucleon in the final state, thus, on the one hand considerably increasing the difficulty of obtaining the "true" internal momentum distribution of the deuteron, but, on the other hand offering a unique environment to study half-off-shell scattering. The phase space available to the three nucleons in a (p, 2p) reaction offers the possibility to select conditions favoring one particular process. For example, strong FSI effects are expected and have been seen (Fu-73) when the relative energy of one pair becomes very small. In fact the data of Witten et al (Wi-75) and Felder et al (Fe-76) are invariably in the FSI region for large neutron recoil momenta. In those experiments various recoil momenta were obtained by changing the energy sharing among the two protons, at angle pairs for which a recoilless reaction is possible. However, the same recoil momenta can be obtained away from the FSI region. The data of Perdrisat et al (Pe-69) were of this type. In that experiment various recoil momenta were obtained by changing the angles of the two protons symmetrically with respect to the incident beam direction. However, in these data the invariant mass of one of the nucleon pairs becomes equal to $(m_N + m_\Delta)$ at large recoil momenta, a situation most favorable for virtual excitation of the $\Delta(1232)$.

The goals of the present experiment were defined as: (a) to reexamine the (p, 2p) results obtained previously at various laboratories, (b) to obtain cross section data for small neutron recoil momenta with as small as possible a systematic uncertainty, and (c) to

explore regions of three-body phase space in which virtual Δ excitation should become predominant.

In this work the results of a ^{2}H(p, 2p)n experiment performed at the TRIUMF cyclotron are presented. We have obtained data over a large range of neutron recoil momenta, and investigated the quasifree region with symmetric and asymmetric kinematics for the two protons. The data in this region have a statistical uncertainty as low as 0.4%. To minimize the systematic uncertainty we measured the elastic pp cross section using the same experimental set up, replacing deuterium by hydrogen in the same target cell; the incident beam energy and the angles and final energies of the two detected protons were nearly the same as for the quasifree (p, 2p) data. We determined the target thickness by comparing our measured pp cross section for 90° center-of-mass to the average of recent pp measurements at 500 MeV (Ch-82) and 515 MeV (Ot-84) of 3.44±0.062 mbsr^{-1} (CM). Therefore, the systematic uncertainty of the (p, 2p) cross section data will be no less than the 1.8% from the pp cross section.

There are three sets of data for two different kinematics where zero recoil momentum is possible kinematically. The data for symmetric angle pair 41.4° were obtained and analyzed with two different solid angles, $\Delta\Omega_3$, 0.528 msr and 0.107 msr and this is where we have the best statistics. We did not have enough statistics to do so for the asymmetric angle pair 30.1° - 53.75°. The recoil range covered for these data is 12 to 80 MeV/c.

There are three other symmetric angle pairs, 38.1°, 44.1° and 47.1° where the data are in the small neutron recoil region. The asymmetric angle pairs 41.4° - 50.°, 41.4° - 57.° and 41.4° - 68.° cover the recoil momenta from 78 to 383 MeV/c. The asymmetric angle pairs 30.1° - 44.°, 30.1° - 61.° and 30.1° - 68.° give recoil momenta starting at 60 MeV/c and up to 220 MeV/c.

We measured recoil momenta as large as 674 MeV/c for the 66.° symmetric angle pair, where the minimum possible recoil was 650 MeV/c. The data for 57.° symmetric angle pair ranged from 362 to 406 MeV/c. The data for symmetric angle pairs 50.° and 52.° cover the recoil region 173 to 299 MeV/c. At these very large recoil momenta, the pp interaction is no longer dominant; the np interaction contributes about as much.

For neutron recoils larger than approximately 200 MeV/c, the IA prediction no longer describe the data. The discrepancy becomes increasingly large at large recoils. Other processes like rescattering, FSI and isobar excitation become predominant. Off-shellness also is large when the internal momentum is so large. We have done a calculation for the rescattering of the projectile with the ejected or the residual nucleon, and FSI of the two deuteron constituents based on a previous calculation by Wallace (Wa-72). This calculation includes 6 Feynman diagrams, two for single scattering pp and np, two for rescattering and two for FSI (see fig. 4.1 and 4.2).

In this work, the cross section results are used to determine the PWIA momentum distribution $| \Phi (\vec{q}) |^2$ using equation 1.1, because

this is the standard method of presenting (p, 2p) results. For the small recoil data, the comparison with the theoretical expectation when all 6 Feynman diagrams are included, is presented as the ratio of the experimental - to the theoretical cross sections; the input to the theoretical calculations are the Paris potential deuteron wave function and the NN phase-shifts from the VPI group. For the large recoil data, we present the "effective" theoretical momentum distribution resulting from the calculation (of the 6 Feynman diagrams), which one obtains by using equation (1.1) with the results of the calculation.

Chapter II describes the experimental setup. Chapter III contains the description of the data analysis. Chapter IV will give the details of the rescattering and FSI calculation. In Chapter V we present the results of the experiment and discuss them. The conclusion closes the work.

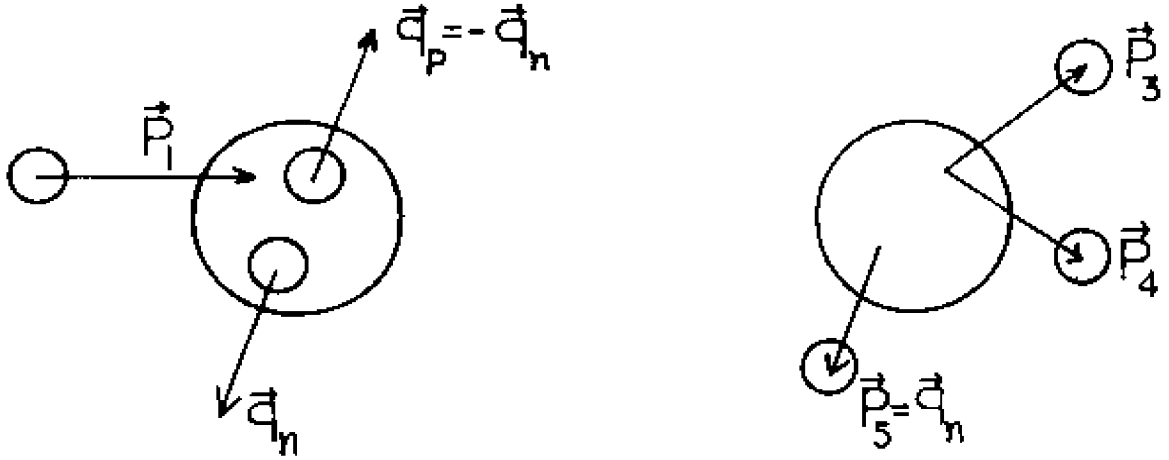

FIGURE 1.1

Chapter II

EXPERIMENTAL SETUP

2.1 INTRODUCTION

This chapter describes the experimental setup used to study the reaction $^{2}H(p, 2p)n$. The experiment was performed in two parts; one part (1983) restricted to symmetric angle pairs, the second part (1984), included symmetric and asymmetric angle pairs. Both parts were done at the TRIUMF Cyclotron using proton beams of 507 MeV (1983) and 508 MeV (1984) at beamline 4B. Fig. 2.1 shows the TRIUMF facility and in particular, beamline 4B. Section 2.2 will give the relevant proton beam characteristics and 2.3 will describe the liquid ^{2}H and ^{1}H target.

We detected two protons in coincidence, on the right hand side (RHS) relative to the incident beam with a counter telescope, and on the left hand side (LHS) with the Medium Resolution Magnetic Spectrometer (MRS). Section 2.4 and 2.5 will describe the detection system on both sides. The electronics and logic will be presented in section 2.6 for the MRS and section 2.7 for the RHS and coincidence. Section 2.8 contains the description of the data acquisition system.

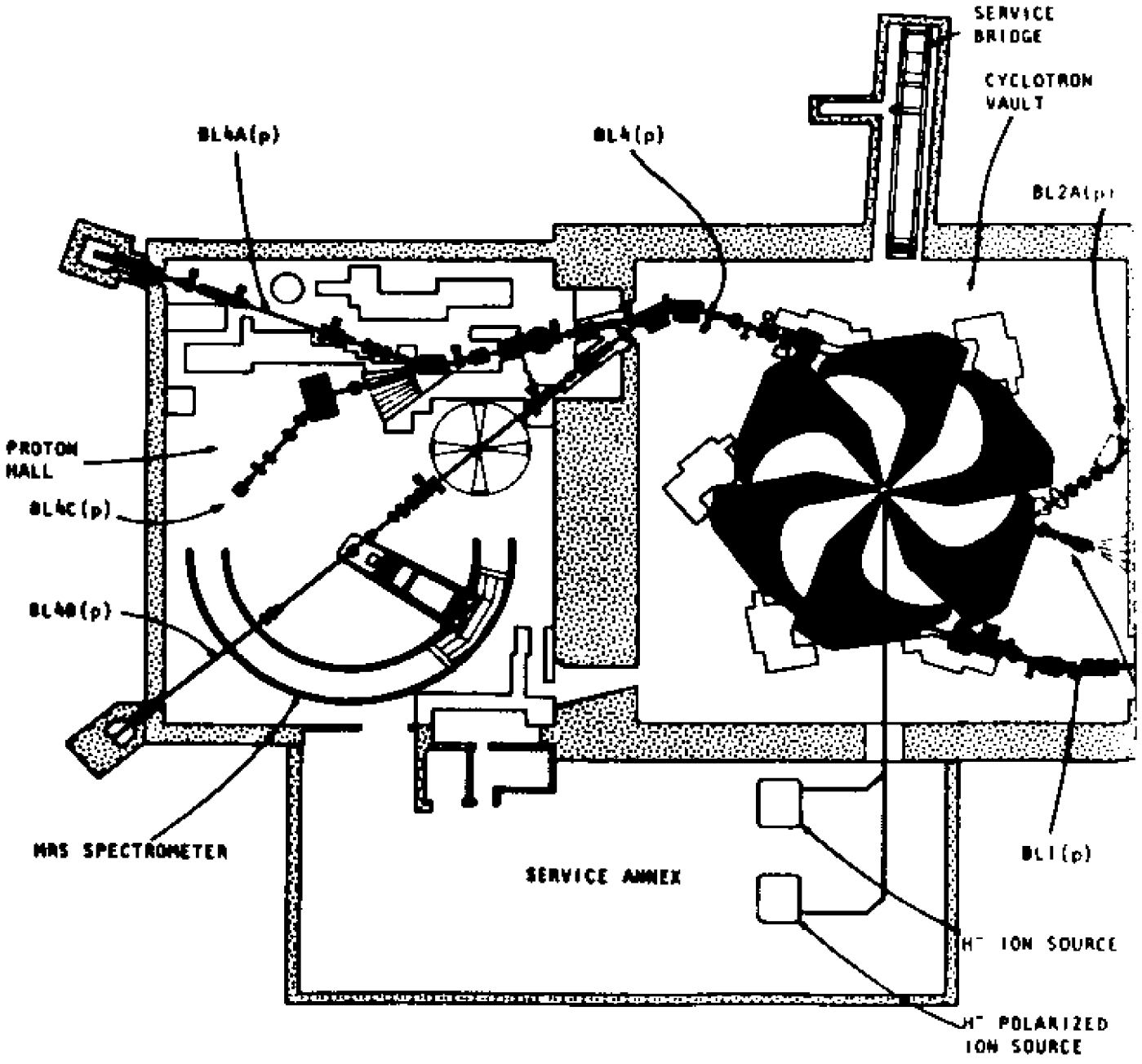
SERVICE BRIDGE
CYCLOTRON VAULT
BL4A(p)
BL4(p)
BL2A(p)
PROTON HALL
BL4C(p)
BL4B(p)
HRS SPECTROMETER
SERVICE ANNEX
BL1(p)
H⁻ ION SOURCE
H⁻ POLARIZED ION SOURCE

FIGURE 2.1

2.2 PROTON BEAM

The accelerator at TRIUMF is a six sector isochronous cyclotron which accelerates H^- ions. Two proton beams independently variable in energy between 183 MeV and 520 MeV can be extracted simultaneously using two stripping foils of carbon or aluminum. The beam is on for 5 ns (nanosecond) every 43 ns, so the microscopic duty cycle is approximately 11%. Beam spot at target is typically 0.4 to 0.5 cm diameter and the beam energy spread is ~1MeV FWHM. The typical beam currents used were between 0.1 nA to 10 nA. The beam intensity was monitored using a secondary electron emission monitor (SEM) and a Faraday cup (for part of the experiment). The beam spot was checked every few hours throughout the experiment by reducing the current and inserting the beam profile monitors and a fluorescent screen and viewing it on closed circuit TV.

2.3 TARGET CELLS

A cryogenic target cooled with a Helium refrigerator, with two identical target cells which can be filled simultaneously with deuterium and hydrogen, has been used for this experiment. Fig. 2.2 shows the cryostat assembly. The system of two identical cells has been developed and built at Technische Hogeschool, Delft (Se-84) so as to fit inside an existing liquid ^{4}He cryostat (Go-78). A fluorescent ZnS screen, used to monitor the beam spot during the experiment is attached to the tail section. The entire cryogenic system is fitted into a hydraulic positioning mechanism used to raise, lower and rotate the cryostat so

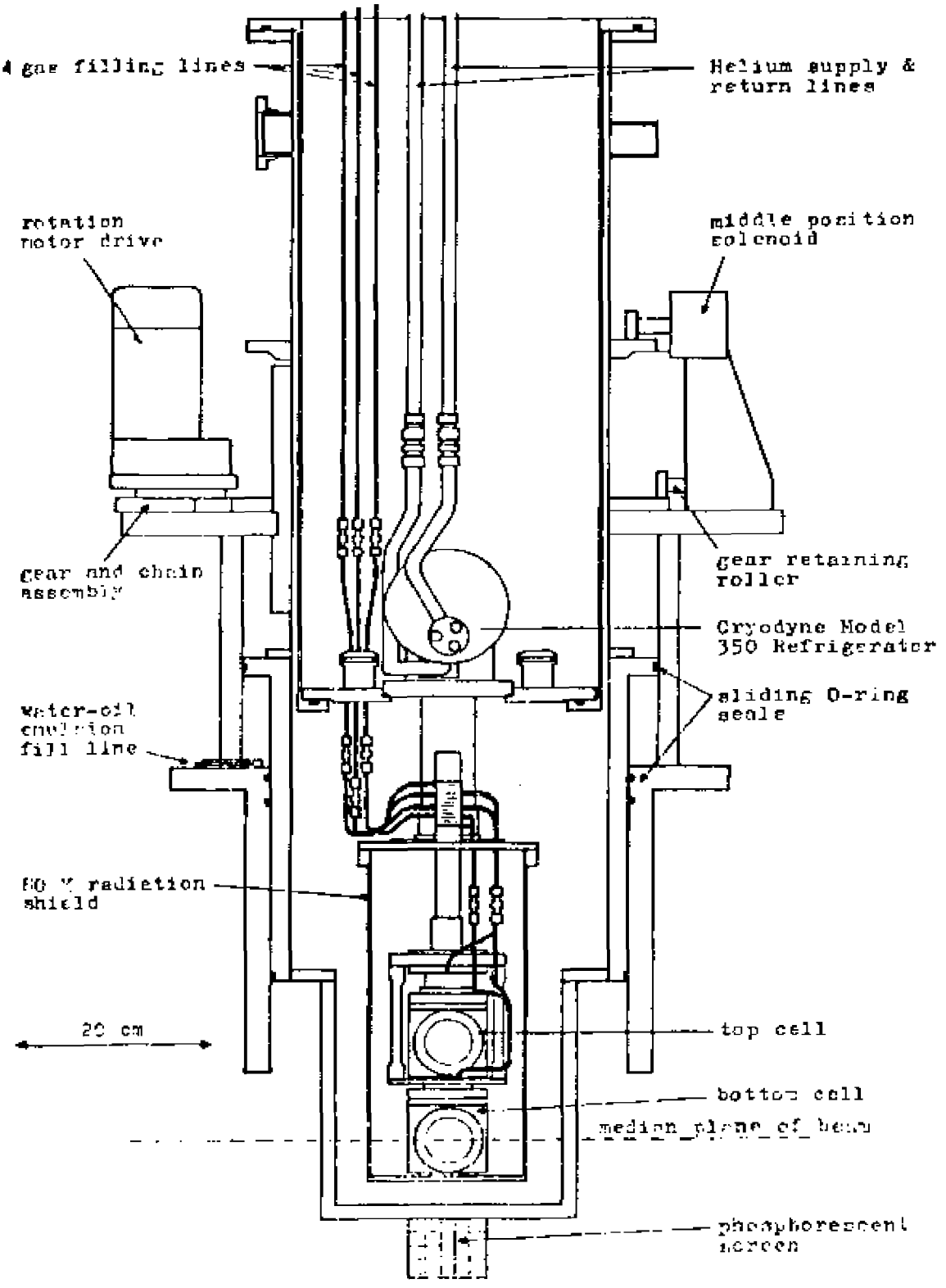
4 gas filling lines
Helium supply & return lines
rotation motor drive
middle position solenoid
gear and chain assembly
gear retaining roller
Cryodyne Model 350 Refrigerator
sliding O-ring seals
water-oil emulsion fill line
80 K radiation shield
20 cm
top cell
bottom cell
median plane of beam
phosphorescent screen

FIGURE 2.2

that either one of the two target cells, or the fluorescent screen is positioned in the beam with the desired orientation. The entire operation of the positioning mechanism is remotely controlled.

Two gas filling lines were available to each cell to avoid blockage in case of condensation of the gas in one of the lines. The target frame was 55 mm diameter and 6 mm thick with windows made from stainless steel (thickness 0.025 mm). This design of the target frame made it possible to make measurements up to $\pm 75^{\circ}$ for the two outgoing particles. The actual target thickness of the target cell was more than 6 mm due to the bulging of the foils. How the target thickness was determined will be discussed in section 3.4.

2.4 COUNTER TELESCOPE

For the 1983 measurements we had only one counter telescope, and it was employed on the RHS of the incident beam. The counter telescope contained a solid angle defining plastic scintillator counter of 6.35 cm diameter and 0.32 cm thick, a NaI(Tl) crystal of 12.7 cm diameter and 15.2 cm deep, a delay line wire chamber (DLC) and a Cu absorber when needed. The distance to the plastic scintillator was 195.7 cm from the scattering center.

For the 1984 measurements six counter telescopes were used, all on the RHS of the incident beam; they are numbered 1 to 6 as shown in figure 2.3. Telescope 1 included an 8.0 cm diameter and 0.32 cm thick solid angle defining plastic scintillator counter ΔE_R; the remaining five had 6.35 cm diameter and 0.32 cm thick scintillators.

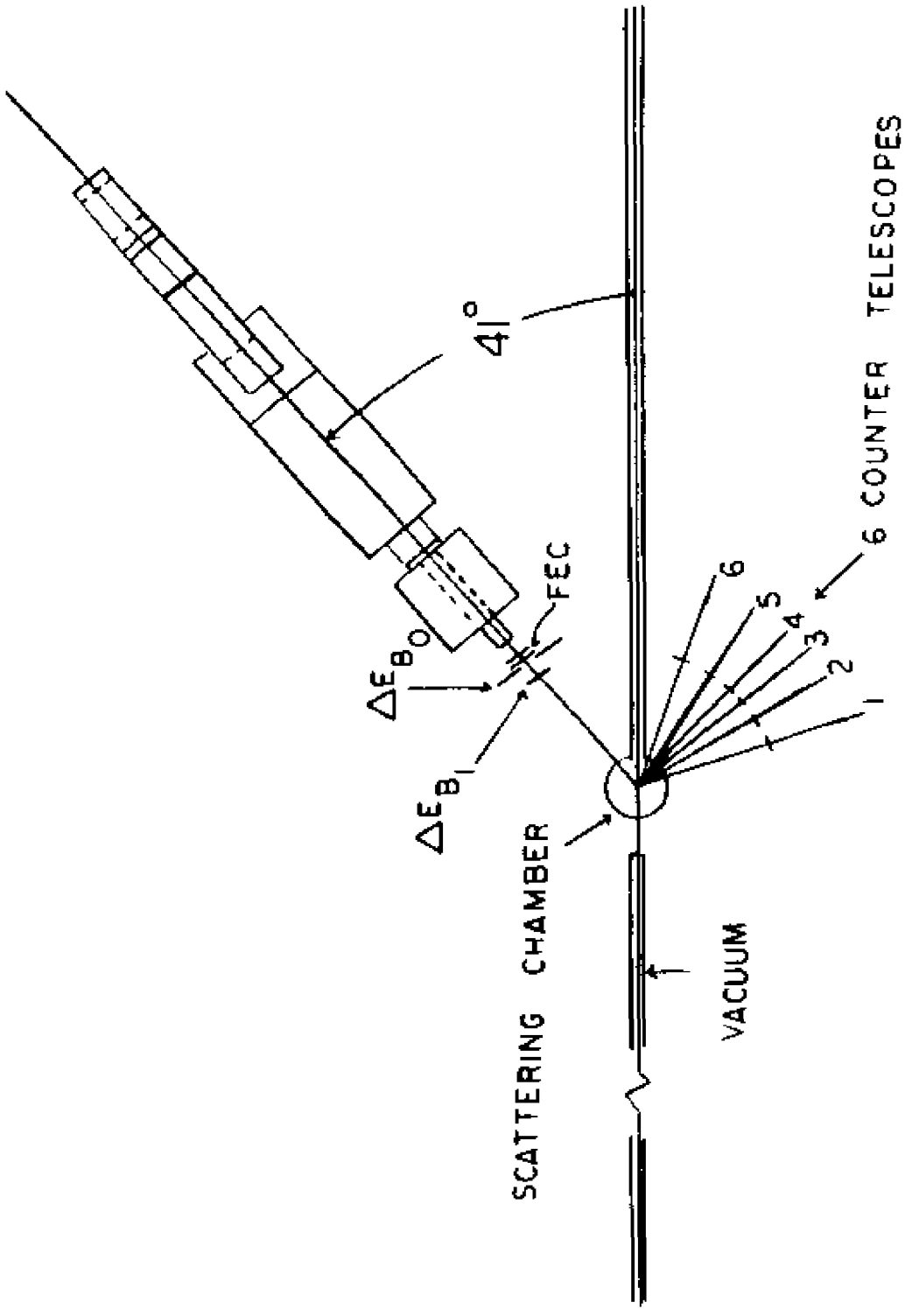
41°
6 COUNTER TELESCOPES
6
5
4
3
2
1
FEC
ΔE_B0
ΔE_B1
SCATTERING CHAMBER
VACUUM

FIGURE 2.3

The counter telescopes 1 to 4 had a NaI(Tl) crystal E of 15.2 cm deep and 12.7 cm diameter, the remaining two were 7.6 cm deep and 12.7 cm diameter. The counter telescope 1 also included a delay line chamber (DLC). The distances to all counters from the scattering center was 200 cm, except for 1, for which the distance was 205.7 cm.

2.5 THE MEDIUM RESOLUTION SPECTROMETER

Fig. 2.4 shows the vertical section of the Medium Resolution Spectrometer (MRS). The MRS consists of two optical elements, a quadrupole singlet followed by a dipole magnet, three multi wire proportional chambers (MWPC) (for 1983), drift chambers (for 1984) and plastic scintillator detectors above the dipole. The quadrupole was set for point-to-point focusing in the non-bend plane. The quadrupole can be positioned between 1 and 2 meter from the target center. The dipole has a nominal 60° bend angle and is strongly focusing in the bend plane; together with the quadrupole the system produces an image of the target on the focal plane.

In the 1983 experiment three sets of MWPC (St-81) gave the coordinates (X_o, Y_o), (X_t, Y_t) and (X_b, Y_b). (X_o, Y_o) is located in front of the quadrupole, 166.7 cm from target center. (X_t, Y_t) and (X_b, Y_b), called top and bottom MWPC, are located above the dipole with 1 meter distance between them. The angle between the focal plane and the first MWPC at the exit of the dipole magnet was 66°. All three wire chambers are perpendicular to the central trajectory. The MWPC's have 2mm spacing between wires. Following the top MWPC there were two long

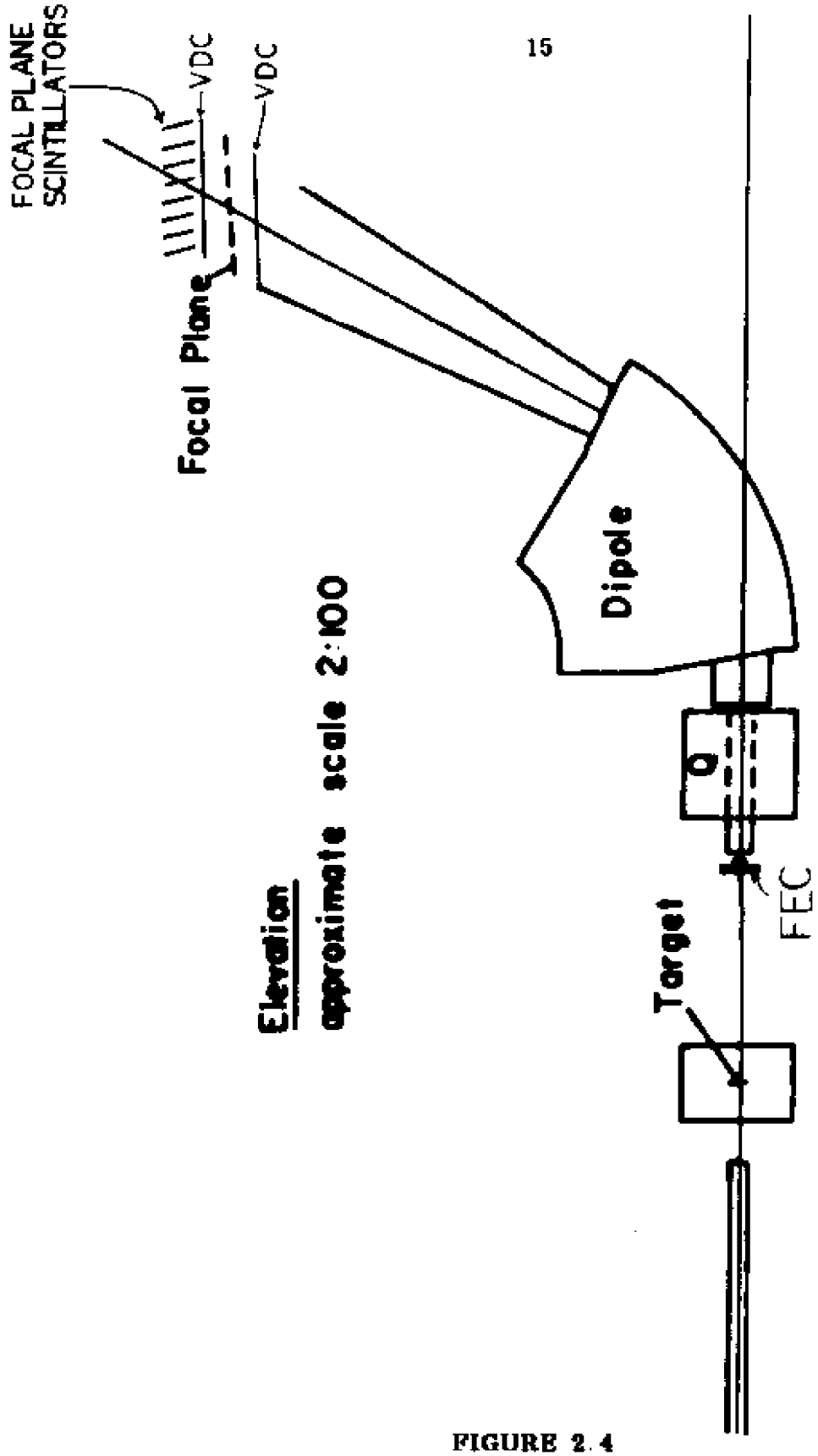
FOCAL PLANE SCINTILLATORS
VDC
VDC
Focal Plane
Dipole
Q
FEC
Target
Elevation
approximate scale 2:100

FIGURE 2.4

scintillator paddles each 12.5 cm wide, 100 cm long and 2.5 cm thick.

For the 1984 measurements we had three sets of drift chambers. One set of chambers was located in front of the quadrupole. These front end chambers (FEC's) have two wire planes (16 wires each, spaced by 5mm) per axis (X and Y) and one TDC per wire. Measurements of the drift times allow to calculate the position of the intersection interpolating between wires. Most events trigger one TDC per plane. The FEC's are low pressure drift chambers inserted in the vacuum system of the MRS. Particle localization in the focal plane is done by means of two sets of vertical drift chambers (VDC's), each providing an 'X' coordinate (bend plane position) and a 'U' coordinate running at 30° to 'X' (see Fig. 2.5a). The two VDC's are oriented at 45° to the central ray. Fig. 2.5b shows the configuration of a VDC. Following the upper VDC is an array of 8 plastic scintillators. The focal plane VDC's are of the 'MIT' type (Be-77). The principle of operation is that the electrons produced by ionization from a passing proton, drift toward the anode, which is made up of signal wires and guard wires. The combination of signal and guard wires results in drift cells 2 mm wide and 12 mm long, with field lines perpendicular to the wire plane on most of their length. The drift velocity is constant down to about 0.5 mm from the wire. The measurement of drift times from several neighboring wires allows reconstruction of the intersection with the wire plane to ~100μm (FWHM), and of the angle with this plane to ~10 mr (FWHM). The dimension of the VDC's are such that a particle traversing it at ~45° should hit 3 to 5 wires. The signal wires are 6 mm apart in the VDC's. The drift times from each wire hit are digitized in TDC's.

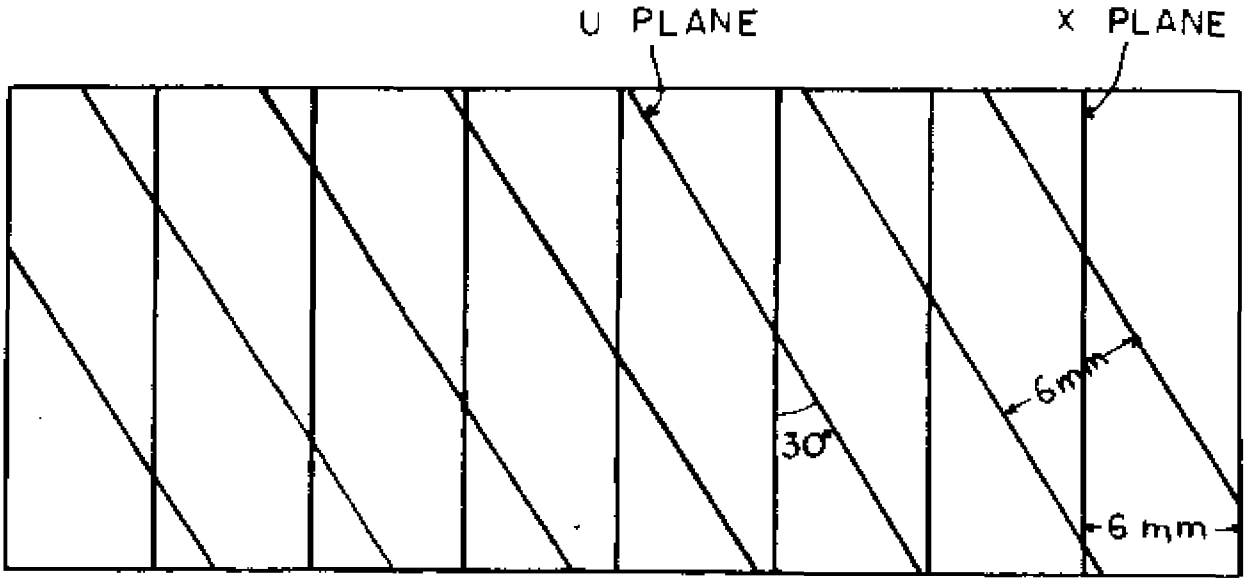

FIGURE 2.5a

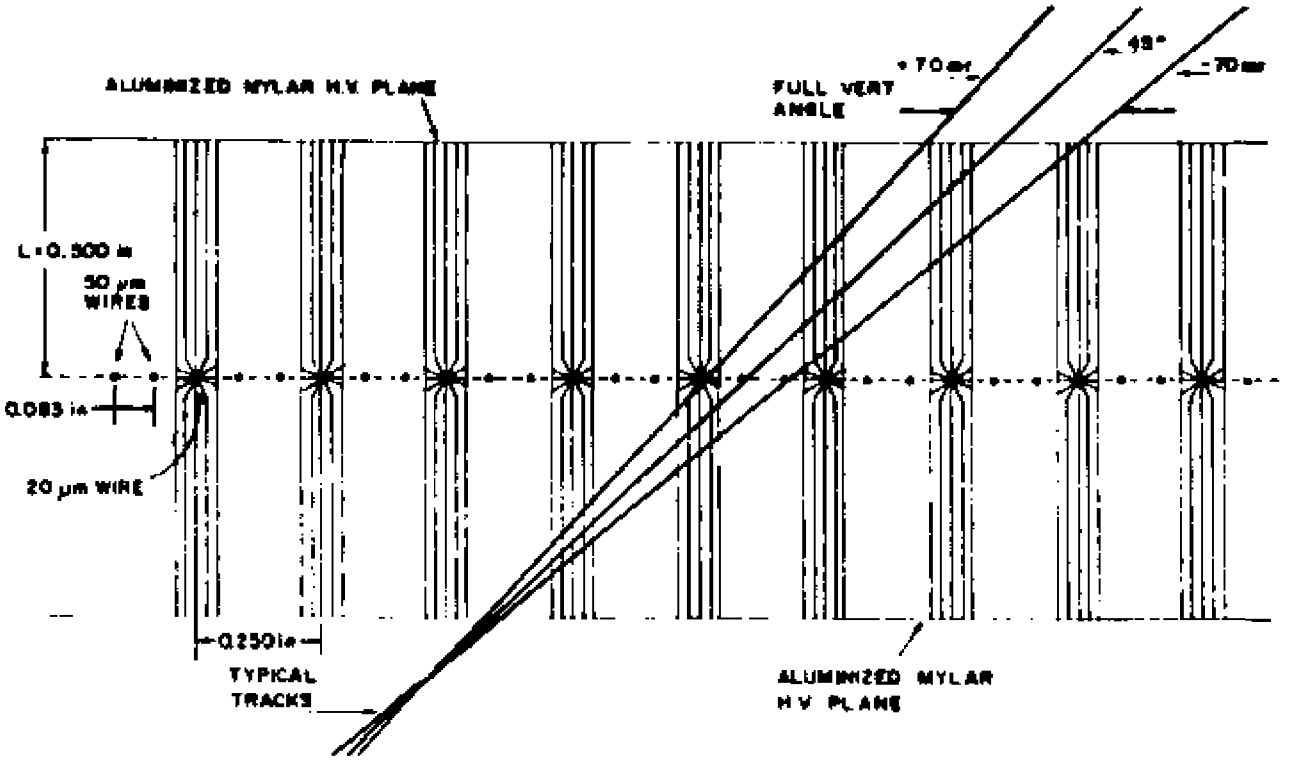

FIGURE 2.5b

A thin plastic scintillator 0.079 cm thick, called ΔE_B (Fig. 2.3), was located between the target and (X_o, Y_o) chamber at a distance of 163 cm in the 1983 experiment. The solid angle $\Delta\Omega_3$ was defined by applying cuts on the X_o and Y_o coordinate for the 1983 measurements. For the 1984 measurements we had two solid angle defining plastic scintillator counters named ΔE_{BO} and ΔE_{B1} in front of (X_o, Y_o) chamber at a distance of 145.8 cm and 135 cm. For the ΔE_{BO}, a 1.7 cm diameter hole was carved in a 8 x 8 cm plastic scintillator. The ΔE_{B1}, detector was 3.5 cm in diameter and 0.159 cm thick. The time of flight (TOF) between the ΔE_B's and plastic scintillators at the top of the MRS was measured. Distance between the two groups of scintillators is approximately 11 m. TOF and momentum together identify the particles. The momentum acceptance of the MRS is +12 % to -10 % of the central momentum only when the cuts on X_0 and Y_0 are sufficiently restrictive. The central momentum can be set by adjusting the currents in the quadrupole and dipole magnets. The magnetic field of the dipole is measured with a NMR probe inserted between the pole faces of the magnet. The entire spectometer assembly is mounted on a large support boom which can be rotated around the 4BT2 target center. The accuracy with which the MRS angle can be set is $\pm$ 0.02°.

2.6 MRS ELECTRONICS

The MRS event trigger consists of a coincidence (MASTERGATE in fig. 2.6) between a signal from ΔE_B (MRS LOGIC in fig. 2.8) and a signal from one of the focal plane scintillators at the top of the MRS. The

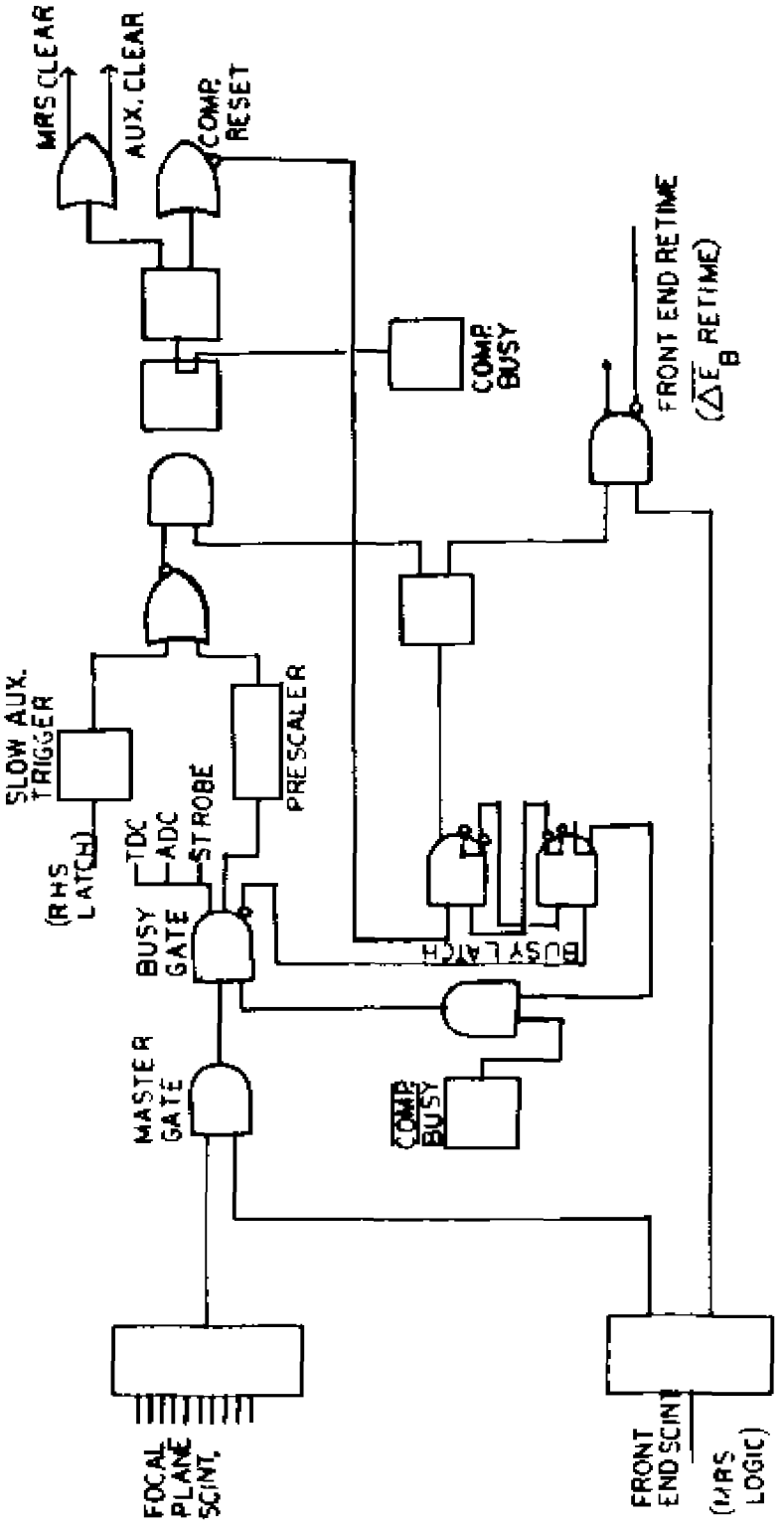

(NAMES IN PARENTHESIS REFERS TO FIGURE 2.8)

FIGURE 2.6

threshold and timing of this coincidence are set by programable ECL descriminators and delays (LeCroy). The MASTERGATE output signal will set the BUSY LATCH, unless the computer is busy. If the BUSY LATCH is set, and no L·R coincidence signal (RHS LATCH in fig. 2.8) is present on the SLOW AUXILIARY input, a fast clear signal is generated to reset the MRS. If on the other hand, the RHS LATCH signal is present no reset will be generated and the event will be processed, i.e., a TDC start pulse, an ADC gate pulse and bit pattern strobe pulse are generated, and a CAMAC trigger is produced. The data transfer is then initiated and computer signals are generated (COMP. BUSY and $\overline{\text{COMP. BUSY}}$). The BUSY LATCH then remains set until the computer busy condition is removed. At this time, a normal ending is occuring and clear signals are generated for the MRS and RHS (COMPUTER RESET in fig. 2.8) electronics. The pulses from all scintillators on the MRS side are digitized in ADC's, providing energy information. Timing signals from the ΔE_B and the focal plane scintillators are digitized in the TDC's, providing time-of-flight information. This information is used for particle identification. The MRS electronics has provisions for generating pulser events to check the system without beam and to measure the live-time of the system during actual running.

2.7 RHS AND COINCIDENCE ELECTRONICS

Fig. 2.7 shows the electronics for the counter telescopes and how the RHS trigger signal was generated. Also shown are the various locations connected to ADC's, TDC's and a bit pattern unit in the CAMAC crate. The trigger for the RHS was a signal from one of the plastic

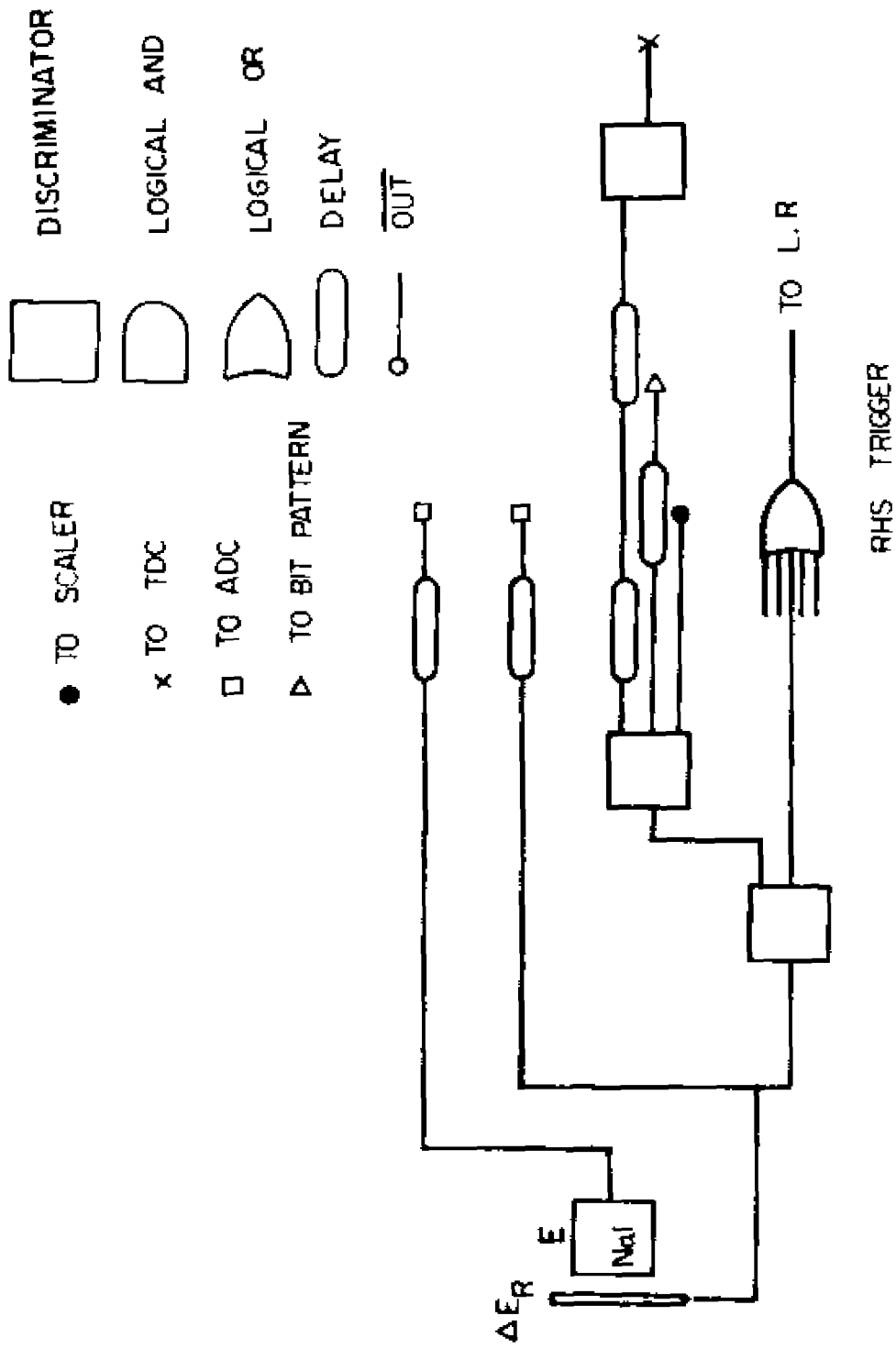
DISCRIMINATOR
LOGICAL AND
LOGICAL OR
DELAY
OUT
● TO SCALER
× TO TDC
□ TO ADC
△ TO BIT PATTERN
TO L.R
RHS TRIGGER
E
NaI
ΔE_R

FIGURE 2.7

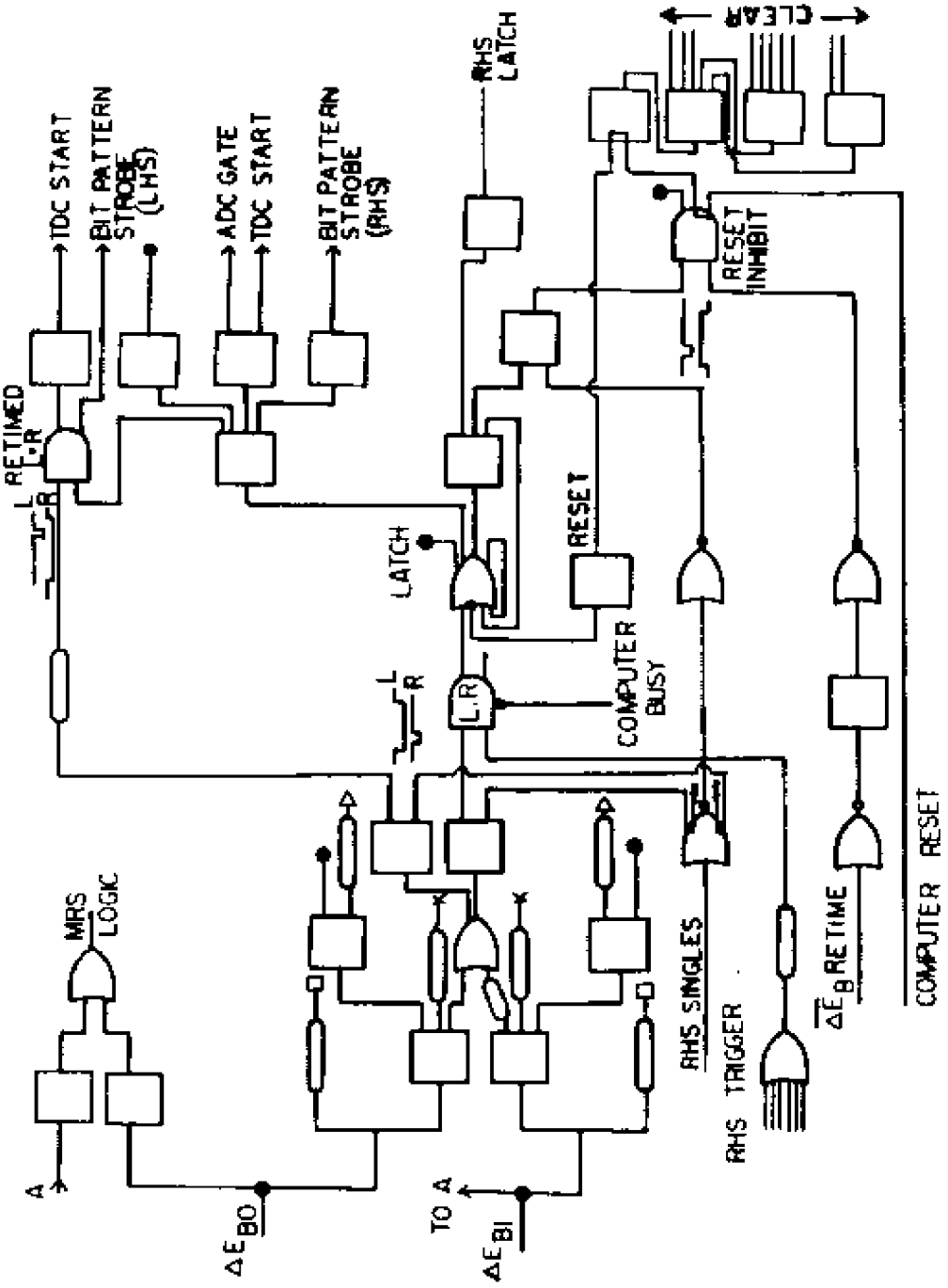
TDC START
BIT PATTERN STROBE (LHS)
ADC GATE
TDC START
BIT PATTERN STROBE (RHS)
RHS LATCH
CLEAR
RESET INHIBIT
RETIMED L·R
L R
LATCH
RESET
L·R
L R
COMPUTER BUSY
MRS LOGIC
A
ΔE BO
TO A
ΔE BI
RHS SINGLES
RHS TRIGGER
ΔE B RETIME
COMPUTER RESET

FIGURE 2.8

scintillator detectors ΔE_R. A coincidence between this signal and the signal from the ΔE_B counter on the LHS is detected by the L·R coincidence circuit (in Fig. 2.8) which is timed on the RHS. As soon as the L·R coincidence is formed, the LATCH is set using a majority coincidence unit to prevent another event from being processed. Also a gate pulse for the ADC's, a strobe pulse for the bit pattern and a start pulse for the TDC's used for right-to-left timing are generated from the LATCH output. Again, the various locations connected to ADC's, TDC's and the bit pattern unit are shown. A second L·R coincidence (RETIMED L·R), timed on the LHS, provided another TDC start for left-to-right timing; this is the timing information which was used for the separation of real and random events as explained in section 3.2. Normally, the latch will be reset by a signal from the MRS (COMPUTER RESET). However, if no valid event was detected in the MRS, the coincidence circuit would reset itself; for a good event, this selfresetting function is prevented by the ΔE_B-RETIME (fig. 2.6) signal from the MRS (RESET INHIBIT input). At the same time that the LATCH is reset, clear signals are sent to all CAMAC units.

For test purpose, through the line called RHS SINGLE as shown in fig. 2.8, the RHS electronics can be triggered without requiring a signal from the LHS.

2.8 DATA ACQUISITION

The data acquisition system comprised an Eclipse computer interfaced to three CAMAC crates and used DACS (data acquisition system), a software system adapted to the MRS Eclipse Computer. A

detailed description of DACS can be found in a TRIUMF report (Ti-84). Commands are provided in DACS to acquire data through CAMAC, to store the data in a temporary buffer, to write the information blockwise onto the magnetic tape, and to analyse a portion of the data applying software cuts to produce on line spectra. Such spectra were essential to monitor the good progress of the experiment.

When a charged particle is detected on the LHS by the ΔE_B counter and on the RHS by the ΔE_R counter, the electronic logic circuits determine the occurrence of a valid left-right coincidence event as described in section 2.7. At the same time the MRS electronics is being triggered by a coincidence between ΔE_B and one of the focal plane plastic scintillators. If the logic requirements as described in section 2.6 and 2.7 are satisfied, a signal is sent to the CAMAC system to effect a read-out of the data, both from the MRS and the RHS telescopes, into a memory buffer. The RHS information read includes pulse height from all scintillator and NaI(Tl) counters, time-of-flight between the ΔE_B counter and RHS scintillators and a bit pattern to identify which counter on the RHS fired, or the nature of the event as either one due to charged particles in the detectors or one due to the firing of light emitting diodes (LED) in all scintillators, triggered by a randomly generated pulse. The LHS information includes chamber read-out, time-of-flight from ΔE_B to focal plane scintillator, energy loss in ΔE_B and focal plane scintillators and a bit pattern to identify the type of event and which scintillator (ΔE_{BO} or ΔE_{B1} for 1984) fired. A way to prevent a new event from being acquired while data are being processed by the computer, is provided by the latching mechanism

described in section 2.7. After an event has been recorded into the memory buffer, the system was reset to allow for the acquisition of the next event. When the memory buffer became full the data were written on magnetic tape and part of the data analyzed to produce on line spectra.

There were two kinds of events recorded on magnetic tape:
1) scaler events: the scaler events, triggered by a clock at constant intervals were read in every five seconds. Scalers were connected to various points in the electronics logic, as indicated in figure 2.6, 2.7 and 2.8.
2) regular events: regular events were coincidence events and were either pulser events, or (p,2p) (or (p,p) elastic events with the hydrogen target) as identified by the bit set for them in the bit pattern register. The pulser events are used to measure the live time factor of the electronics and data acquisition system and were generated by LED's. Such events had the same pattern as regular events, and had to satisfy the same logic requirements.

The event structure is shown in Table 2.1 for the 1983 data and Table 2.2 for the 1984 data.

TABLE 2.1

EVENT STRUCTURE (1983 DATA)

Words	Source
1	Event length
2	Event type
3	Sequence #
4-13	ADC

14-35	TDC
36-37	RHS bit pattern
38-39	MRS bit pattern
40-48	TDC
49-50	ADC
51	Number of hits +1
52 onwards	Address of wire hits in MWPC'S

TABLE 2.2

EVENT STRUCTURE (1984 DATA)

Words	Source
1	Event length
2	Event type
3	Sequence #
4-5	RHS bit pattern
6-22	ADC
23-37	TDC
38-39	MRS bit pattern
40-45	TDC
46-58	ADC
59-60	60 Hz clock
61	Number of hits +1
62 onwards	TDC address and times for the drift chambers

In tables 2.1 and 2.2 the first word is the event length, and the second word is a flag identifying the event type. The RHS bit pattern register allowed to identify pulser events, and were decoded to provide the identity of the telescope involved. The rest of the information concerns the pulse height in the NaI(Tl) and plastic scintillators, time-of-flight information and wire address for the 1983 data, TDC address and time for the 1984 data.

Chapter III

DATA ANALYSIS

3.1 INTRODUCTION

An Eclipse minicomputer was used to acquire the data at TRIUMF. The off-line data analysis has been done using IBM and NAS mainframe computers at the College of William and Mary. First the data were transferred from variable block size to fixed block size. Then the analysis program was developed in stages, as the data processing progressed. The analysis program prepared one-dimensional and two-dimensional spectra, with or without cuts on various variables like time-of-flight or pulse height; it also calculates corrections for energy loss due to absorbers, as well as the missing mass of the recoil particle, and finally the differential cross sections. Section 3.2 describes the initial phase of the analysis. Section 3.3 contains the analysis carried out to obtain energy calibrations for the NaI(Tl) detectors and the MRS focal plane momentum calibration. Section 3.4 describes the determination of the pp differential cross section and how it was used to determine the target thickness. Section 3.5 describes the analysis of the (p, 2p) data proper, and Section 3.6 describes how the five-fold differential cross sections were obtained from the data; a discussion of various correction factors and the error analysis are also included in this part.

3.2 INITIAL ANALYSIS

The data were analyzed event by event. Depending on the event length each data block on tape contained six or seven events. There were two different kinds of events on tape: 1) scaler event, and 2) regular coincidence event. The third word in the event structure identified the event type. Each time a scaler event was identified, it was counted and all the scaler values were updated, taking care of overflows as they ocurred. Among the regular events were pulser events, which satisfy all the requirements as (p, 2p) events but are triggered by a pulser to determine the live-time factor of the system. These events are identified by the bit set for them in the bit pattern register. For every run, the pulser events were identified and counted, and their numbers then compared with the number of times the pulser was actually triggered; the ratio of these two numbers gives a measure of the system's live time LT in a particular run. We can write it as

$$LT = \frac{\text{Pulser accepted}}{\text{Pulser triggered}}$$

This ratio was typically about 80% for the (p, 2p) data and 35% to 55% for the hydrogen data.

Events were rejected from further analysis for any of the following reasons:

1) No bit set in the bit pattern register for any RHS counter telescope.

2) The event length was less than 55 words (for 1983 data) and 66 words (for 1984 data), as such short events contained no wire chamber information.

3) The events were not within a chosen window of values for TTB (time of flight from E_B to focal plane scintillators). Fig. 3.1 shows a typical histogram for TTB and the windows. This selection helped reject particles that were not protons or originated in other beam bursts, and thus were random events.

4) Random events (events originated from same beam burst but not from same reaction) were subtracted using a sample of events originating from different beam bursts following the true coincidence events. A TOF spectrum is shown in fig. 3.2.

Next the decoding of the chambers was done. In the 1983 experiment we used three sets of MWPC for the coordinates (X_o, Y_o), (X_b, Y_b) and (X_t, Y_t) in the MRS. In the 1984 experiment we had front end drift chambers (FEC's) (X_o, Y_o) at the entrance of the MRS with a total of 4 wire planes, and two sets of vertical drift chambers (VDC's), (X_1, X_2), (U_1, U_2) at the exit of the dipole magnet, below and above the focal plane.

Events were rejected if any one of the (X_o, Y_o), (X_t, X_b) MWPC planes had a missing wire coordinate or more than five wires hit. Events (1983) with two to five wires hit were accepted provided the gap was no more than two wires. (A gap occurs when a wire did not fire in an otherwise continuous pattern of hits). In 1984 and for the (X_o, Y_o) planes, events with no wire hit or more than two wires hit were rejected (FEC's have drift space perpendicular to particle trajectories). For the X_1 plane events with less than three wires hit or more than five wires hit were rejected. (VDC's have drift paths at ~45° to trajec-

TTB SPECTRUM

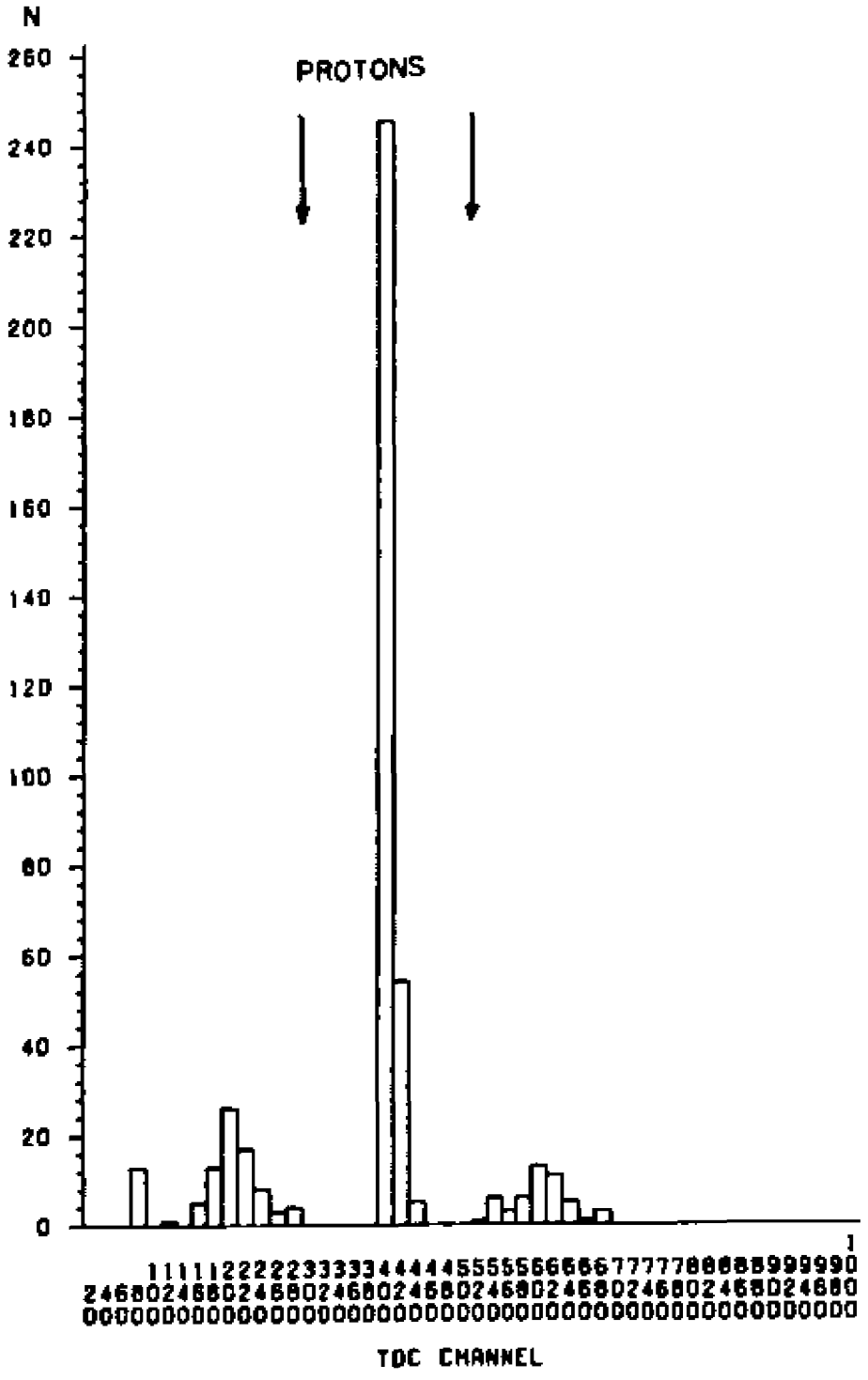

FIGURE 3.1

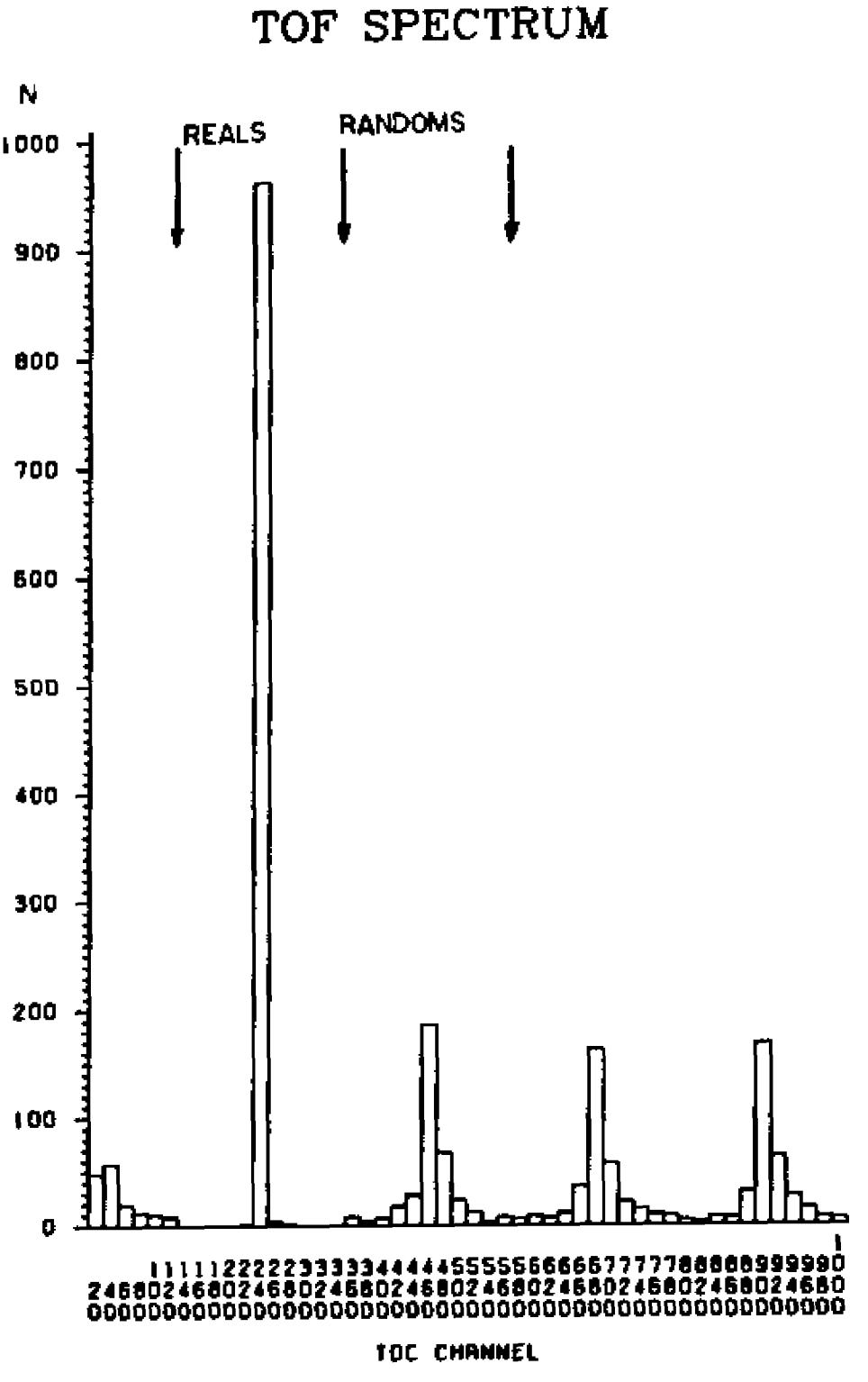
TOF SPECTRUM
N
1000
900
800
700
600
500
400
300
200
100
0
REALS
RANDOMS
TOC CHANNEL

FIGURE 3.2

tory. A typical number of hit is 4). The focal plane coordinate XF was then calculated from the X_b and X_t coordinate (1983 - data) as follows

$$XF = ((220\ (X_b - 2X_t))/(X_b - X_t - 220)) + 0.005\ (X_o - 24)^2$$

(in wire number units)

and from the X_1 and X_2 coordinates (1984 - data) as follows:

$$XF = (G(X_1 + H) - F(X_1 + H - X_2))/G \quad \text{(in 50}\mu\text{m units)}$$

where F, G and H are constants, and their values are 3400, 5472 and 7392 (in units of 50 μm), respectively.

We did not use the X_2 coordinate as one wire was dead in that chamber in the region of interest; instead we calculated the X_2 coordinate from the X_1 coordinate, using the fact that the angle the trajectory makes with the detector plane is strongly correlated to the value of X_1. This procedure introduced no important uncertainty because the focal plane is parallel to the chambers.

Fig. 3.3 shows the focal plane XF, X_1 and X_2, the constants F, G and H and the angle Θ. We calculated Θ as below

$$\Theta = \tan^{-1}(G/(X_1 + H - X_2))$$

and fitted Θ as a function of X_1 by linear regression

$$\Theta = aX_1 + b\ ;$$

the values found were a = (3.05 ±0.6) 10^{-4}° /channel and b = 42.4 ±1.6)°. The "missing coordinate X_2 was then calculated from

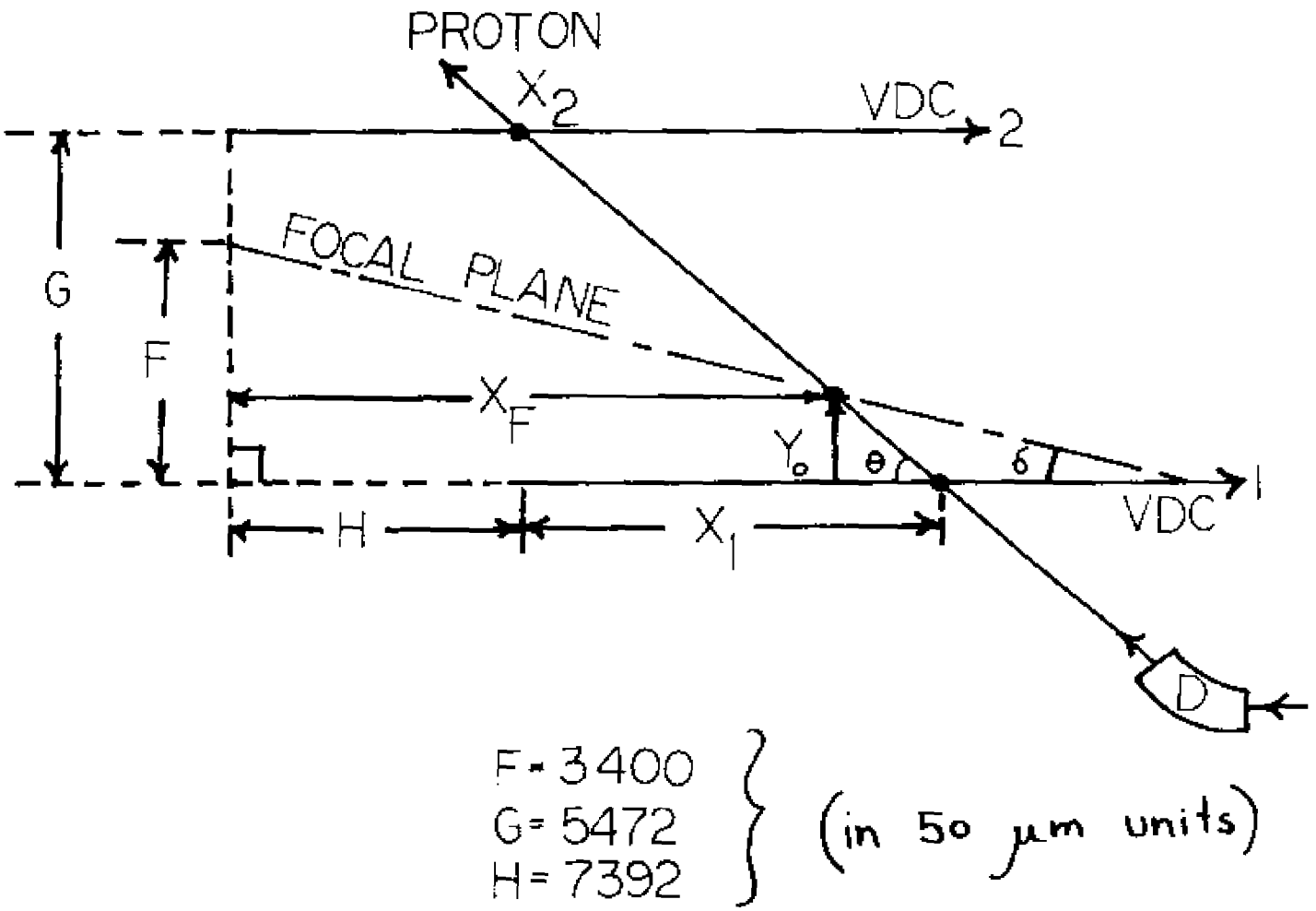
PROTON
X2
VDC
2
FOCAL PLANE
G
F
XF
Yo
θ
δ
1
VDC
H
X1
D
F = 3400
G = 5472
H = 7392
(in 50 μm units)

FIGURE 3.3

$$X_2 = X_1 + H - G/\tan\Theta(X_1)$$

We estimate that the uncertainty introduced by this approximation is of the order of ±1.9 MeV/c

3.3 CALIBRATION OF DETECTORS AND FOCAL PLANE

Energy calibration were obtained with the same setup as when the (p, 2p) data were acquired, but with liquid hydrogen as target. For the focal plane calibration we kept the magnetic field constant and changed the angle of the MRS. For NaI(Tl) detectors, we changed the angle of the detectors to change the energy (1983); in 1984 we used (p, 2p) data for this calibration.

The most probable values of the NaI pulse height (PH) were plotted against the calculated and corrected (for energy loss in absorber and other material) kinematical values of T_4; similarly, the most likely values of the XF-coordinate were plotted against the calculated and corrected kinematical values of p_3. The reaction participants are labelled as

$$1 + 2 \rightarrow 3 + 4$$

(1 is the incident proton, 2 is the H_2 nucleus, 3 and 4 are the scattered and ejected protons), with convention that particle 3 is detected by the MRS on the LHS of the incident beam and particle 4 is detected by the counter telescopes on the RHS.

The values for each kinematical configuration are given in table 3.1 (1983), where p_3 and T_4 are central values calculated from the kinematics for Θ_3 and Θ_4 set to the detector angles.

Fig. 3.4a shows the plot of XF-channels vs. corrected p_3 and 3.4b is the plot of NaI PH vs. corrected T_4. The constants are found as shown below.

For the MRS, defining

$$p = p_o (1 + aX) \text{ with } X = XF - 256$$

$$p_o a = -(3.92 \pm 0.14)\ 10^{-1} \text{ MeV/c/channel}$$

$$a = -(5.36 \pm 0.20)\ 10^{-4} \text{ 1/channel at } p_o = 731. \text{MeV/c}$$

To establish the connection with the B field strength, we write:

$$p_o\ (XF = 256) = aB, \text{ where B is the field strength.}$$

$$a = (0.792 \pm 0.004)\ 10^{+3} \text{ MeV/c/Tesla}$$

In general, the B-field is different for different kinematic configurations, but no hysteresis correction is needed as B was measured directly with a NMR probe.

For a RHS NaI crystal:

$$T_4 = a + b \times \text{ADC (channels)};$$

the data were fitted by linear regression and the values for a and b found were:

TABLE 3.1

1983 CALIBRATION OF THE MRS FOCAL PLANE AND RHS NAI CRYSTAL

Θ_3	Θ_4	XF - Channels Units: Wire Spacing of 2mm	p_3 MeV/c	p_3 MeV/c Corrected	NaI PH Channels	T_4 MeV	T_4 MeV Corrected
34.54°	49.00°	15 ±4	833.1	830.9	448 ±8	189.	113.
37.85°	45.50°	125 ±4	787.1	784.9	560 ±8	220.	154.
41.62°	41.62°	268 ±4	733.6	731.4	672 ±8	253.	195.
44.33°	39.00°	358 ±4	694.0	691.0	752 ±8	277.	222.

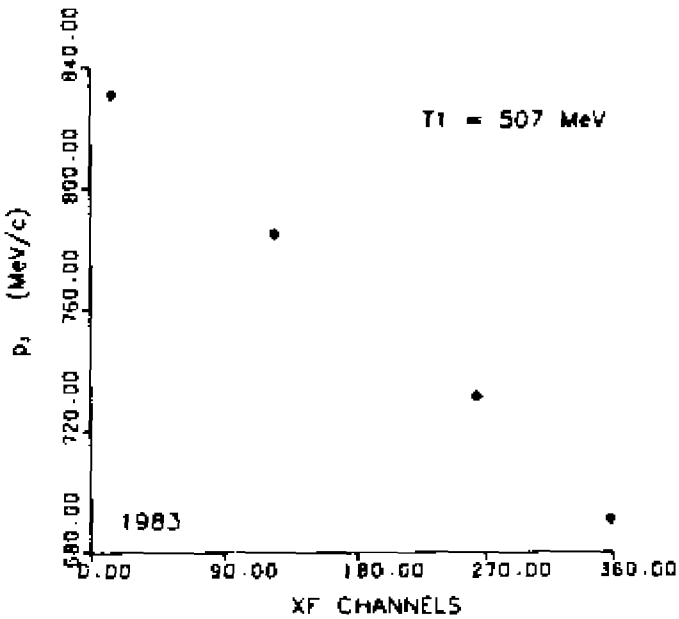

FIGURE 3.4a

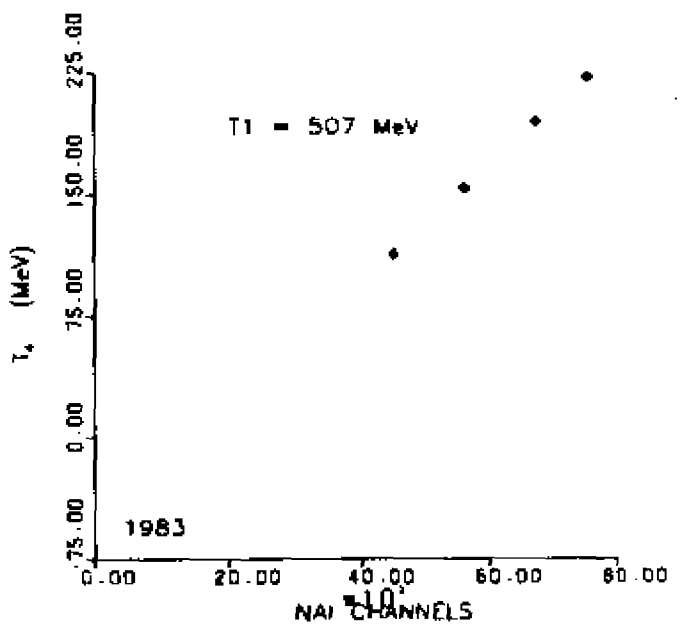

FIGURE 3.4b

$$a = -(44. \pm 2.)\ \text{MeV}.$$

$$b = (3.59 \pm 0.03)\ 10^{-1}\ \text{MeV/channel}$$

Table 3.2 shows the data for the 1984 focal plane calibration.

TABLE 3.2
1984 FOCAL PLANE CALIBRATION

Θ_3	XF-channels Units (50μm)	p_3 $\frac{MeV}{c}$
38.48°	5440 ±200	779.1
40.05°	8900 ±200	757.6
41.62°	12540 ±200	735.0
43.09°	15960 ±200	713.6
44.58°	19580 ±200	691.7

These data were also fitted by linear regression, writing $p = p_o (1 + \alpha XF)$, the constants were found to be

$$p_o\ (XF = 0) = aB = 814.3 \pm 0.2\ \text{MeV/c for B = .9081 Tesla}$$

$$p_o\alpha = -(0.635 \pm 0.017)\ 10^{-3}\ \text{MeV/c/channel}$$

$$\alpha = -(0.780 \pm 0.020)\ 10^{-3}\ \text{1/channel}$$

$$a = (896.7 \pm 0.3)\ \text{MeV/c/Tesla}$$

In 1984, six counter telescopes were available on the RHS. We used four of them for the data presented here. (another part of these data, for asymmetric kinematics, uses all six counters; these data have been analyzed at California State University, Los Angeles) (An-85). We

used the deuterium data for the calibration of these NaI detectors. The calibration data are given in tables 3.3 and 3.4. All of these data were fitted by linear regression.

TABLE 3.3

THE DATA FOR CALIBRATION OF COUNTER E_1

NaI PH Channels	T_4 MeV	T_4 Corrected MeV
660 ±8	223.	166.
690 ±8	230.	174.
715 ±8	236.	181.
755 ±8	246.	193.
785 ±8	254.	202.
810 ±8	259.	210.
840 ±8	268.	218.
865 ±8	275.	226.
890 ±8	280.	233.

Write: $T_4 = a + b \times ADC$ (channels)

$a = (29. \pm 1.4)$ MeV

$b = (0.294 \pm 0.002)$ MeV/channel

The rest of the calibration data had no Cu absorber so there is no correction for T_4.

The focal plane calibration constants were then used to calculate momentum and energy of particle 3 and the RHS calibration constants were used to calculate energy of particle 4 for each event.

TABLE 3.4

THE DATA FOR CALIBRATION OF COUNTER E_2, E_3 & E_4

E2 Counter		E3 Counter		E4 Counter	
NaI PH channels	T_4 MeV	NaI PH channels	T_4 MeV	NaI PH channels	T_4 MeV
545 ±8	138.	430 ±8	182.	384 ±8	109.
590 ±8	151.	505 ±8	167.	425 ±8	123.
628 ±8	164.	566 ±8	149.	465 ±8	135.
665 ±8	177.	615 ±8	130.	480 ±8	147.
695 ±8	189.	665 ±8	104.	510 ±8	157.
				530 ±8	167.
a = -36. ±1.4 MeV		a = 29. ±1.4 MeV		a = 34. ±1.4 MeV	
b = 0.320 ±0.002 MeV/channel		b = 0.317 ±0.002 MeV/channel		b = 0.370 ±0.002 MeV/channel	

3.4 pp DIFFERENTIAL CROSS SECTION

We measured the pp differential cross section using the same experimental setup, same target cell as for the study of $^2H(p, 2p)$, but with the deuterium replaced by hydrogen; the incident energy was also the same as for the $^2H(p, 2p)$ measurements. Furthermore final energies and the angles were 41.6°-41.6° and 30.0°-53.7°, very nearly the same as those for the 41.4°-41.4° (1983 and 1984) and 30.1°-53.75° (1984) (p, 2p) data. For the conditions of the experiment, the differential pp cross section is:

$$d\sigma/d\Omega = N/\Delta\Omega_3\ n_H\ I\ LT\ \epsilon_1$$

where N is the number of protons detected within solid angle Ω_3; n_H is the number of H-nuclei per unit area in the target, and I is the integrated incident proton beam current. LT is the live-time correction factor (see section 3.2) and ϵ_1 is the correction for the efficiency of the chambers in the MRS, mainly determined by the combined probability of a single-wire hit in each one of the MWPC (1983); and of an acceptable pattern in the drift chambers (1984).

We determined the target thickness by comparing the measured pp cross sections at the 41.6° angle pair (90°CM) to the recent high precision measurements of the pp cross section at 500 MeV (Ch-82) and 515 MeV (Ot-84) at the same angles, which give a value of (3.44 ±0.062) mb sr^{-1} center of mass (CM) at 508 MeV, or (10.43 ±0.19) mb sr^{-1} cross section in the lab frame.

Then $$n_H = \frac{(N/\Delta\Omega_3\ I\ LT\ \epsilon_1\ N_o)}{10.43}$$

$$n_H = \rho_H\ (P,\ T)\ x\ t_{tgt}/\cos\ \Theta$$

ρ_H (P, T) is the density of hydrogen at the pressure and temperature maintained and monitored during the experiment; at a pressure of 250mbar, ρ_H = 75.02 ±0.10 mg/cm^3. N_o is Avogadro's number and the target angle Θ=0°. We found the target thickness to be 0.753 ±0.015 cm. The areal density for deuterium in 1983 was 129.0 ±2.6 mg cm^{-2}. The density of liquid deuterium at the pressure of 250 mbar (corresponding to a temperature of 19.5°K), is ρ_D = 172.0 ±0.26 mg/cm^3.

We followed the same procedure to find the target thickness for the 1984 data also. The target thickness was found to be 0.887 ±0.018 cm. The areal density for deuterium in 1984 was then 152. ±3. mg cm^{-2}.

The increase in target thickness from 1983 to 1984 was due to an error made when trying to measure the target thickness at room temperature and atmospheric pressure. The target cell was pressurized more than 250 mbar, causing a permanent deformation of the foils.

Physical measurement using micrometers were performed in 1984, both at room temperature, and at a temperature of 37 K. The results were 0.920 ±0.005 cm and 0.926 ±0.005 cm, respectively. Taking into account the foil thickness, these results are systematically larger than those from the pp cross section measurements, by ~4.5%. We used the pp cross section values, and interpret the discrepancy as due to the overall inefficiency of the detector system, including plastic scintillator and electronics event losses. This procedure is expected to contribute only a negligible amount to the systematic error on the (p, 2p) results, because in first order the target thickness determined from the hydrogen cross section cancels out of the calculation of the (p, 2p) cross section.

We also measured the elastic pp cross section for the asymmetric angle pair 30.0°-53.75° (65.9°cm) and found 3.87 ±0.08 $mbsr^{-1}$, which disagrees with the VPI phase shift value of 3.58 $mbsr^{-1}$; but is in excellent agreement with the experimental result of Hoffmann (Ho-84), 3.83 ±0.08 $mbsr^{-1}$, at the same CM angle and 497.5 MeV beam energy.

3.5 ANALYSIS OF THE (p, 2p) DATA

After various cuts were applied in the initial analysis, two-dimensional displays of X_o-Y_o were created and events within uniform region of these distributions were selected by software cuts for the 1983 data as shown in fig. 3.5. For the 1984 data, we had two solid angle defining plastic scintillator counters in front of the X_o-Y_o chambers. The projection of these counters at the X_o-Y_o chambers are shown in fig. 3.6 and 3.7. The data were analyzed using either counter separately to produce the high precision results discussed below. Table 3.5 shows the symmetric angle pairs we measured in the 1983 experiment and Table 3.6 the angle pairs we measured in the 1984 experiment. Table 3.7 shows the geometry for the high precision data of 1984. Additional asymmetric angle pair data were obtained in the 1984 experiment. A part of these data was analyzed here, and will be discussed succinctly in section 5.4; the other part has been analyzed at C.S.U.L.A.(An-85).

TABLE 3.5

T_1 = 0.507 GeV

ANGLES MEASURED IN 1983

θ_3	θ_4	p_3 MeV/c	T_4 MeV	Minimum Recoil MeV/c
50.°	50.°	723.	240.	174.
52.°	52.°	706.	243.	223.
57.°	57.°	672.	221.	362.
66.°	66.°	557.	149.	649.

TABLE 3.6

T_1 = 0.508 GeV

ANGLES MEASURED IN 1984

θ_3	θ_4	p_3 MeV/c	T_4 MeV	Minimum Recoil MeV/c
38.13°	38.°	732.	252.	-54.
44.13°	44.°	732.	252.	46.
47.13°	47.°	729.	250.	106.

TABLE 3.7

T_1 = 0.508 GeV

ANGLES MEASURED FOR THE HIGH PRECISION DATA

θ_3	θ_4	p_3 MeV/c	T_4 MeV	Minimum Recoil MeV/c
41.36°	41.41°	735.	252.	1.9*
41.54°	41.41°	735.	252.	1.9
30.13°	53.75°	891.	150.	3.5

* Data with smaller $\Delta\Omega_3$.

p_3, T_4 are calculated for minimum recoil, using the angles of the detector axis θ_3 and θ_4.

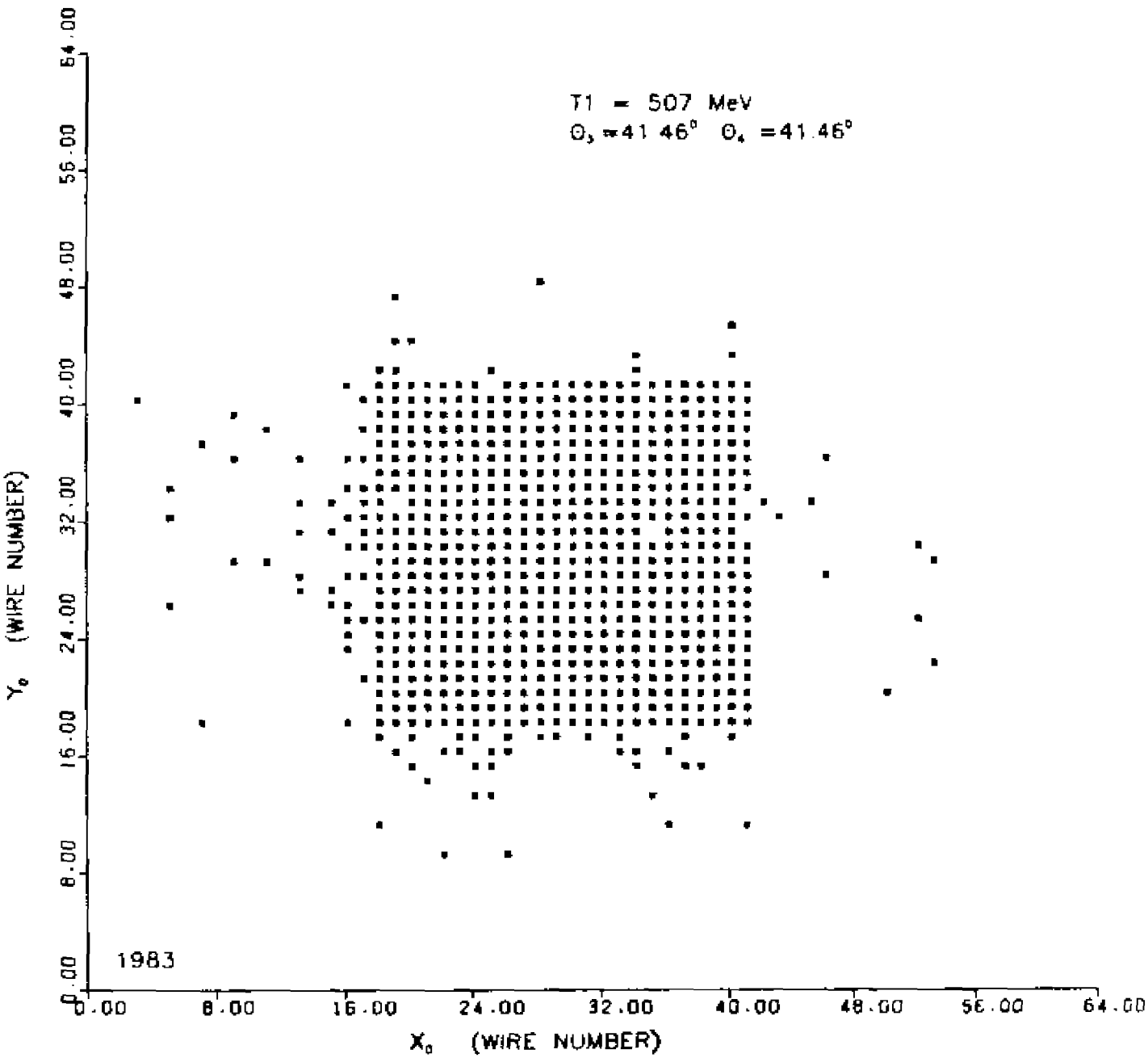
T1 = 507 MeV
Θ_3 =41 46° Θ_4 =41.46°
1983
Y_0 (WIRE NUMBER)
X_0 (WIRE NUMBER)
0.00
8.00
16.00
24.00
32.00
40.00
48.00
56.00
64.00

FIGURE 3.5

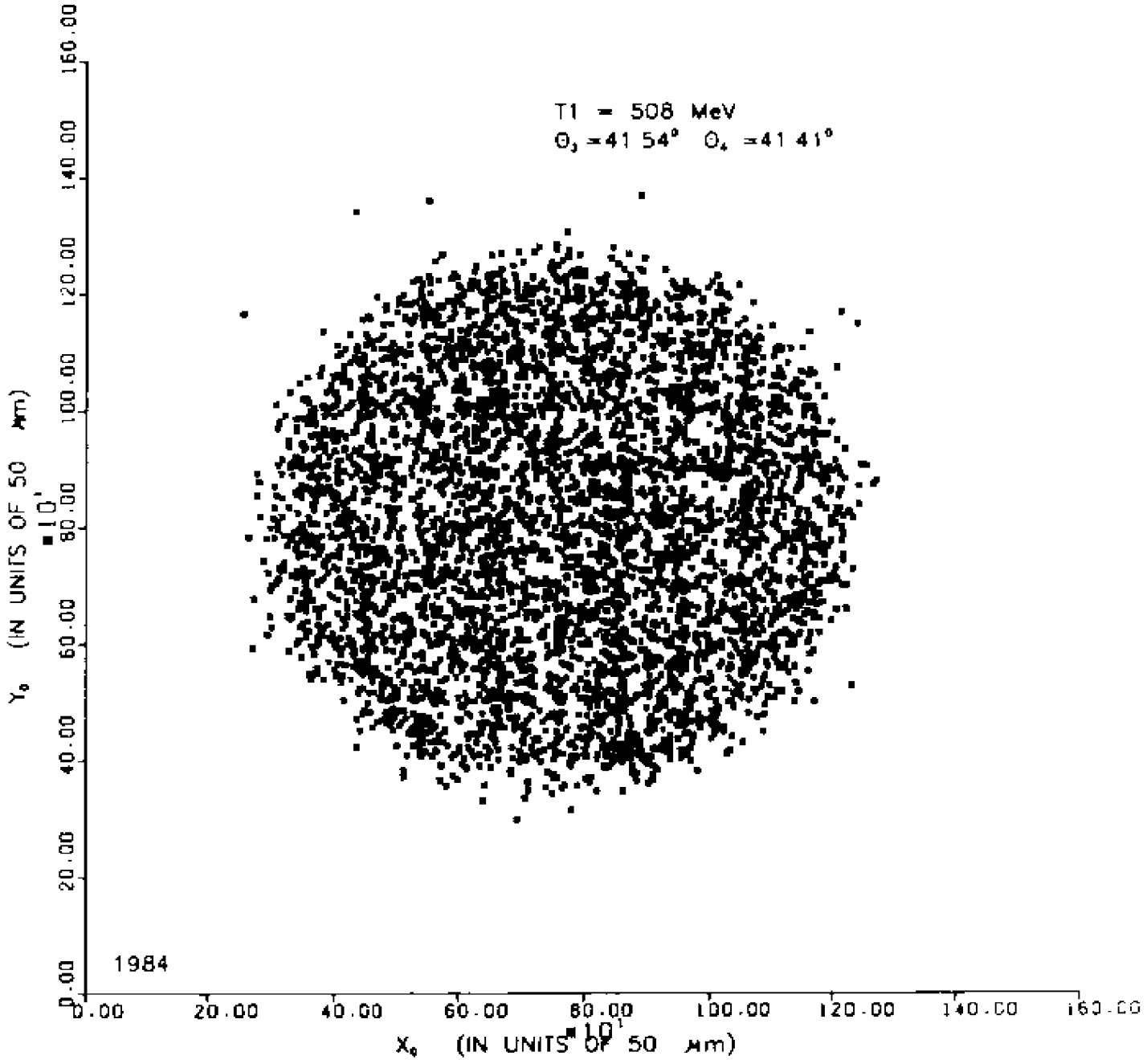
T1 = 508 MeV
Θ_3 =41 54° Θ_4 =41 41°
1984
Y_0 (IN UNITS OF 50 μm)
X_0 (IN UNITS OF 50 μm)
0.00
20.00
40.00
60.00
80.00
100.00
120.00
140.00
160.00

FIGURE 3.6

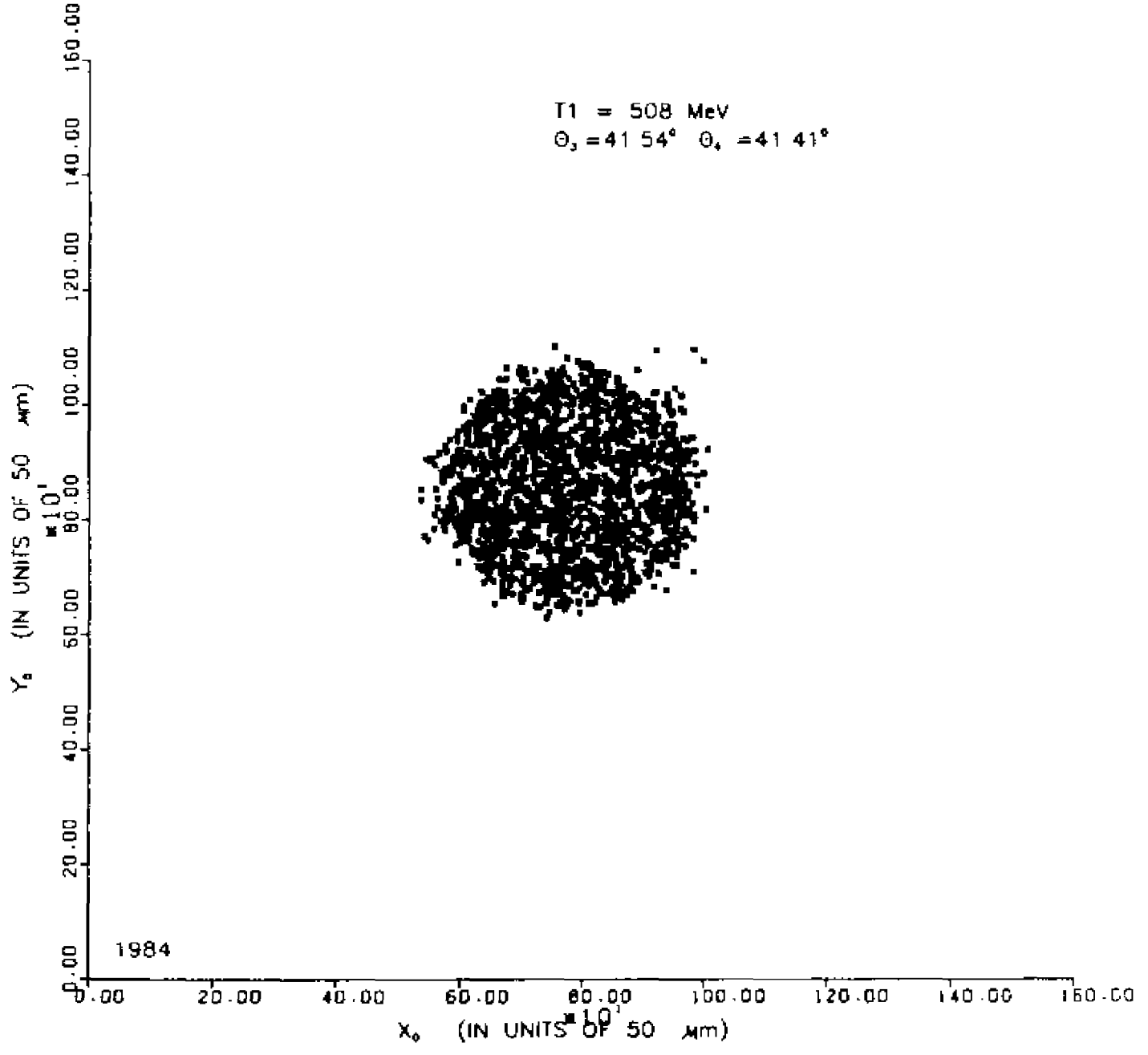
T1 = 508 MeV
Θ3 = 41 54° Θ4 = 41 41°
1984
Y0 (IN UNITS OF 50 μm)
X0 (IN UNITS OF 50 μm)
0.00
20.00
40.00
60.00
80.00
100.00
120.00
140.00
160.00
*10¹

FIGURE 3.7

Next the momentum p_3 was calculated from the focal plane coordinate XF of the MRS and magnetic field strength and the kinetic energy T_4 from the pulse heights in the NaI(Tl) detectors using the calibration constants given in Section 3.3. Corrections were applied for energy losses in the various absorbers including the Cu preceding the NaI (Tl) detectors.

Fig. 3.8 shows a typical two-dimensional plot of T_3 vs. T_4 for ^2H (p, 2p)n at the 41.54°-41.41° angle pair and central p_3 = 734. MeV/c. As expected most events are concentrated on a ridge corresponding to quasi-free scattering. There are also events due to nuclear reaction energy losses in the NaI(Tl) detector, accidental events and background events originating from the walls (steel windows) of the target cells. From the values of T_3 and T_4 we calculated the missing mass m_5 for each event:

$$m_5 = (E_5^2 - p_5^2)^{1/2}$$

$$E_5 = E_1 + m_2 - E_3 - E_4$$

$$\vec{p}_5 = \vec{p}_1 - \vec{p}_3 - \vec{p}_4$$

where E_1 and p_1 are energy and momentum of the projectile protons, m_2 is the mass of the target nucleus (deuteron), E_3, p_3 and E_4, p_4 are energy and momentum of particle 3 and 4; all variables are referred to the laboratory frame. A one-dimensional spectrum of m_5 is shown in fig. 3.9, where the location of the selection window is also displayed. The peak appears at 936 MeV instead of 939 MeV; we did not feel a need to change the T_4 - calibration to adjust m_5. The two-dimensional spectrum of T_3 vs. T_4 obtained including all initial cuts and with a cut of 14

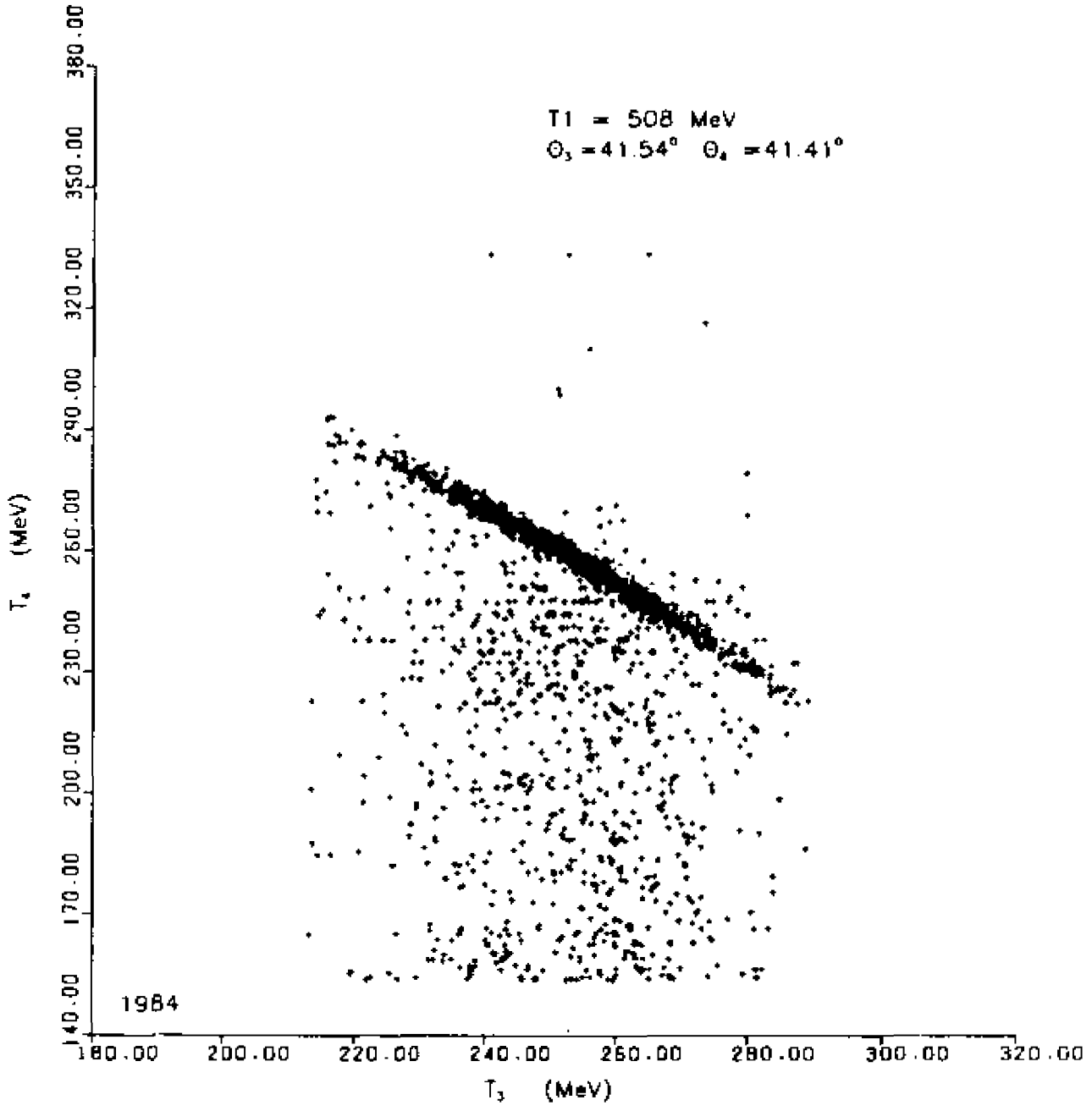
T1 = 508 MeV
Θ3 = 41.54° Θ4 = 41.41°
1984
T4 (MeV)
T3 (MeV)
140.00
170.00
200.00
230.00
260.00
290.00
320.00
350.00
380.00
180.00
200.00
220.00
240.00
260.00
280.00
300.00
320.00

FIGURE 3.8

MeV centered at the missing mass peak in figure 3.9 is shown in figure 3.10. Fig. 3.10 should be compared with fig. 3.9 which is the same spectrum without the cut on the missing mass. The missing mass cut width was varied from 12 to 16 MeV, depending on the quality (energy resolution) of the data.

The NaI pulse height information was not used for the 41° and 30° high precision data. Pion production contamination in these data could be acertained directly from the elastic pp-data; it was less than 10^{-4}. For all other angle pairs, either an energy cut or a missing mass cut was applied to eliminate any pion production contamination, based on the T_4 information from the NaI pulse height. In this case, (see next section) we needed a correction for events lost from the quasi-free ridge either by nuclear reaction, or by pile-up pulses in the NaI detector.

3.6 CROSS SECTIONS AND UNCERTAINTIES

The measured five fold differential cross sections are

$$\frac{d^5\sigma}{d\Omega_3 d\Omega_4 dT_3} = \frac{N}{\Delta\Omega_3 \Delta\Omega_4 \Delta T_3 \; n_D \; I \; LT \; \varepsilon_1 \; \varepsilon_2}$$

where N is the number of events (after random subtraction) in the energy interval ΔT_3 and within solid angle $\Delta\Omega_3$ on LHS and $\Delta\Omega_4$ on RHS where the statistical error on N is given by:

$$\Delta N = (N + 2N')^{1/2}$$

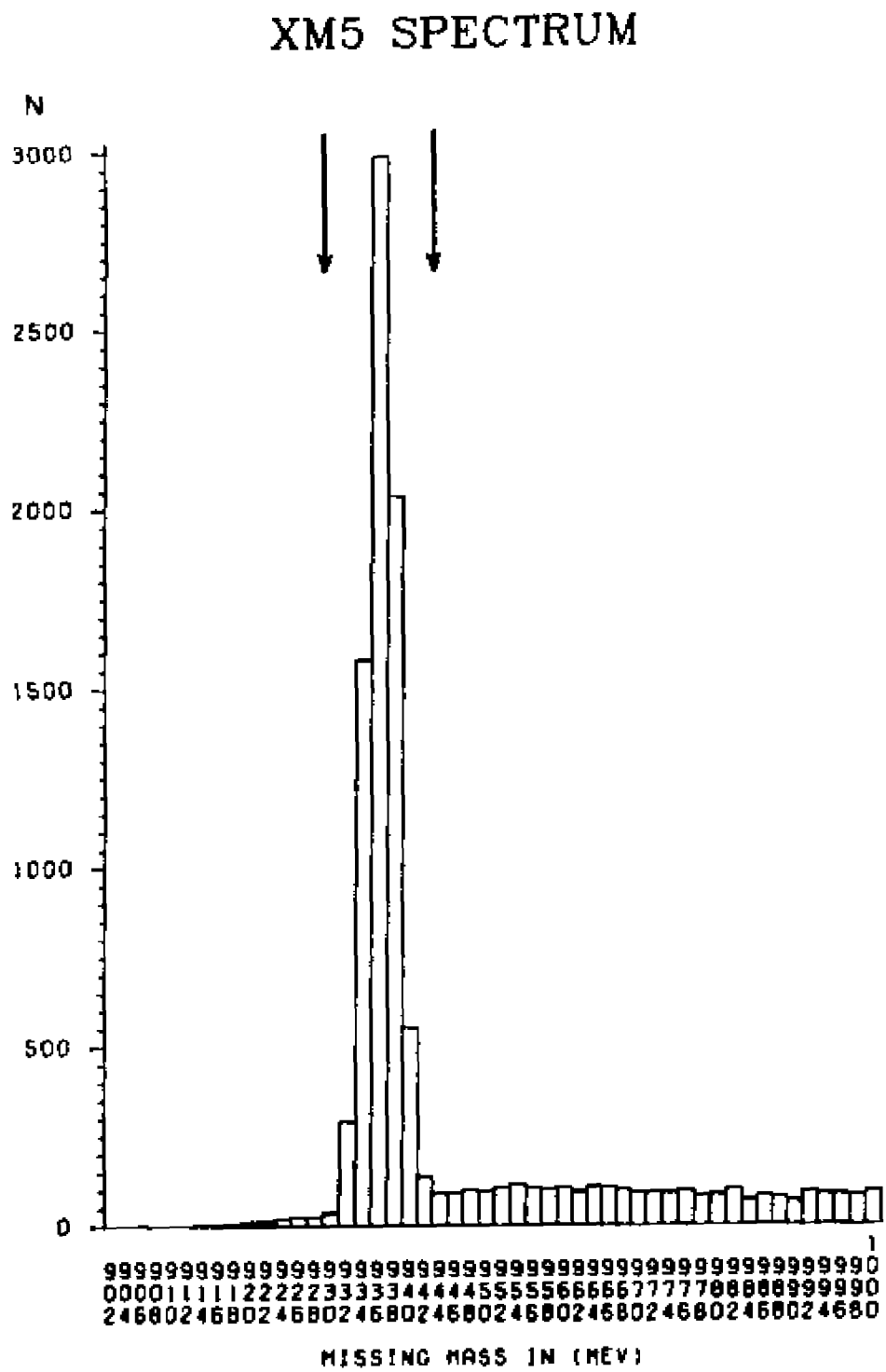
XM5 SPECTRUM
N
3000
2500
2000
1500
1000
500
0
MISSING MASS IN (MEV)

FIGURE 3.9

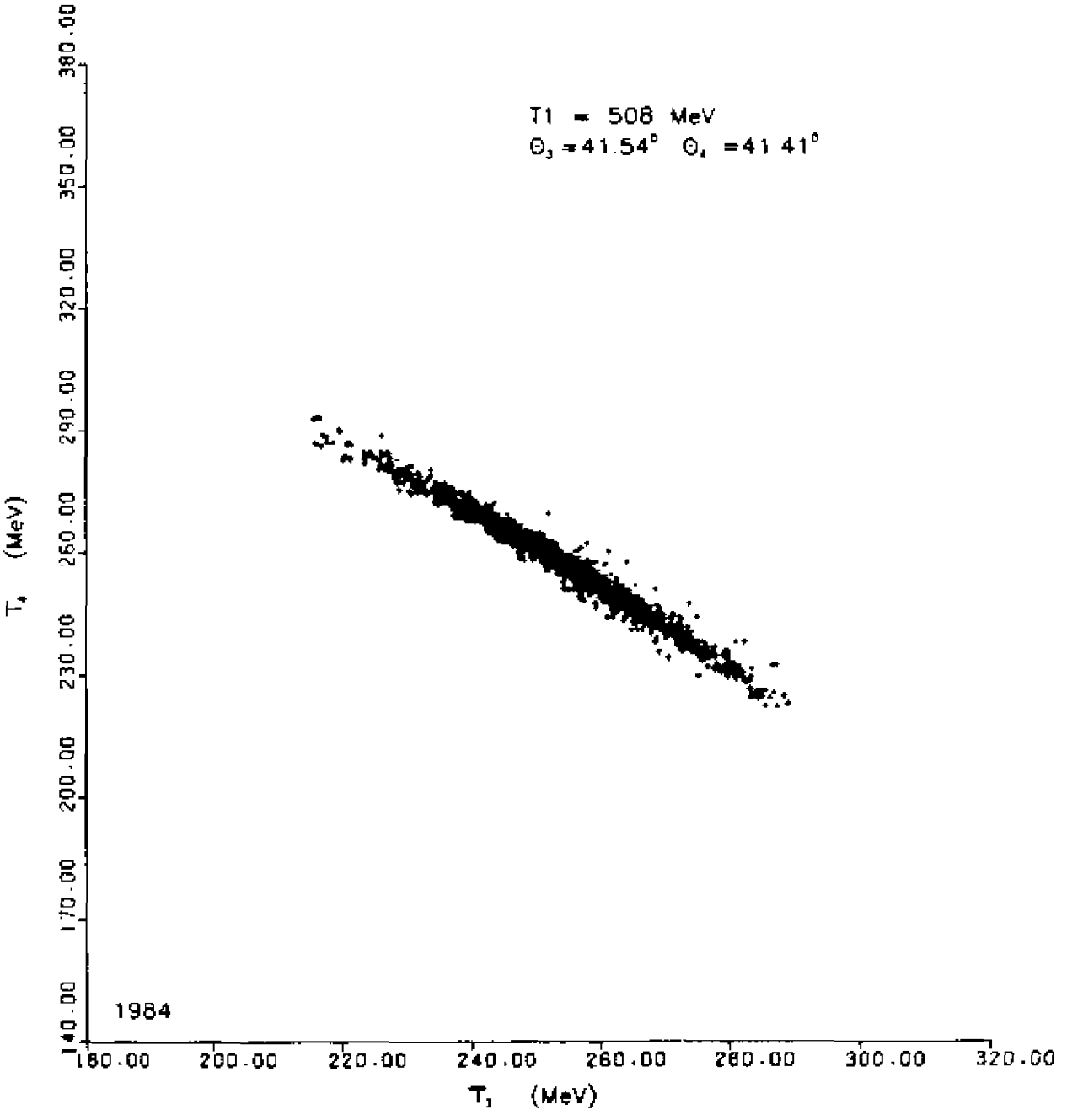
T1 = 508 MeV
Θ_3 = 41.54° Θ_4 = 41.41°
1984
T_4 (MeV)
T_3 (MeV)
140.00
170.00
200.00
230.00
260.00
290.00
320.00
350.00
380.00
180.00
200.00
220.00
240.00
260.00
280.00
300.00
320.00

FIGURE 3.10

where N is the total number of real events and N' is the number of accidental events.

ε_1 is the global correction factor for the multi wire proportional chamber (1983), and drift chamber (1984) efficiencies:

$$\varepsilon_1 = R_1/I_1$$

where I_1 is the number of particles incident on the wire planes and R_1 is the number of particles which satisfy the imposed requirements. The statistical error for chamber efficiencies ε_1 is given by

$$\text{relative error} = \sqrt{1/N_{\text{accepted}} - 1/N_{\text{presented}}}$$

Typical values for the efficiencies are 75% to 80%, and the statistical error is of the order of 0.2% for a typical (p, 2p) run.

LT is the live-time factor of the electronics and computer. The values of LT range from 60% to 85%, and the statistical error calculated as above is ≈0.1% for the typical (p, 2p) run at 41-41°.

ε_2 is a correction factor for the events lost from the full energy peak due to nuclear reactions in the NaI and Cu-absorber, and also due to the pile-up of pulses in the NaI detector. The ε_2 values range from 55% to 85% (Br-84) for our data, with systematic uncertainty of ± 1.%. ε_2 = 1.0 for the 41° and 30° high precision data.

I is the integrated incident proton beam current. It is determined from the secondary electron emission monitor (SEM) counts.

$$I = C \times N_S$$

N_s is the number of counts in SEM and C is a calibration constant which depends on the incident beam energy. The SEM was calibrated against a Faraday cup. The value of C was $9.446*10^8$ proton/count, reproducible to ±0.75%. The statistical error on I is $\approx 4.7*10^{-4}$ for a typical (p, 2p) run at 41°.

n_D is the number of ^2H nuclei per unit area, given by

$$n_D = \rho_D \, t_{tgt}/\cos \Theta$$

where ρ_D is the density of liquid deuterium, t_{tgt} is the thickness of the target cell and Θ is the rotation angle of the target relative to the incident beam. The target thickness t_{tgt} was determined as explained in section 3.4. All high precision (p, 2p) data at 41°, and the elastic pp-data at 41° were taken at the same target angle Θ = 0°, and thus are not affected by an uncertainty on Θ. However, the 30° (p, 2p) data were obtained with Θ = 25.°; an uncertainty on Θ of ±1° translates into ±0.7% systematic uncertainty on n_D.

The solid angle $\Delta\Omega_3$ was determined by software cut on the MWPC (1983 data) and from the size of the counters ΔE_{B0}, ΔE_{B1} in the 1984 data. The solid angle $\Delta\Omega_4$ was determined from the size of the ΔE_R counter. The uncertainties in solid angle are due to the finite size angular acceptance, beam spot and target thickness. The estimated uncertainty on $\Delta\Omega_3\Delta\Omega_4$ due to all above is less than 0.1%.

The total statistical uncertainties in the differential cross sections, calculated as the square root of the sum of the squares of the

fractional uncertainties in N, ϵ_1, LT, and ϵ_2, are given in the data tables. For the high precision data (table 3.7), we estimate the systematic error on the factor $\Delta\Omega_3\,\Delta T_3 n_D$ to be ±2.0% at 41° data, and 2.2% for the 30° data. At all other angles for the 1984-data, the systematic uncertainties become larger, because the detected energies are no longer as for hydrogen, and an energy cut (or missing mass cut) had to be applied; we estimate the total uncertainty to be ±3%. For the 1983-data, the total uncertainty is ±7%.

Chapter IV

MULTIPLE SCATTERING AND IMPULSE APPROXIMATION

4.1 INTRODUCTION

We have calculated the cross sections for the reaction ^{2}H(p, 2p)n including the IA pp and np scattering terms, as well as two other processes, rescattering of the projectile and final state interaction (FSI) among the two nucleons of the deuteron, following the work of Glauber (Gl-59) and Wallace (Wa-72). The calculation uses non relativistic NN amplitudes and noncovariant deuteron wave function; however, all kinematics are done relativistically. The calculation takes spin fully into account and it uses the Paris (La-81) NN - potential deuteron wave function and on-shell NN amplitudes from Arndt et al(Ar-83). The results will be compared with our data, for small neutron recoil as well as large neutron recoil. Section 4.2 contains the derivation of the cross section formulas from general multiple scattering theory. Section 4.3 describes the T matrix for the 3-nucleon final state in terms of 2-body NN amplitudes, and expresses these in terms of the helicity amplitudes. Section 4.4 describes the details of the spin algebra and antisymmetrization requirements. Section 4.5 contains the description of the IA. Results of the calculation are presented in section 4.6.

4.2 MULTIPLE SCATTERING

The reaction participants are labelled as

$$1 + 2 \rightarrow 3 + 4 + 5 \ ,$$

where 1 is the projectile proton, 2 is the deuteron nucleus, 3 and 4 are scattered and ejected protons and 5 is the recoil neutron.

We want to calculate the five-fold differential cross section for the proton-deuteron interaction leading to a 3-nucleon final state, in terms of the known proton-proton (p-p) and neutron-proton (n-p) amplitudes.

The differential cross-section in terms of the T-matrix is

$$d^9\sigma = V^2 \frac{E_1}{p_1} \frac{V^3}{(2\pi)^9} d^3p_3\, d^3p_4\, d^3p_5\, (2\pi)^4\, \delta^3(\vec{p}_3 + \vec{p}_4 + \vec{p}_5 - \vec{p}_1)$$
$$\times \frac{\delta(E_3 + E_4 + E_5 - E_1 - 2m + E_b)}{32\, V^5\, m_d\, E_3\, E_4\, E_5\, E_1} \left| \langle \vec{p}_3 \vec{p}_4 \vec{p}_5, L \,|\, T \,|\, \vec{0}, M; \vec{p}_1, S \rangle \right|^2 \quad (4.1)$$

In (4.1), $|\ \vec{0}, M; \vec{p}_1, S\ \rangle$ represents the initial state of the system were $\vec{0}$ is the deuteron laboratory momentum, M is the Z-component (in the beam direction) of deuteron spin, $\vec{p}_1$ is the momentum of the incident proton and S is the proton spin (S = α, β). $\langle\ \vec{p}_3\ \vec{p}_4\ \vec{p}_5,\ L\ |$ is the final state; here the first three entries are the final nucleon momenta, and L denotes a spin state for this system of three spin-1/2 particles.

The observed differential cross section, after the three-dimensional integration for $\vec{p}_5$ and $\vec{p}_4$ is carried out, is as follows:

$$\frac{d^5\sigma}{d\Omega_3 d\Omega_4 dT_3} = \frac{1}{(2\pi)^5\, 32\, m_d} \frac{p_3 p_4^2}{p_1 (E_5 p_4 - p_5 E_4 \cos\theta_{45})}$$
$$\times \frac{1}{6} \sum_{LMS} \left| \langle \vec{p}_3 \vec{p}_4 \vec{p}_5, L \,|\, T \,|\, \vec{0}, M; \vec{p}_1, S \rangle_A \right|^2 \quad (4.2)$$

The factor of 1/6 arises from averaging on the initial spin states; there are three deuteron spin states to be combined with the two spin states of the projectile proton. The dynamics of the inter-

action are contained in the T-matrix. The T-matrix elements must be antisymmetrized with respect to the proton variables. We want to express the T-matrix in terms of the T_{NN} matrices for the elastic p-p and p-n interactions.

The multiple scattering series which we are going to derive is more naturally expressed in terms of the quantum mechanical scattering matrix τ, which is the solution of the three-body Lippmann-Schwinger equation (Go-64).

$$\tau = V + V\ G\ \tau \qquad (4.3)$$

The two-body interaction potential V is given by: $V = V_{pn} + V_{p'n} + V_{p'p} \equiv V_1 + V_2 + V_3$; p' is the projectile proton and p and n are the deuteron constituents. Three body forces are neglected. It is a good approximation because the two constituents of the deuteron spend most of their time far away from each other. The root-mean-square nucleon separation is of the order of 4 fm, whereas the strong interaction range is of the order of the Compton wavelength of the pion, 1.4 fm. Hence, the probability is small for projectile proton and both nucleons being sufficiently close during the course of the collision for a significant three-body interaction, as long as the internal momentum is of order 200 MeV/c or less. In 4.3,

$$G = \frac{1}{E - H_0 + i\varepsilon}$$

$$H_0 = K_{p'} + K_p + K_n$$

where K are relativistic kinetic energy operators. E is the total

energy of the system. Let us now derive a multiple scattering expansion of τ:

$$\tau^i = V_i + V_i\, G\, \tau \quad \text{so that} \quad \tau = \sum_{i=1}^{3} \tau^i \tag{4.4}$$

We can now introduce the two-body free particle scattering matrices, τ_i, satisfying the two body Lippmann- Schwinger equation,

$$\tau_i = V_i + V_i\, G\, \tau_i \tag{4.5}$$

The presence of the third kinetic energy operator in H_o is permissible since the kinetic energy of this third non-interacting particle is constant.

The solution of equation (4.3) in terms of τ^i and τ_i is (Wo-68)

$$\begin{aligned} \tau = {} & \tau_1 + \tau_2 + \tau_3 + \tau_2\, G\, \tau^3 + \tau_3\, G\, \tau^2 \\ & + \tau_1\, G\, \tau^3 + \tau_1\, G\, \tau^2 + \tau_2\, G\, \tau^1 + \tau_3\, G\, \tau^1 + \ldots . \end{aligned} \tag{4.6}$$

The details are shown in Appendix A. Retaining only terms to first order in G, that is single and double scattering terms, we obtain:

$$\begin{aligned} \tau = {} & \tau_1 + \tau_2 + \tau_3 + \tau_2\, G\, \tau_3 + \tau_3\, G\, \tau_2 + \tau_1\, G\, \tau_3 \\ & + \tau_1\, G\, \tau_2 + \tau_2\, G\, \tau_1 + \tau_3\, G\, \tau_1 \end{aligned} \tag{4.6a}$$

We then make use of the identity

$$\frac{1}{E - H_o + i\varepsilon} = P\left[\frac{1}{(E - H_o)}\right] - i\pi\delta\,(E - H_o)$$

to split the double scattering contribution into two parts: a principal value part and an energy conserving part. The first part exactly cancels all the terms in equation (4.6) containing more than two τ_{pn} matrices. Furthermore the principal value part has been estimated to be much smaller than the energy conserving part. Using the above argument and equation (4.6) we get

$$\begin{aligned}\tau = {} & \tau_{p'p} + \tau_{p'n} + \tau_{pn} - i\pi\, \tau_{p'p}\, \delta(E-H_o)\, \tau_{p'n} \\ & - i\pi\, \tau_{p'n}\, \delta(E-H_o)\, \tau_{p'p} - i\pi\, \tau_{pn}\, \delta(E-H_o)\, \tau_{p'p} \\ & - i\pi\, \tau_{pn}\, \delta(E-H_o)\, \tau_{p'n} - i\pi\, \tau_{p'n}\, \delta(E-H_o)\, \tau_{pn} \\ & - i\pi\, \tau_{p'p}\, \delta(E-H_o)\, \tau_{pn} \qquad (4.7)\end{aligned}$$

The first three terms in equation (4.7) are impulse approximation terms. We neglect the third term because it represents an interaction of the two nucleons of the deuteron, with the projectile proton passing through undeflected.

Now we can obtain the expressions for the matrix elements of the various terms of equation (4.7). If final momentum of the projectile proton is $\vec{p}_3$, the first term of equation (4.7) can be expressed as

$$\langle \vec{p}_3, \vec{p}_4, \vec{p}_5, L | \tau_{pp'} | \vec{0}, M; \vec{p}_1, S \rangle = \sum_{q_n q_p L'} \langle \vec{p}_3 \vec{p}_4 \vec{p}_5, L | \tau_{pp'} | L' \vec{p}_1 \vec{q}_n \vec{q}_p \rangle \langle \vec{q}_p \vec{q}_n L' | \vec{0}, M; S \rangle$$

Where a complete set of proton-neutron plane wave states $\langle \vec{q}_p \vec{q}_n L' |$ is used. The spin states $| L' \rangle$ are three-particle states. The above expression simplifies as follows

$$\langle \vec{p}_3 \vec{p}_4 \vec{p}_5 L | \tau_{pp'} | \vec{0}, M; \vec{p}_1, S \rangle = \frac{(2\pi)^{3/2}}{V^{1/2}} \sum_{L'} \langle \vec{p}_3 \vec{p}_4, L | \tau_{pp'} | \vec{p}_1, -\vec{p}_5, L' \rangle \langle L' | \phi_M(\vec{p}_5) | S \rangle$$

The corresponding T matrix element is

$$\langle \vec{p}_3 \vec{p}_4 \vec{p}_5 L | T_{pp'} | \vec{0}, M; \vec{p}_1, S \rangle = (2\pi)^{3/2} (2m_d)^{1/2} \sum_{L'} \langle \vec{p}_3 \vec{p}_4 L | T_{pp'} | \vec{p}_1, -\vec{p}_5, L' \rangle \langle L' | \phi_M(\vec{p}_5) | S \rangle \quad (4.8a)$$

The relation between τ matrix and T matrix is as given below

$$\langle f | T | i \rangle = -(2\pi)^3 \delta^3(\vec{p}_f - \vec{p}_i) \prod_{\text{initial}} \frac{1}{\sqrt{2VE_i}} \prod_{\text{final}} \frac{1}{\sqrt{2VE_f}} \langle f | T | i \rangle$$

Similarly we find the expression for the T matrix element of the second term of eqn (4.7) to be

$$\langle \vec{p}_3 \vec{p}_4 \vec{p}_5 L | T_{p'n} | \vec{0}, M; \vec{p}_1, S \rangle = (2\pi)^{3/2} (2m_d)^{1/2} \sum_{L'} \langle \vec{p}_3 \vec{p}_5 L | T_{p'n} | \vec{p}_1, -\vec{p}_4, L' \rangle \langle L' | \phi_M(-\vec{p}_4) | S \rangle \quad (4.8b)$$

Fig. (4.1a) and (4.1b) shows the diagrams for above processes.

Following the same procedure, the matrix element of the fourth term in equation (4.7) is

$$\begin{aligned}
&\langle \vec{p}_3 \vec{p}_4 \vec{p}_5 L | T_{p'p} \, \delta(E - p_{p'} - p_n - p_p) \, T_{p'n} | \vec{0}, M; \vec{p}_1, S \rangle \, (-i\pi) \\
&= -i\pi \sum_{L'L''} \int V^{1/2} \frac{d^3 S_b}{(2\pi)^{3/2}} \int V \frac{d^3 q_{p_n}}{(2\pi)^3} \Bigg[\frac{\langle \vec{p}_3 \vec{p}_4 L | T_{p'p} | -\vec{q}_{p_n} \vec{S}_b L' \rangle}{\sqrt{2VE_3}\sqrt{2VE_4}\sqrt{2VE_{q_{p_n}}}\sqrt{2VE_{S_b}}} \\
&\quad \times (2\pi)^3 \delta^3(\vec{p}_3 + \vec{p}_4 + \vec{q}_{p_n} - \vec{S}_b) \, \delta(E - E_{q_{p_n}} - E_{S_a} - E_5) \\
&\quad \times \frac{\langle \vec{S}_a \vec{p}_5 L | T_{p'n} | \vec{p}_1 \vec{q}_{p_n} L'' \rangle}{\sqrt{2VE_{S_a}}\sqrt{2VE_5}\sqrt{2VE_1}\sqrt{2VE_{q_{p_n}}}} \langle L'' | \phi_M(q_{p_n}) | S \rangle \Bigg] (2\pi)^3 \delta^3(\vec{Q}_f - \vec{Q}_i)
\end{aligned}$$

Note that $\vec{q}_p = -\vec{q}_n$ is the internal momentum of the nucleons in the deuteron. After carrying out three-dimensional $\vec{S}_b$ integration and the q_n-

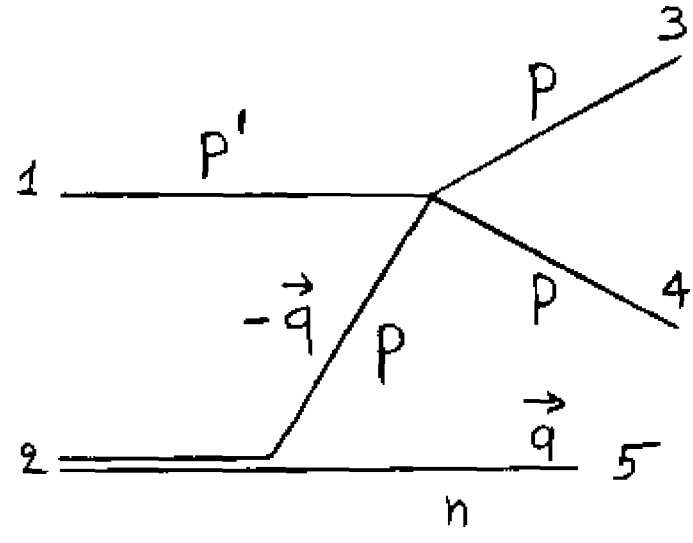

FIGURE 4.1a

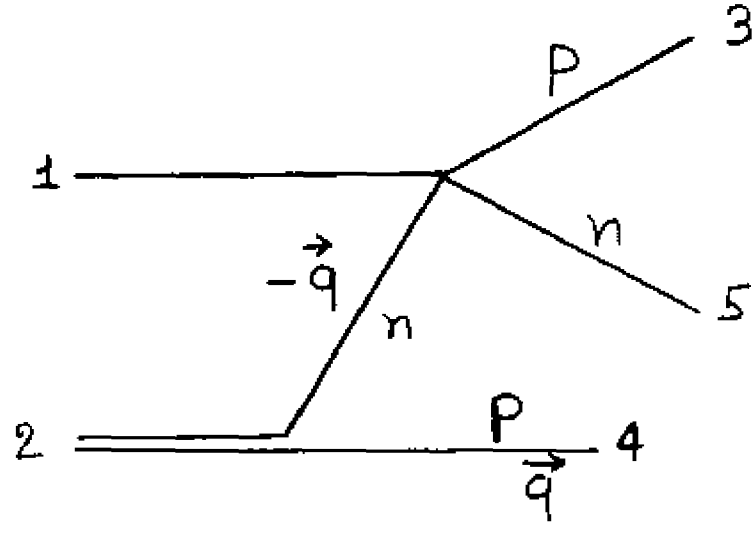

FIGURE 4.1b

integration along the direction of $\vec{p}_3 + \vec{p}_4$, we get the following expression:

$$\langle \vec{p}_3 \vec{p}_4 \vec{p}_5 L | T^a | \vec{0}, M_j \vec{p}_1 S \rangle = \frac{i\pi (2m_d)^{1/2}}{(2\pi)^{3/2}\, 4} \sum_{L'L''} \int_{(\vec{p}_3+\vec{p}_4)_\perp} d^2 q_t \langle \vec{p}_3 \vec{p}_4 L | T_{p'p} | \vec{p}_3 + \vec{p}_4 - \vec{q}_t, \vec{q}_t, L' \rangle$$

$$\times \frac{\langle \vec{p}_3 + \vec{p}_4 - \vec{q}_t, \vec{p}_5 L' | T_{p'n} | \vec{p}_1, -\vec{q}_t, L'' \rangle \langle L'' | \phi_M(\vec{q}_t) | S \rangle}{| (q_{0_{11}} + | \vec{p}_3 + \vec{p}_4 |) E(q_t) + q_{t_{11}} E(\vec{p}_3 + \vec{p}_4 - \vec{q}_t) |} \qquad (4.9a)$$

Implied in the above expression is that energy and momentum are conserved at each vertex. We also have replaced $\vec{q}_N$ by $\vec{q}$. The $(\vec{p}_3 + \vec{p}_4)$ under the integral sign indicates a two-dimensional integration over the component of $\vec{q}$ perpendicular to $\vec{p}_3 + \vec{p}_4$. The component of $\vec{q}$ parallel to $\vec{p}_3 + \vec{p}_4$, denoted by q_{11} is determined from energy and momentum conservation. The q-vector varies over a surface symmetrical with respect to the axis $\vec{p}_3 + \vec{p}_4$. Details about the integral element d^2q and the calculation of $|\vec{q}|$ are given in Appendix B.

Equation (4.9a) describes a double scattering process in which the proton projectile collides first with the neutron and then with the target proton as shown in Fig. 4.2a. For symmetric angles of particles 3 and 4, the p-n interaction is nearly 0° scattering and the p-p interaction 90°-scattering. This is true for all four diagrams.

Similarly, the T matrix element for the <u>fifth term</u> in equation (4.7) can be written as:

$$\langle \vec{p}_3 \vec{p}_4 \vec{p}_5 L | T^b | \vec{0}, M_j \vec{p}_1 S \rangle = \frac{i\pi (2m_d)^{1/2}}{(2\pi)^{3/2}\, 4} \sum_{L'L''} \int_{(\vec{p}_3+\vec{p}_5)_\perp} d^2 q_t \langle \vec{p}_3 \vec{p}_5 L | T_{p'n} | \vec{p}_3 + \vec{p}_5 - \vec{q}_t, \vec{q}_t, L' \rangle$$

$$\times \frac{\langle \vec{p}_3 + \vec{p}_5 - \vec{q}_t, \vec{p}_4 L' | T_{pp} | \vec{p}_1, -\vec{q}_t, L'' \rangle \langle L'' | \phi_M(\vec{q}_t) | S \rangle}{| (q_{0_{11}} + | (\vec{p}_3 + \vec{p}_5) |) E(q_t) + q_{t_{11}} (\vec{p}_3 + \vec{p}_5 - \vec{q}_t) |} \qquad (4.9b)$$

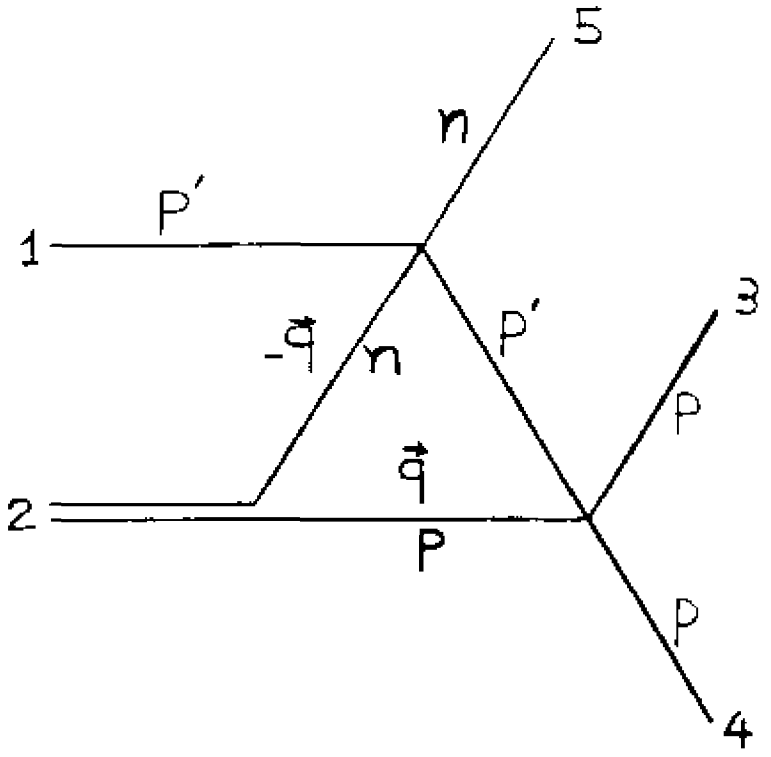

FIGURE 4.2a

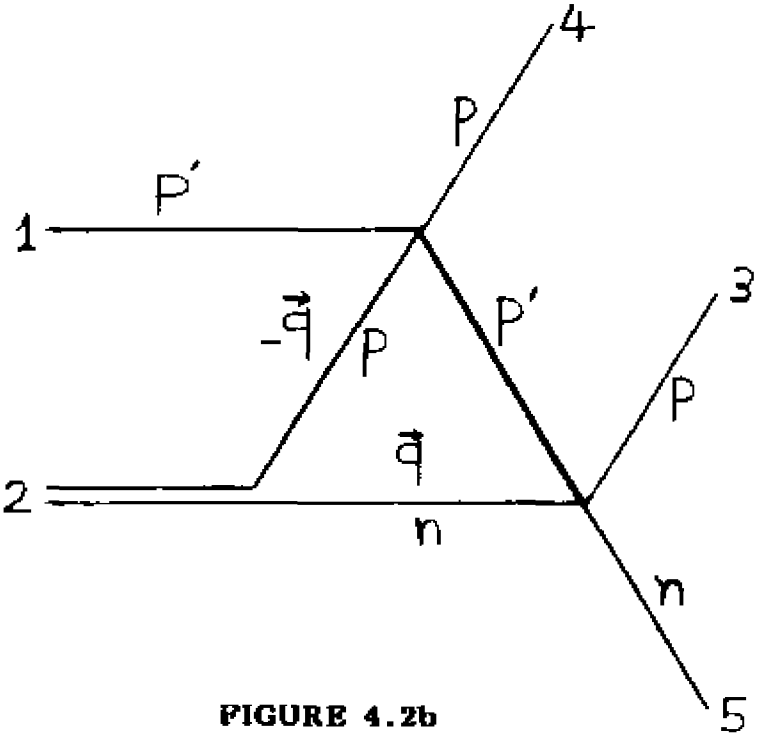

FIGURE 4.2b

Equation (4.9b) also describes a double scattering process; here the projectile proton first collides with the target proton and then with the neutron, as illustrated in figure 4.2b.

The sixth and seventh terms in equation (4.7) correspond to a final state interaction (FSI). The T matrix element for the sixth term is:

$$\langle \vec{p}_3 \vec{p}_4 \vec{p}_5 L | T^c | \vec{0}, M; \vec{p}_1 S \rangle = \frac{i\pi (2m_d)^{1/2}}{(2\pi)^{3/2}\, 4} \sum_{L'L''(\vec{p}_4+\vec{p}_5)_L} \int d^3q \langle \vec{p}_4 \vec{p}_5 L | T_{pn} | \vec{p}_4 + \vec{p}_5 - \vec{q}, \vec{q}, L' \rangle$$

$$\times \frac{\langle \vec{p}_3, \vec{p}_4 + \vec{p}_5 - \vec{q}, L' | T_{pp'} | \vec{p}_1, -\vec{q}, L'' \rangle \langle L'' | \phi_M(\vec{q}) | S \rangle}{| (q_{11} + |\vec{p}_4 + \vec{p}_5|) E(q) + q_{11} E(\vec{p}_4 + \vec{p}_5 - \vec{q}) |} \qquad (4.9c)$$

Equation (4.9c) describes the scattering of the projectile proton from the target proton, which then collides with the neutron. This is a single scattering process followed by a final state interaction of the target nucleons, as shown in fig. 4.2c.

The T matrix element for the seventh term in equation (4.7) is:

$$\langle \vec{p}_3 \vec{p}_4 \vec{p}_5 L | T^d | \vec{0}, M; \vec{p}_1 S \rangle = \frac{i\pi (2m_d)^{1/2}}{(2\pi)^{3/2}\, 4} \sum_{L'L''(\vec{p}_4+\vec{p}_5)_L} \int d^3q \langle \vec{p}_4 \vec{p}_5 L | T_{pn} | \vec{p}_4 + \vec{p}_5 - \vec{q}, \vec{q}, L' \rangle$$

$$\times \frac{\langle \vec{p}_3, \vec{p}_4 + \vec{p}_5 - \vec{q}, L' | T_{p'n} | \vec{p}_1, -\vec{q}, L'' \rangle \langle L'' | \phi_M(\vec{q}) | S \rangle}{| (q_{11} + |\vec{p}_4 + \vec{p}_5|) E(q) + q_{11} E(\vec{p}_4 + \vec{p}_5 - \vec{q}) |} \qquad (4.9d)$$

Equation (4.9d) describes the scattering of the projectile proton from the neutron, which then collides with the target proton. Again, this is a single scattering process followed by a final state interaction of the target nucleons as shown in figure 4.2d.

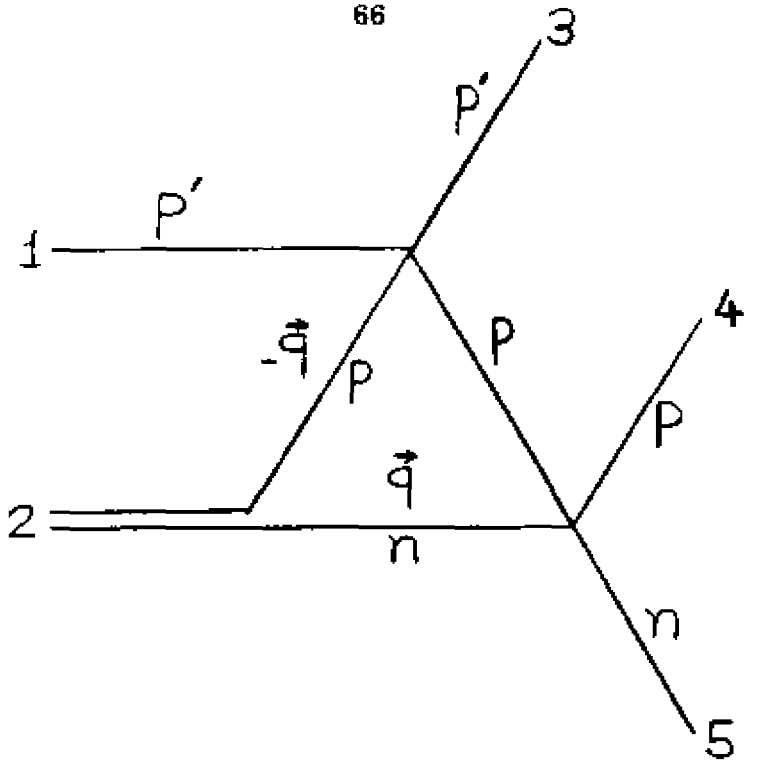

FIGURE 4.2c

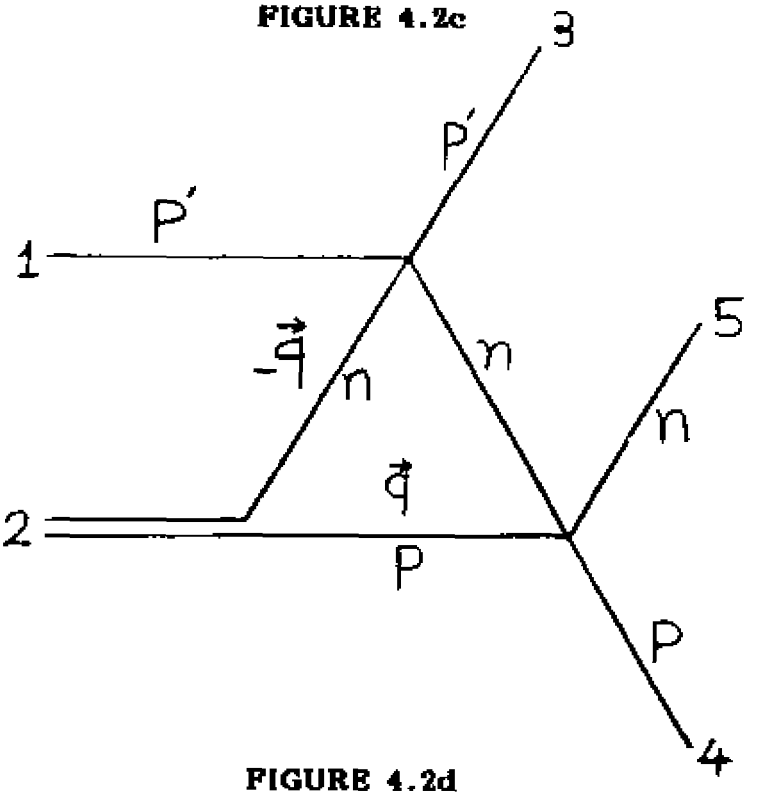

FIGURE 4.2d

We neglect the eighth and ninth terms of equation (4.7) because they correspond to an initial state interaction of the target nucleons before the projectile collides with the deuteron.

Finally, the T matrix calculated here is the sum of the single, double and final state interaction terms:

$$T = T_{pp'} + T_{p'n} + T^a + T^b + T^c + T^d \qquad (4.10)$$

Equation (4.10) antisymmetrized and substituted in equation (4.2) gives the differential cross section.

4.3 TWO-BODY T MATRICES

The relation between the on-energy-shell nucleon-nucleon T matrices and the non-relativistic center of mass scattering amplitude F_{CM} is

$$\langle \vec{p}_3', \vec{p}_4', m' | T_{NN} | \vec{p}_3, \vec{p}_4, m \rangle = 8\pi \sqrt{s} \langle m' | F_{cm}^{NN}(\theta, \varphi) | m \rangle \qquad (4.11)$$

where $s = (p_3 + p_4)^2 = (p_3' + p_4')^2$, θ is the CM scattering angle and φ the angle between initial and final reaction planes.

In (4.11), $| m \rangle$ is the spin wave function for a system of two spin-1/2 particles. Taking α and β to denote the spin-up and spin-down states, the triplet spin states are $| 1 \rangle = \alpha\alpha$, $| 0 \rangle = \frac{1}{\sqrt{2}} (\alpha\beta + \beta\alpha)$ and $| -1 \rangle = \beta\beta$. Using $m = s$ to denote the singlet state, $| s \rangle = \frac{1}{\sqrt{2}} (\alpha\beta - \beta\alpha)$.

The $< m' \mid F \mid m >$ are the singlet-triplet representation matrix elements M_{ss}, M_{11}, M_{10}, M_{1-1}, M_{01}, M_{00}, M_{0-1}, M_{-11}, M_{-10}, M_{-1-1} of Stapp et al. (St-57) Because of the symmetry properties of M's:

$$M_{11} = M_{-1-1} \qquad M_{01} = -M_{0-1}$$
$$M_{-11} = M_{1-1} \qquad M_{10} = -M_{-10}$$

there are only six independent M's, which are then calculated in terms of the helicity amplitudes H of Arndt et al. (Ar-83) The relation between the M's and H's are:

$$\begin{aligned} M_{SS} &= 2H_1/k \\ M_{00} &= 2\,(H_5\ \cos\theta + H_4\ \sin\theta)/k \\ M_{11} &= (H_3\ \cos\theta + H_4\ \sin\theta + H_2)/k \\ M_{10} &= -\sqrt{2}\,(H_5\ \sin\theta - H_4\ \cos\theta)/k \\ M_{01} &= -\sqrt{2}\,(-H_3\ \sin\theta + H_4\ \cos\theta)/k \\ M_{1-1} &= (H_2 - H_3\ \cos\theta - H_4\ \sin\theta)/k \end{aligned} \qquad (4.12)$$

Where k is the CM momentum and θ is the CM angle. The M matrix elements are non-antisymmetrized and antisymmetrization is performed in eqns. (4.17) to (4.21). The two spin-flip amplitudes M_{10} and M_{01} change sign, when (θ, φ) is replaced by $(\theta, \varphi + 180^\circ)$, and this property is taken into account systematically in the calculation. (St-57).

4.4 SPIN ALGEBRA

There are six initial and eight final spin states. Together they give 48 amplitudes. The 90° CM pp and pn interaction is dominated by spin flip contributions. As we have seen, this interaction figures importantly in all the diagrams. So it is important to include nucleon spin into our analysis.

Three spin 1/2 particles can be combined to give eight orthogonal spin wave functions (Wu-48):

$$
\begin{aligned}
|\,1\,\rangle &= \alpha_1\,\alpha_2\,\alpha_3 \\
|\,2\,\rangle &= \beta_1\,\beta_2\,\beta_3 \\
|\,3\,\rangle &= \frac{1}{\sqrt{3}}\,(\beta_1\,\alpha_2\,\alpha_3 + \alpha_1\,\beta_2\,\alpha_3 + \alpha_1\,\alpha_2\,\beta_3) \\
|\,4\,\rangle &= \frac{1}{\sqrt{3}}\,(\alpha_1\,\beta_2\,\beta_3 + \beta_1\,\alpha_2\,\beta_3 + \beta_1\,\beta_2\,\alpha_3) \\
|\,5\,\rangle &= \frac{1}{\sqrt{6}}\,(\beta_1\,\alpha_2\,\alpha_3 + \alpha_1\,\beta_2\,\alpha_3 - 2\alpha_1\,\alpha_2\,\beta_3) \\
|\,6\,\rangle &= \frac{1}{\sqrt{6}}\,(\alpha_1\,\beta_2\,\beta_3 + \beta_1\,\alpha_2\,\beta_3 - 2\,\beta_1\,\beta_2\,\alpha_3) \\
|\,7\,\rangle &= \frac{1}{\sqrt{2}}\,(\alpha_1\,\beta_2 - \beta_1\,\alpha_2\,)\,\alpha_3 \\
|\,8\,\rangle &= \frac{1}{\sqrt{2}}\,(\beta_1\,\alpha_2 - \alpha_1\,\beta_2)\,\beta_3
\end{aligned}
\qquad (4.13)
$$

The third state is taken to be that of the neutron. The spin wave functions $|\,1\,\rangle$ to $|\,6\,\rangle$ are symmetric with respect to proton spins, and $|\,7\,\rangle$ and $|\,8\,\rangle$ are antisymmetric. The presence of two protons in the final state requires that all physical states be antisymmetric with respect to all proton variables. As a consequence, the antisymmetrized final states of the system are

$$< \vec{p}_3\ \vec{p}_4\ \vec{p}_5,\ L \mid \pm < \vec{p}_4\ \vec{p}_3\ \vec{p}_5,\ L \mid, \qquad \begin{matrix} - \text{ For } L = 1 \text{ to } 6 \\ + \text{ For } L = 7,\ 8 \end{matrix} \qquad (4\text{-}14)$$

The initial states of the system can also be expressed in terms of the three-particle spin states (4.13). First we need to write the momentum space deuteron wave function in the form:

$$\Phi_M(\vec{q}) = \sum_{m=-1}^{1} \Phi_M^m(\vec{q}) \mid m > \qquad \text{where } \mid m > \text{ is the two-particle spin wave function.}$$

Then the six initial states of the system are:

$$\mid O,\ M;\ \vec{p}_1\ ,\ S > = \sum_{L=1}^{8} \mid \vec{p}_1\ ,\ L > \sum_{m=-1}^{1} < L \mid \Phi_M^m(\vec{q}) \mid m\ S > \qquad (4.15)$$

$$= \mid \vec{p}_1, \tfrac{1}{2} > \Phi_M^{\pm 1}(\vec{q}) + (\mid \vec{p}_1, \tfrac{3}{4} > \tfrac{\sqrt{6}}{3} - \mid \vec{p}_1, \tfrac{5}{6} > \tfrac{\sqrt{3}}{6}$$

$$+ \mid \vec{p}_1, \tfrac{7}{8} > \tfrac{1}{2}) \ \Phi_M^0(\vec{q})$$

$$+ (\mid \vec{p}_1, \tfrac{4}{3} > \tfrac{\sqrt{3}}{3} + \mid \vec{p}_1, \tfrac{6}{5} > \tfrac{\sqrt{6}}{6} - \mid \vec{p}_1, \tfrac{8}{7} > \tfrac{\sqrt{2}}{2}\ ) \ \Phi_M^{\pm 1}(\vec{q})$$

Where upper signs and numbers apply for S = α and the lower ones for S = β. The deuteron wave function components in (4.15) are

$$\Phi_1^1(\vec{q}) = \frac{u(q)}{q} Y_{00} + \frac{1}{\sqrt{10}} \frac{w(q)}{q} Y_{20}(\Theta_q, \varphi_q) = \Phi_{-1}^{-1}(\vec{q})$$

$$\Phi_1^0(\vec{q}) = -\frac{\sqrt{3}}{\sqrt{10}} \frac{w(q)}{q} Y_{21}(\Theta_q, \varphi_q) = \Phi_{-1}^0(\vec{q}) = -\Phi_0^1(\vec{q}) = \Phi_0^{-1}(\vec{q})$$

$$\Phi_1^{-1}(\vec{q}) = \frac{\sqrt{3}}{\sqrt{5}} \frac{w(q)}{q} Y_{22}(\Theta_q, \varphi_q) = \Phi_{-1}^1(\vec{q})$$

$$\Phi_0^0(\vec{q}) = \frac{u(q)}{q} Y_{00} - \frac{2}{\sqrt{10}} \frac{w(q)}{q} Y_{20}(\Theta_q, \varphi_q) \qquad (4.16)$$

where θ_q, φ_q are the angles of $\vec{q}$ relative to the spin quantification direction, here the beam direction. The S- and D-state radial wave functions of the deuteron are u(q) and w(q), respectively.

The spin states of equations (4.8) and (4.9) are three-particle spin states whereas those of equations (4.12) are two-particle spin states. Using equation (4.13) we then find the three-particle spin states for the nucleon-nucleon amplitudes. These amplitudes are written out in Appendix C.

Finally, using equations (4.8), (4.11), (4.14) and (4.15) we obtain the following T matrix element for the single scattering

$$T_{LMS}(\vec{q}) = (2\pi)^{3/2}(2m_d)^{1/2}(8\pi)\sqrt{5}\sum_{m_2=-1}^{+1}\left[A_{LMs}(\theta,\varphi) \mp A_{LMs}(\pi-\theta,\pi-\varphi)\right]\phi_m^M(\vec{q}) \quad (4.17)$$

where

$$A_{\substack{L\alpha \\ L-1\beta}} = \langle L|F^{pN}(\theta,\varphi)|^1_2\rangle$$

$$A_{\substack{L0\alpha \\ L0\beta}} = \langle L|F^{pN}(\theta,\varphi)|^3_4\rangle\frac{\sqrt{6}}{3} - \langle L|F^{pN}(\theta,\varphi)|^5_6\rangle\frac{\sqrt{3}}{6} + \langle L|F^{pN}(\theta,\varphi)|^7_8\rangle\frac{1}{2}$$

$$A_{\substack{L-1\alpha \\ L1\beta}} = \langle L|F^{pN}(\theta,\varphi)|^4_3\rangle\frac{\sqrt{3}}{3} + \langle L|F^{pN}(\theta,\varphi)|^6_5\rangle\frac{\sqrt{6}}{6} - \langle L|F^{pN}(\theta,\varphi)|^8_7\rangle\frac{\sqrt{2}}{2}$$

Where N = p or n.

θ or φ are determined from the initial and final momenta of the p-N interaction.

Similarly using equations (4.9), (4.11), (4.14) and (4.15) we get the following T matrix elements for the two double scattering diagrams and two FSI diagrams:

$$T^a_{LMS} = \frac{i\pi (2m_d)^{1/2} (8\pi)^2}{(2\pi)^{3/2}\, 4} \int_{(\vec{p}_3+\vec{p}_4)_\perp} d^2q_\perp \left[\sum_{m=-1}^{+1} \frac{a_{LMS}(\theta,\phi,\theta',\phi')\ \phi^m_M(\vec{q}_\perp)}{|(q_{\parallel} + |\vec{p}_3+\vec{p}_4|)E(\vec{q}) + q_{\parallel} E(\vec{p}_3+\vec{p}_4-\vec{q})|} \right.$$

$$\left. \mp \sum_{m=-1}^{+1} \frac{a_{LMS}(\pi-\theta,\pi+\phi,\theta',\phi')\ \phi^m_M(\vec{q}_\perp)}{|(q_{\parallel} + |(\vec{p}_3+\vec{p}_4)|)E(\vec{q}) + q_{\parallel} E(\vec{p}_3+\vec{p}_4-\vec{q})|} \right] \sqrt{s}\sqrt{s'} \qquad (4.18)$$

where the a's are found in appendix D and

$$s = (p_3 + p_4)^2$$

$$s' = (p_1 + q)^2$$

$$T^b_{LMS} = \frac{i\pi (2m_d)^{1/2} (8\pi)^2}{(2\pi)^{3/2}\, 4} \left\{ \int_{(\vec{p}_3+\vec{p}_5)_\perp} d^2q_\perp \left[\sum_{m=-1}^{+1} \frac{b_{LMS}(\theta,\phi,\theta',\phi')\ \phi^m_M(\vec{q}_\perp)\sqrt{s}\sqrt{s'}}{|(q_{\parallel} + |\vec{p}_3+\vec{p}_5|)E(\vec{q}) + q_{\parallel} E(\vec{p}_3+\vec{p}_5-\vec{q})|} \right] \right.$$

$$\left. \mp \int_{(\vec{p}_4+\vec{p}_5)_\perp} d^2q_\perp \left[\sum_{m=-1}^{+1} \frac{b_{LMS}(\theta,\phi,\theta',\phi')\ \phi^m_M(\vec{q}_\perp)\sqrt{s}\sqrt{s'}}{|(q_{\parallel} + |\vec{p}_4+\vec{p}_5|)E(\vec{q}) + q_{\parallel} E(\vec{p}_4+\vec{p}_5-\vec{q})|} \right] \right\} \qquad (4.19)$$

where the b's are found in Appendix D and

$$s = (p_{3 \text{ or } 4} + p_5)^2$$

$$s' = (p_1 + q)^2$$

$$T^c_{LMS} = \frac{i\pi (2m_d)^{1/2} (8\pi)^2}{(2\pi)^{3/2}\, 4} \left\{ \int_{(\vec{p}_4+\vec{p}_5)_\perp} d^2q_\perp \left[\frac{\sum_{m=-1}^{+1} c_{LMS}(\theta,\phi,\theta',\phi')\ \phi^m_M(\vec{q}_\perp)\sqrt{s}\sqrt{s'}}{|(q_{\parallel} + |(\vec{p}_4+\vec{p}_5)|)E(\vec{q}) + q_{\parallel} E(\vec{p}_4+\vec{p}_5-\vec{q})|} \right] \right.$$

$$\left. \mp \int_{(\vec{p}_3+\vec{p}_5)_\perp} d^2q_\perp \left[\vec{p}_4 \rightarrow \vec{p}_3 \right] \right\} \qquad (4.20)$$

where the c's are given in Appendix D and

$$s = (p_{3 \text{ or } 4} + p_5)^2$$

$$s' = (p_1 + q)^2$$

$$T^{d}_{LMS} = \frac{i\pi(2m_d)^{1/2}(8\pi)^2}{(2\pi)^{3/2}\,4}\left\{\int_{(\vec{p}_4+\vec{p}_5)_\perp} d^2q_\perp\left[\sum_{m=-1}^{+1}\frac{d_{LMS}(\theta\phi,\theta'\phi')\,\phi^{M}_{M}(\vec{q}_\perp)\sqrt{s}\,\sqrt{s'}}{|(q_{1\parallel}+|\vec{p}_4+\vec{p}_5|)E(\vec{q}_\perp)+q_{\perp}E(\vec{p}_4+\vec{p}_5-\vec{q}_\perp)|}\right]\right. \tag{4.21}$$

$$\left. \mp \int_{(\vec{p}_3+\vec{p}_5)_\perp} d^2q_\perp\,[\,\vec{p}_4 \to \vec{p}_3\,]\right\}$$

where the d's are given in Appendix D and

$$s = (p_{3 \text{ or } 4} + p_5)^2$$

$$s' = (p_1 + q)^2$$

Equations (4.17) - (4.21) combined with F amplitudes of Appendix 1C, the singlet-triplet representation matrix elements M's, equation (4.12), and the wave function formulas, equation (4.16), give the complete set of equations for calculating the single scattering, double scattering and FSI contributions. To obtain the differential cross section we substitute the T matrix (4.17) to (4.21) into equation (4.2). This completes the derivation of all the formulas one needs to calculate the ^{2}H(p, 2p)n differential cross sections.

4.5 IMPULSE APPROXIMATION

What is commonly referred to, both in the literature, and in Chapter 5, as the IA estimate of the cross section for (p, 2p) is the contribution of the first term in the multiple scattering expansion, formula (4.7). Expression (4.2) for the cross section can then be written as follows, when (4.17) only is used for the T-matrix:

$$\frac{d^5\sigma}{d\Omega_3 d\Omega_4 dT_3} = \frac{S p_4^2 p_3}{p_1(E_5 p_4 - p_5 E_4 \cos\theta_{45})} \sum_{m,m'} |\langle m' | F_{cm}^{pp}(\theta,\phi) | m \rangle|^2 |\phi(\vec{p}_5)|^2$$

$$= K \left(\frac{d\sigma}{d\Omega}\right)_{cm}^{pp} |\phi(\vec{p}_5)|^2 \qquad (4.22)$$

Where $|\Phi(\vec{P}_5)|^2$ is a theoretical single nucleon momentum distribution (SNMD) for the deuteron, which we take from the Paris NN-potential; $(d\sigma/d\Omega)_{CM}^{pp}$ is the proton-proton on-shell CM differential cross section and K is the kinematic factor.

4.6 RESULTS OF THE CALCULATION

We show here the detailed results of the calculation including the two IA graphs of Fig. 4.1a and 4.1b and the 4 graphs of Fig. 4.2a to 4.2c. Of particular interest are the results for the 41-4°-41.4° configuration, because this is the kinematics for which we have better data. Displayed in fig. 4.3 is the quantity (R-1) vs. neutron recoil momentum where R_{global} is the ratio of the cross section including all graphs, to the IA pp cross section alone

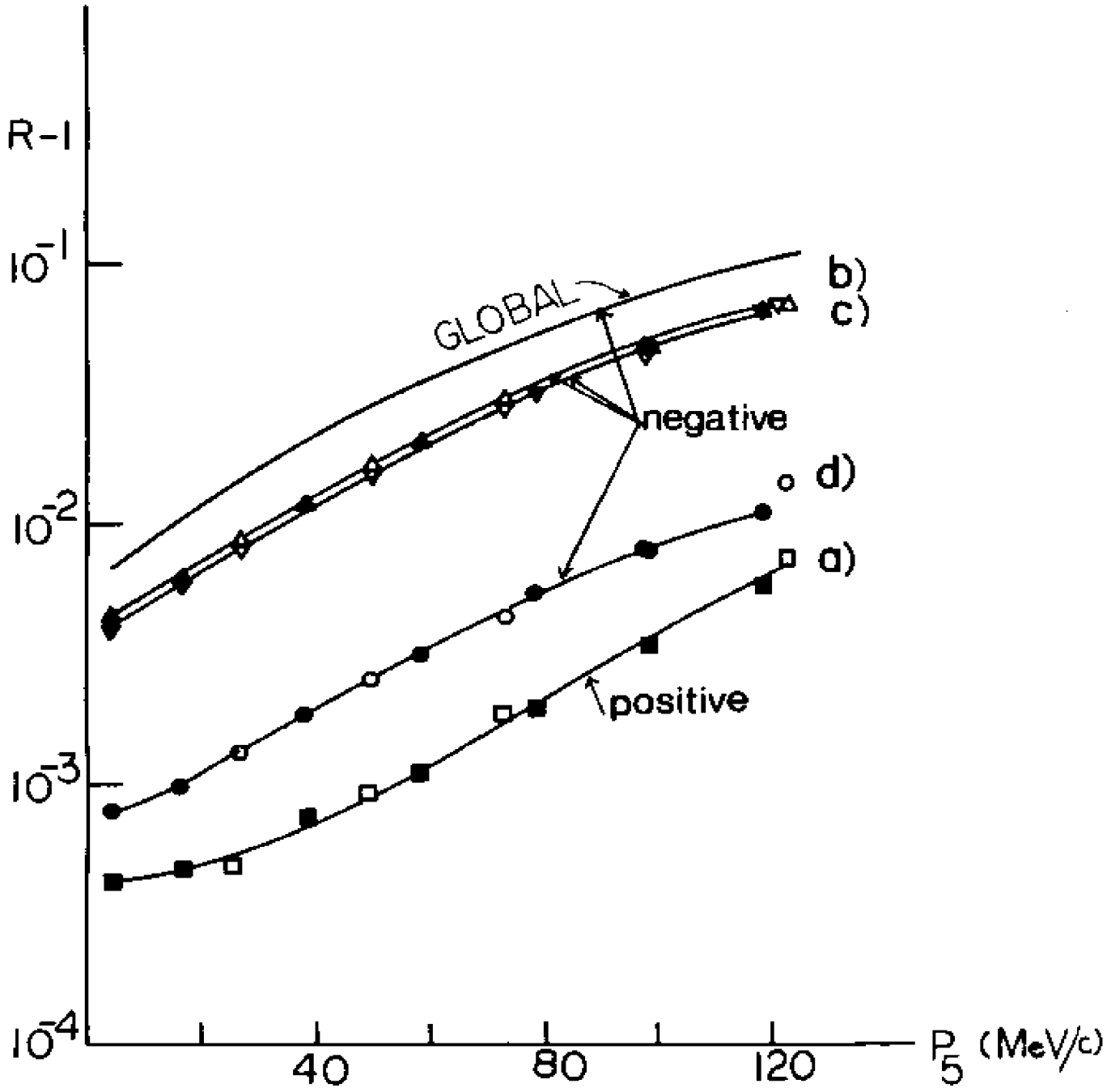
R-1
10^{-1}
10^{-2}
10^{-3}
10^{-4}
GLOBAL
b)
c)
negative
d)
a)
positive
40
80
120
P_5 (MeV/c)

FIGURE 4.3

$$R_{global} = \left| T_{IA}^{pp} + T_{IA}^{pn} + \sum_{i=a}^{d} \frac{T^i}{4\pi} \right|^2 \Big/ \left| T_{IA}^{pp} \right|^2$$

Similarily, we define (4.23)

$$R_i = \left| T_{IA}^{pp} + T_{IA}^{pn} + \frac{1}{4\pi} T^i \right|^2 \Big/ \left| T_{IA}^{pp} \right|^2$$

where i = a, b, c, d for each diagram.

Thus (R-1) is the percentage correction to be applied to the pp IA-term according to our results. The curves labelled a) through d) correspond to the inclusion of one of the graphs of fig. 4.2 at a time. The curve labelled "global" correspond to all graphs included. Only graph a) contributes a positive correction to the IA. Graphs b), c) and d) produce a negative correction; added all together the 4 graphs result in a negative correction to the IA.

A primary criterium to check the correctness of the calculation results was symmetry. We expect the results to be symmetric about the minimum recoil when the two proton angles are equal (see further discussion of this point in the next chapter). In fact, all results for symmetric angle kinematics have been found to be symmetric. In fig. 4.3 the dots correspond to p_3 being smaller than $\tilde{p}_3$ (central p_3) (i.e. $\vec{p}_5$ pointing on the same side as $\vec{p}_3$) and the crosses are for p_3 larger than $\tilde{p}_3$ (i.e. $\vec{p}_5$ pointing on the same side as $\vec{p}_4$). It is obvious in fig. 4.3 that the results are symmetric for all individual graphs, as well as globally. We have also checked that we find the same results at 600 MeV as shown in Wallace's reference (Wa-71)

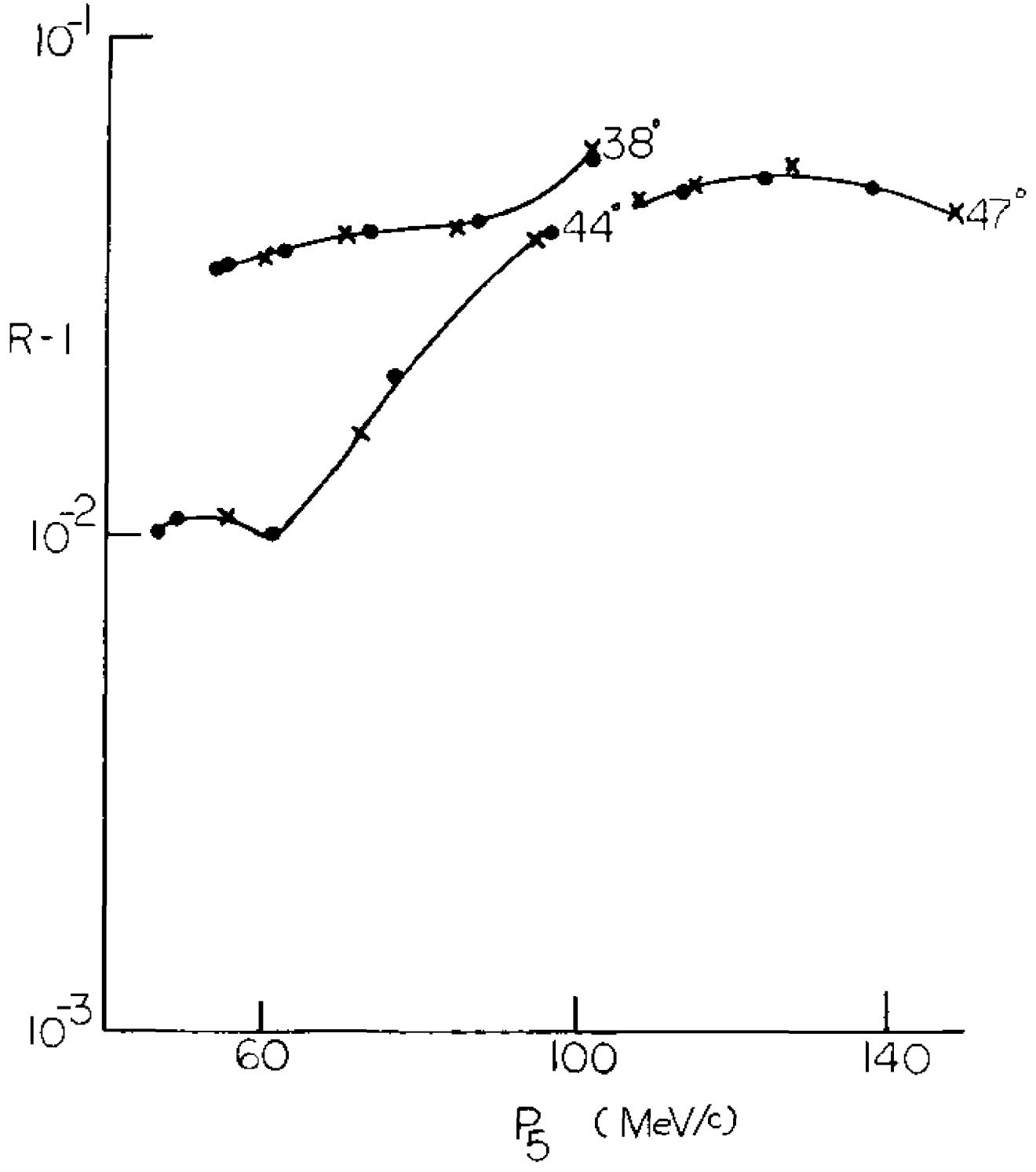

FIGURE 4.4

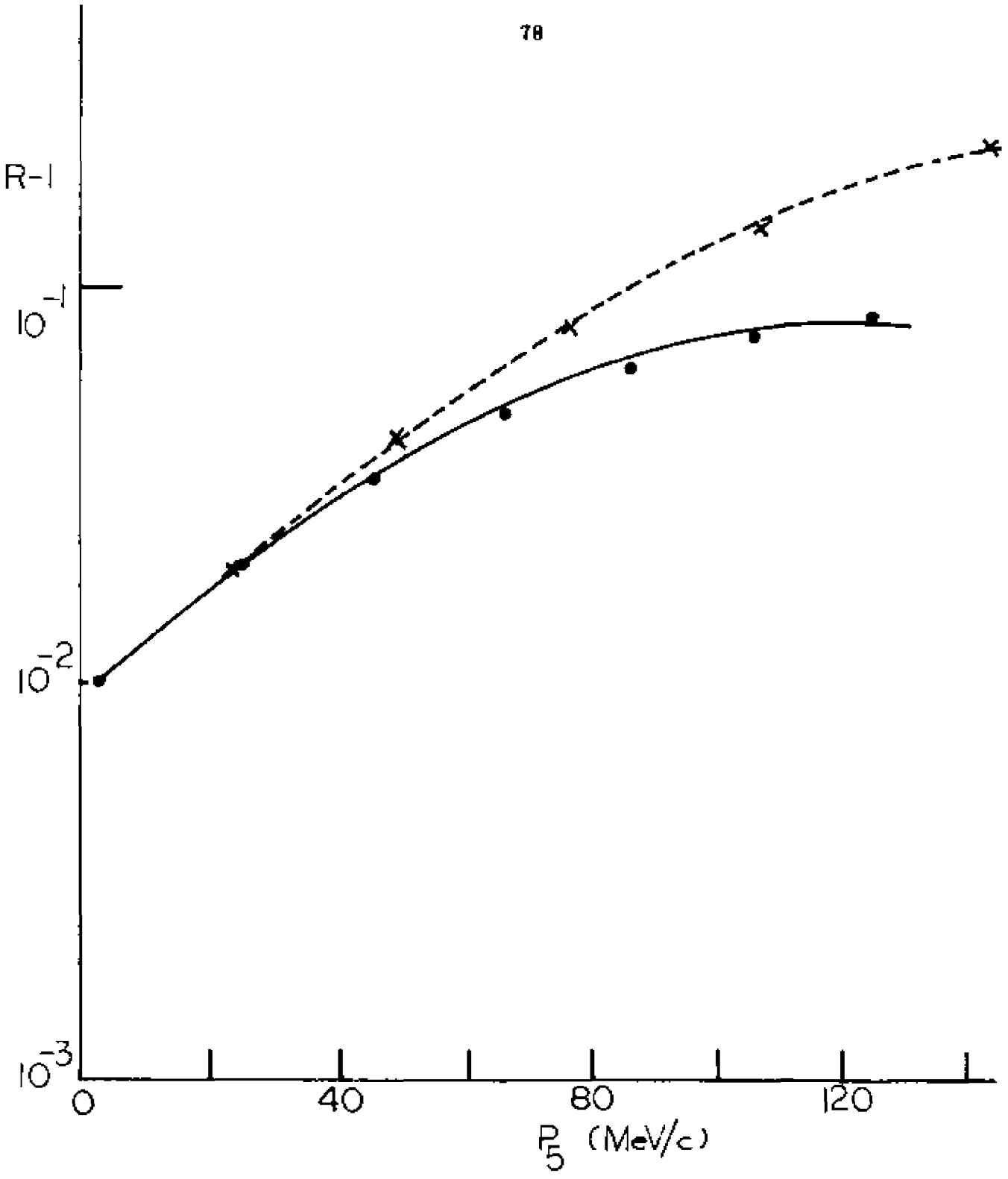

FIGURE 4.5

Fig. 4.4 shows the values of (R-1) for all graphs combined vs. the neutron recoil momentum for the symmetric angle pairs at 38°, 44° and 47°. Here also the results are symmetric about the minimum recoil as expected. Finally, fig. 4.5 shows the global values of (R-1) vs. neutron recoil momentum for the asymmetric angle pair 30° - 53.75°. In this case the results need not be symmetric about minimum recoil, and indeed they are not. We also notice from all the graphs shown, that the correction due to multiple scattering is minimum at minimum recoil. This is because at minimum recoil momentum the cross section is dominated by the IA process, whereas as p_5 increases the multiple scattering contributions become increasingly important.

Finally, fig. 4.6 shows R as a function of angle for symmetric angles and momenta p_3 and p_4. The correction due to multiple scattering is negative and small up to about 54°. Then the correction becomes positive and it rises very fast. Nearly all of the contribution to this fast rise comes from the first graph, although the contribution from the other three graphs becomes positive also. In the same figure, the contribution due to IA np scattering is shown separately. The IA np process nearly doubles the cross section at 66°.

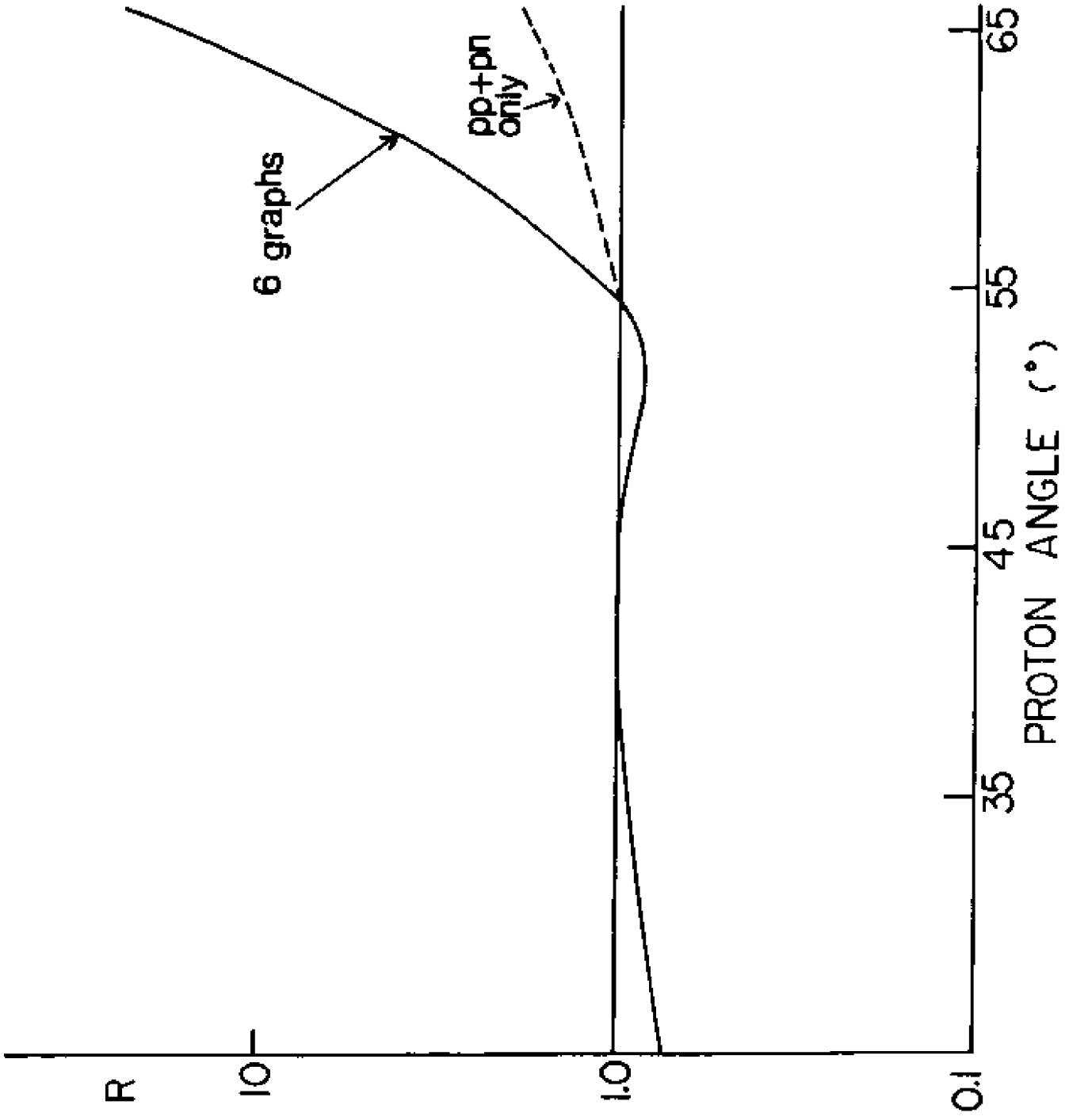

FIGURE 4.6

Chapter V

RESULTS AND DISCUSSION

5.1 INTRODUCTION

The results presented in this chapter concern the reaction ^{2}H (p, 2p)n, i.e.,

$$p + {}^{2}H \rightarrow p + p + n$$
$$1 + 2 \rightarrow 3 + 4 + 5$$

where 1 is the incident proton, 2 is the target deuteron, 3 and 4 are the detected scattered and knocked-out protons, respectively, and 5 is the recoil neutron.

Section 5.2 describes the kinematics for the reaction ^{2}H (p, 2p)n. In Section 5.3 we present the results for small neutron recoil momenta for several symmetric proton angle pairs and one asymmetric angle pair. In Section 5.4 we present the results for large neutron recoil momenta for several symmetric and asymmetric angle pairs. We compare our results with the prediction of the impulse approximation (IA) and with those of our multiple scattering calculation (described in chapter IV). We also compare our results with previous (p, 2p) and (e, e'p) results.

5.2 KINEMATICS

In order to determine the final state entirely (kinematically complete reaction), one needs to measure 12 variables, 9 components of momenta and 3 masses, for the 3-nucleon final state. The masses of the 2 protons are determined from their TOF and dE/dx (see section 2.6), and we require the momentum and energy to be conserved in the initial and final states (4 relations); so finally we need to measure 12 - 2 - 4 = 6 additional independent variables in general to determine the final state entirely. We measured p_3, Θ_3, φ_3, T_4, Θ_4 and φ_4 for each detected event (see figure 5.1). The 41° and 30° data will be analyzed without the T_4- information. The recoil momentum p_5 was then obtained from p_4 calculated as in eqn. 5.9.

Most of the data will be presented in the form of a momentum density, Φ^2, as a function of the neutron recoil momentum p_5. Momentum and energy conservation are used to calculate p_5 for each event:

$$\vec{p}_1 = \vec{p}_3 + \vec{p}_4 + \vec{p}_5 \qquad (5.1)$$

$$E_1 + m_2 = E_3 + E_4 + E_5 \qquad (5.2)$$

The invariant mass of particles i and j is

$$M_{ij}^2 = \sqrt{E_{ij}^2 - \vec{P}_{ij}^2}, \qquad (5.3)$$

where $$E_{ij} = E_i + E_j = E_1 + m_2 - E_k, \qquad (5.4)$$

and $$\vec{P}_{ij} = \vec{p}_i + \vec{p}_j = \vec{p}_1 - \vec{p}_k, \qquad (5.5)$$

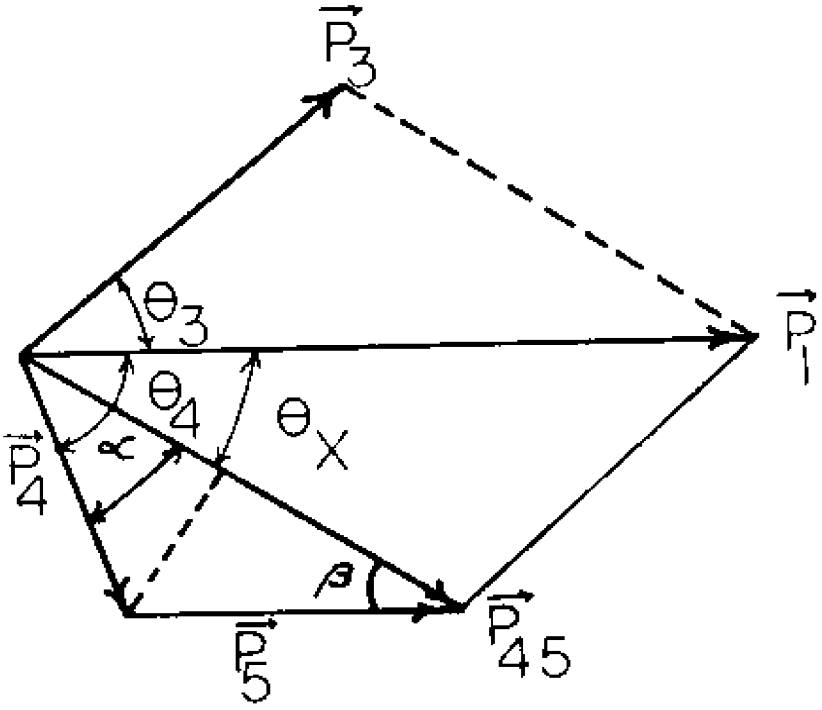
$\vec{P}_3$
θ_3
$\vec{P}_1$
θ_4
θ_X
$\vec{P}_4$
α
β
$\vec{P}_5$
$\vec{P}_{45}$

FIGURE 5.1

where i, j, k are from 3 to 5. Using equations (5.1) to (5.5) one can write

$$E_5^2 = (E_{45} - E_4)^2, \tag{5.6}$$

$$p_5^2 = (\vec{P}_{45} - \vec{p}_4)^2. \tag{5.7}$$

Equations (5.6 - 5.7) give

$$m_5^2 = (E_{45} - E_4)^2 - (\vec{P}_{45} - \vec{p}_4)^2 \tag{5.8}$$

Equation 5.8 is a quadratic relation from which $| p_4 |$ can be calculated (see figure 5.1); the result is

$$p_4 = \frac{P_{45}\cos\alpha\, E_x^2 + E_{45}\sqrt{E_x^4 - 4m_4^2(E_{45}^2 - P_{45}^2\cos^2\alpha)}}{2(E_{45}^2 - P_{45}^2\cos^2\alpha)} \tag{5.9}$$

where $$c_x^2 = M_{45}^2 + m_4^2 - m_5^2,$$

$$\alpha = \theta_4 - \theta_x,$$

and $$\theta_x = \tan^{-1}(p_3 \sin\theta_3 / (p_1 - p_3\cos\theta_3))$$

Now p_5 can be obtained from (5.9)

$$p_5 = p_4 \sin\alpha/\sin\beta \tag{5.10}$$

where $\beta = \tan^{-1}(p_4 \sin\alpha/(P_{45} - p_4\cos\alpha))$

The momentum density Φ^2 is obtained from the measured cross sections using the IA as follows:

$$| \Phi(\vec{p}_5) |^2 = \frac{d^5\sigma/d\Omega_3\, d\Omega_4\, dT_3}{K\,(d\sigma/d\Omega)_{CM}^{pp}} \tag{5.11}$$

where K is a kinematic factor given by:

$$K = p_3\, p_4^2\, M_{34}^2/p_1(E_5\, p_4 - E_4\, p_5\cos\theta_{45})$$

and $(d\sigma/d\Omega)^{pp}_{CM}$ is the CM pp on-shell differential cross section obtained from the VPI phase-shifts (Ar-83) at the collision energy T_{34} and CM angle δ_3 as follows:

$$T_{34} = (M_{34}^2 - (m_3 + m_4)^2)/2m_3$$
$$\delta_3 = \cos^{-1}((\gamma p_3 \cos\theta_{334} - \eta E_3)/p_3^{CM})$$

where p_3 and E_3 are laboratory frame quantities, p_3^{CM} is the momentum of particle 3 in the CM-system of particles 3 and 4,

$$\vec{\eta} = (\vec{p}_3 + \vec{p}_4)/M_{34}\ , \quad \gamma = (E_3 + E_4)/M_{34}$$

and θ_{334} is the laboratory angle between $\vec{p}_3$ and $\vec{p}_3 + \vec{p}_4$.

$|\ \Phi(\vec{p}_5)\ |^2$ is thus the result of the experiment, when the IA is used. The physical interpretation of the Φ^2-spectra presented in the next sections is thus as follows; in the absence of any contribution other than single pp scattering, it would be the deuteron single nucleon momentum density. But because other contributions are always present to some degree, Φ^2 is in fact not the true momentum distribution.

The calculated value of p_5 using (5.10) is then corrected using a Monte Carlo simulation including the finite acceptance of the detectors. Monte Carlo events are generated by choosing 5 independent variables (p_3, θ_3, φ_3, θ_4 and φ_4) of the experiment uniformly over the intervals defined by the experimental geometry, and assuming the 3 nucleon masses. Each event is then weighted according to the theoretical probability for the neutron recoil of the event. For each energy interval, T_3, one observes a distribution of p_5 values due to the finite solid angles, as well as finite target thickness and beam size.

Furthermore, multiple scattering in the target deuterium and assorted foils is included. The most likely value of p_5 is then determined. Calling the most likely value p_5 (MC), the results of the Monte Carlo simulation for $\Theta_3 = \Theta_4 = 41.41^\circ$ are shown in fig. 5.2 as a function of the p_5 values calculated from (5.10); the correction is largest near zero recoil.

5.3 SMALL NEUTRON RECOIL DATA

One-nucleon knock-out reactions like (p, 2p) and (e, e'p) are studied in order to determine the single nucleon momentum distribution of a bound nucleon in a nuclear system. In the quasi-free scattering domain (i.e., small recoil region), one would expect the IA to be a good approximation, as the distortions are small in the energy range of interest here; also the proton knocked out is nearly on-shell in this region. We present first our data in this domain of small neutron recoil momenta (Pu-85, Pu-85a).

All the data displayed in this section and section 5.4 are tabulated in data tables 1 through 16 (see TABLE CAPTIONS); the uncertainties in these tables are statistical only; random and target empty corrections have been made where necessary.

Fig. 5.3 shows the measured cross sections for the 41.54° - 41.41° angle pair and for the solid angles $\Delta\Omega_3 = 0.528$ msr and $\Delta\Omega_4 = 1.19$ msr., as a function of T_3, the energy of one of the detected protons. Statistical error bars are smaller than the size of the data points. The overall systematic uncertainty is estimated to be ±2.0% for cross

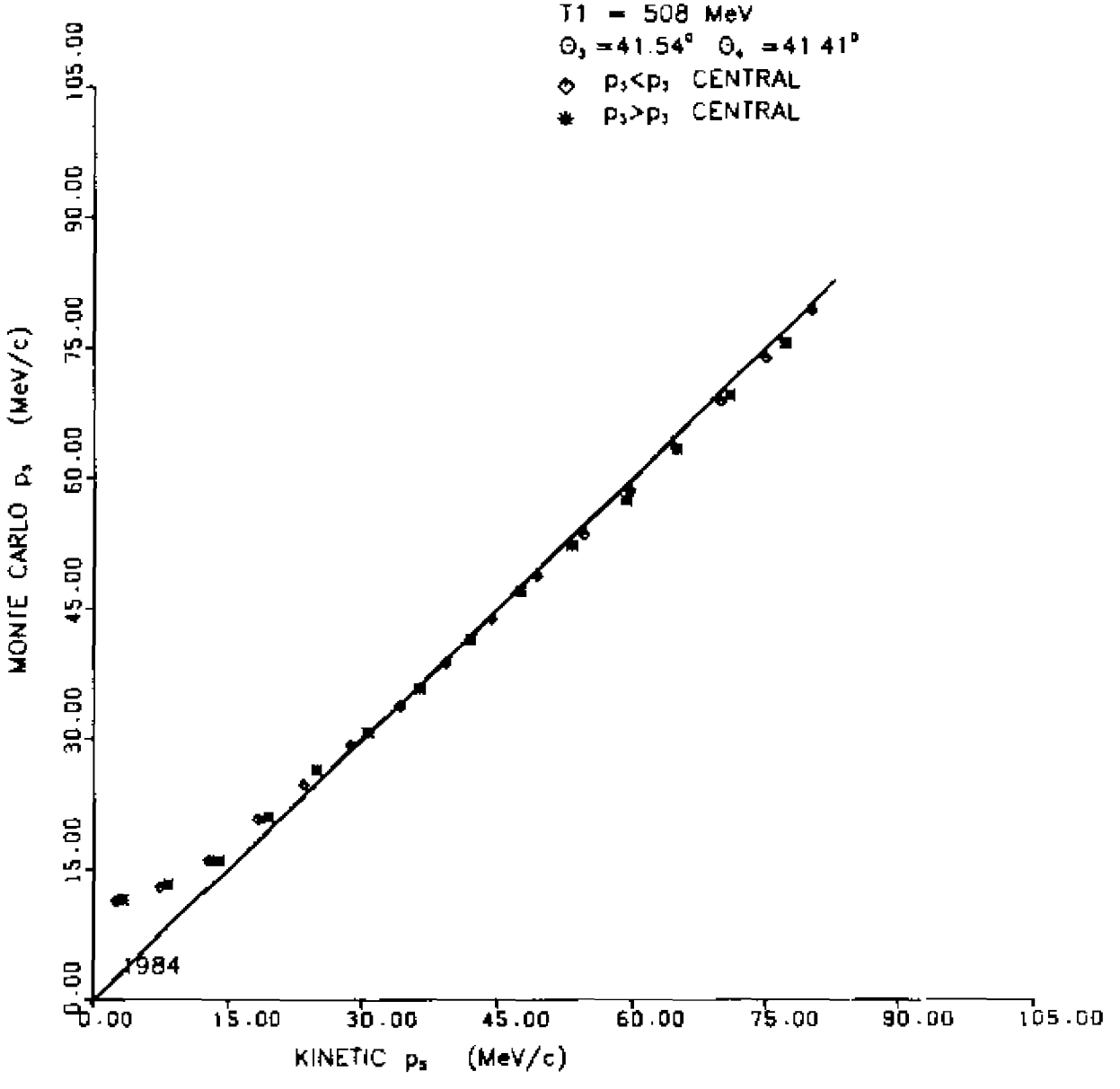
T1 = 508 MeV
Θ3 =41.54° Θ4 =41 41°
◇ p3<p3 CENTRAL
✱ p3>p3 CENTRAL
MONTE CARLO p3 (MeV/c)
KINETIC p3 (MeV/c)
0.00
15.00
30.00
45.00
60.00
75.00
90.00
105.00
1984

FIGURE 5.2

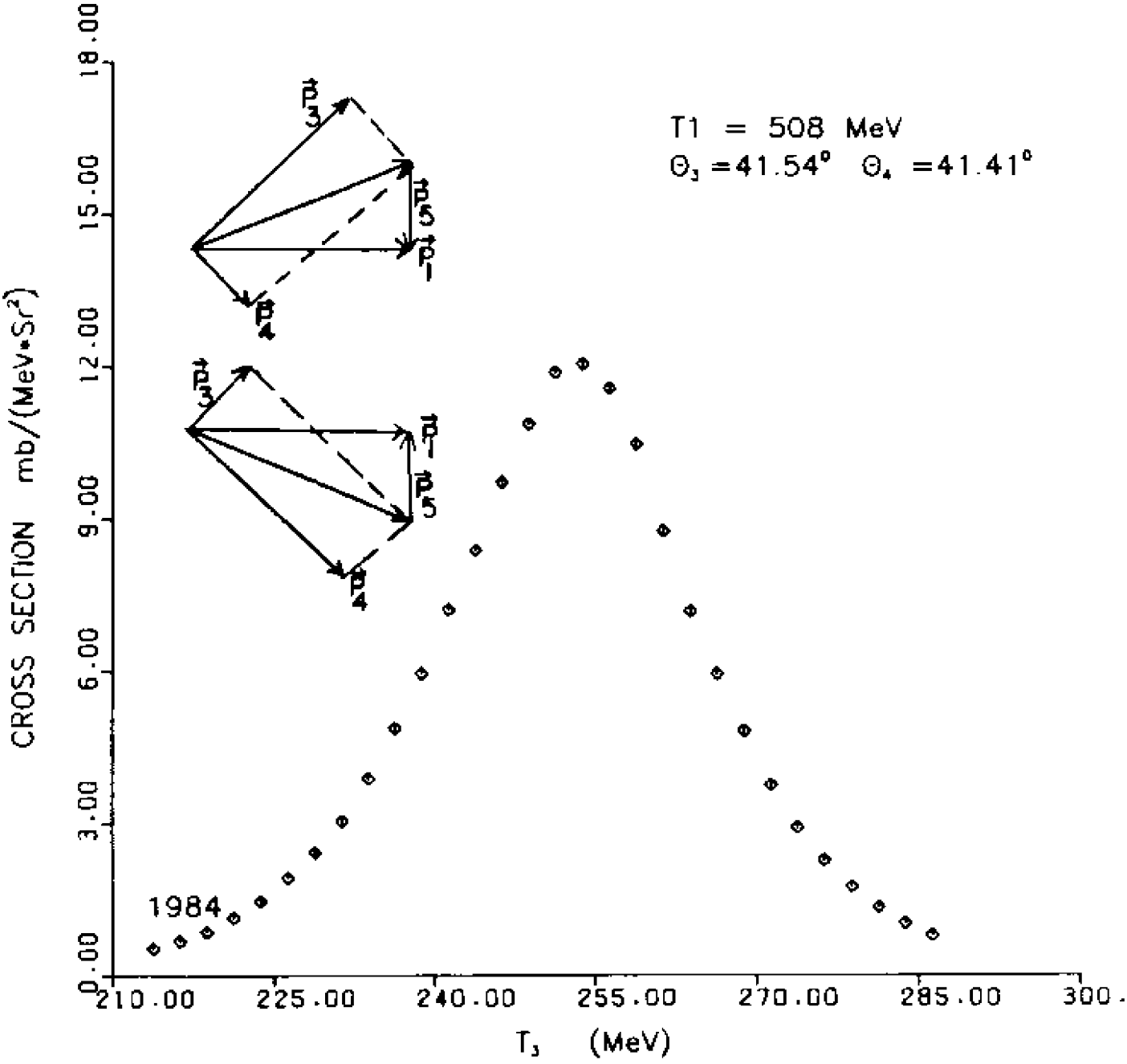
T1 = 508 MeV
Θ3 =41.54° Θ4 =41.41°
CROSS SECTION mb/(MeV•Sr²)
T3 (MeV)
1984
0.00
3.00
6.00
9.00
12.00
15.00
18.00
210.00
225.00
240.00
255.00
270.00
285.00
300.

FIGURE 5.3

sections (details are given in section 3.6). The cross sections are nearly symmetric about the minimum recoil, which occurs at T_3 = 253 MeV and is zero kinematically. This minimum recoil is approximately 10 Mev/c when resolution is taken into account. This symmetry in cross sections occurs because of the mirror symmetry of the kinematics. The value of $|\vec{p}_5|$ for $p_3 - \delta p_3$ is the same as for $p_3 + \delta p_3$, as shown in fig. 5.3.

The internal momentum density Φ^2 corresponding to the data in fig. 5.3 is shown in fig. 5.4 as a function of the neutron recoil momentum p_5. Φ^2 is obtained from eqn. (5.11) and p_5 from the Monte Carlo results in fig. 5.2. Thus the data are corrected for resolution. When compared to the density of the Paris (La-81) deuteron wave function Φ^2_{Paris}, the data agree rather nicely in shape, but are below the theoretical distribution by 4.7 to 14.6% over the range of neutron recoil momenta 13 to 80 Mev/c. We could not show the data points at recoil momenta smaller than 13 MeV/c, because of the hydrogen contamination in the deuterium target. To find the amount of hydrogen contamination in the target, we analyzed the data with very small solid angle by putting software cuts. The hydrogen peak is seen very clearly for solid angle $\Delta\Omega_3$ = .0327 msr, as shown in fig. 5.5, where it does not occur at the energy of zero recoil in (p, 2p), but somewhat higher. The amount of hydrogen in the deuterium was found to be $^1H/^2H = 1.5\ 10^{-3}$.

It was found necessary to adjust the central values of the angles on the MRS-side to achieve precise symmetry between the low-p_3 and high-p_3 values of Φ^2. For the large solid angle data, Θ_3 = 41.54°,

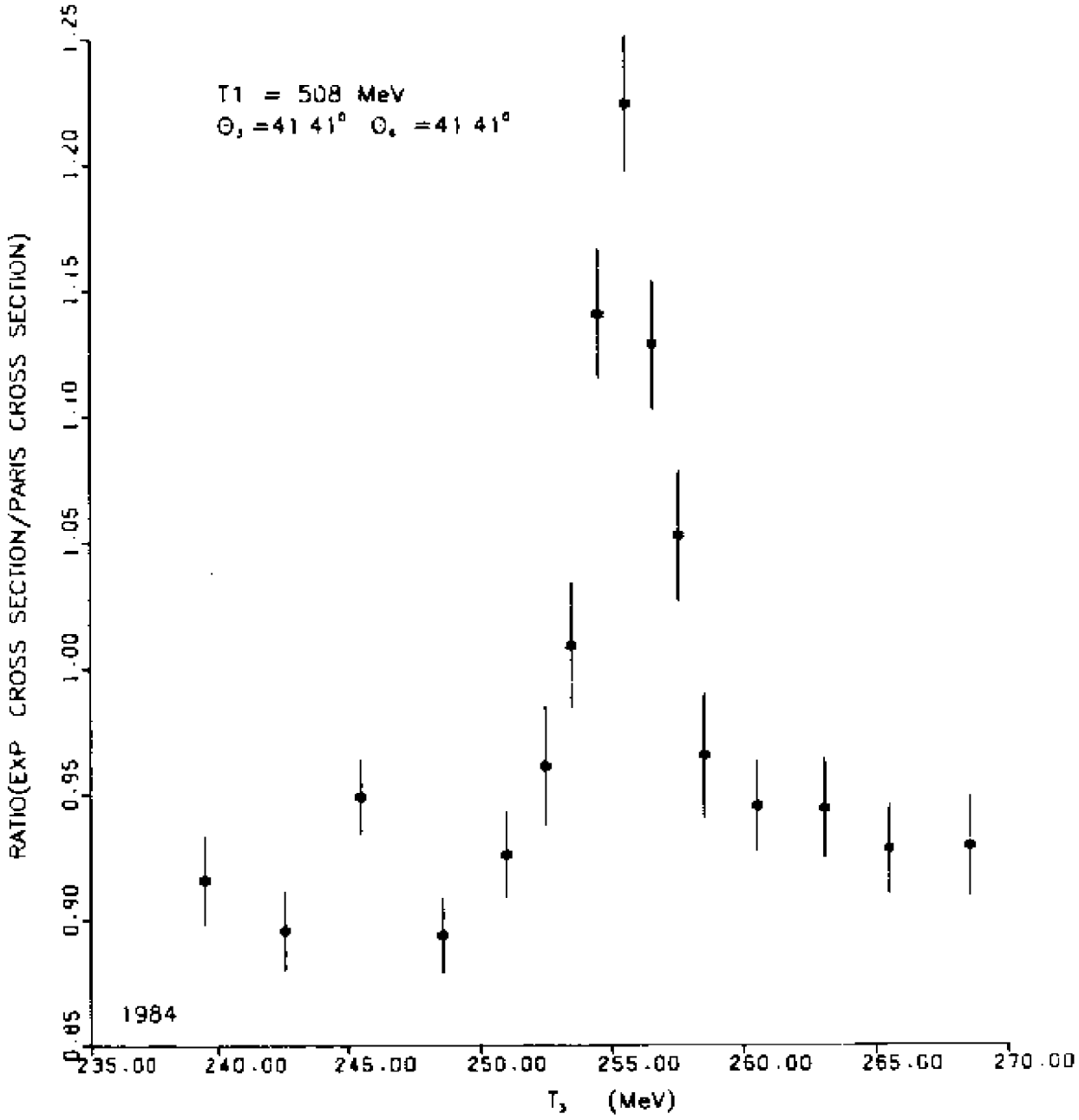
T1 = 508 MeV
Θ1 =41 41° Θ2 =41 41°
RATIO(EXP CROSS SECTION/PARIS CROSS SECTION)
0.85
0.90
0.95
1.00
1.05
1.10
1.15
1.20
1.25
1984
235.00
240.00
245.00
250.00
255.00
260.00
265.00
270.00
T1 (MeV)

FIGURE 5.4

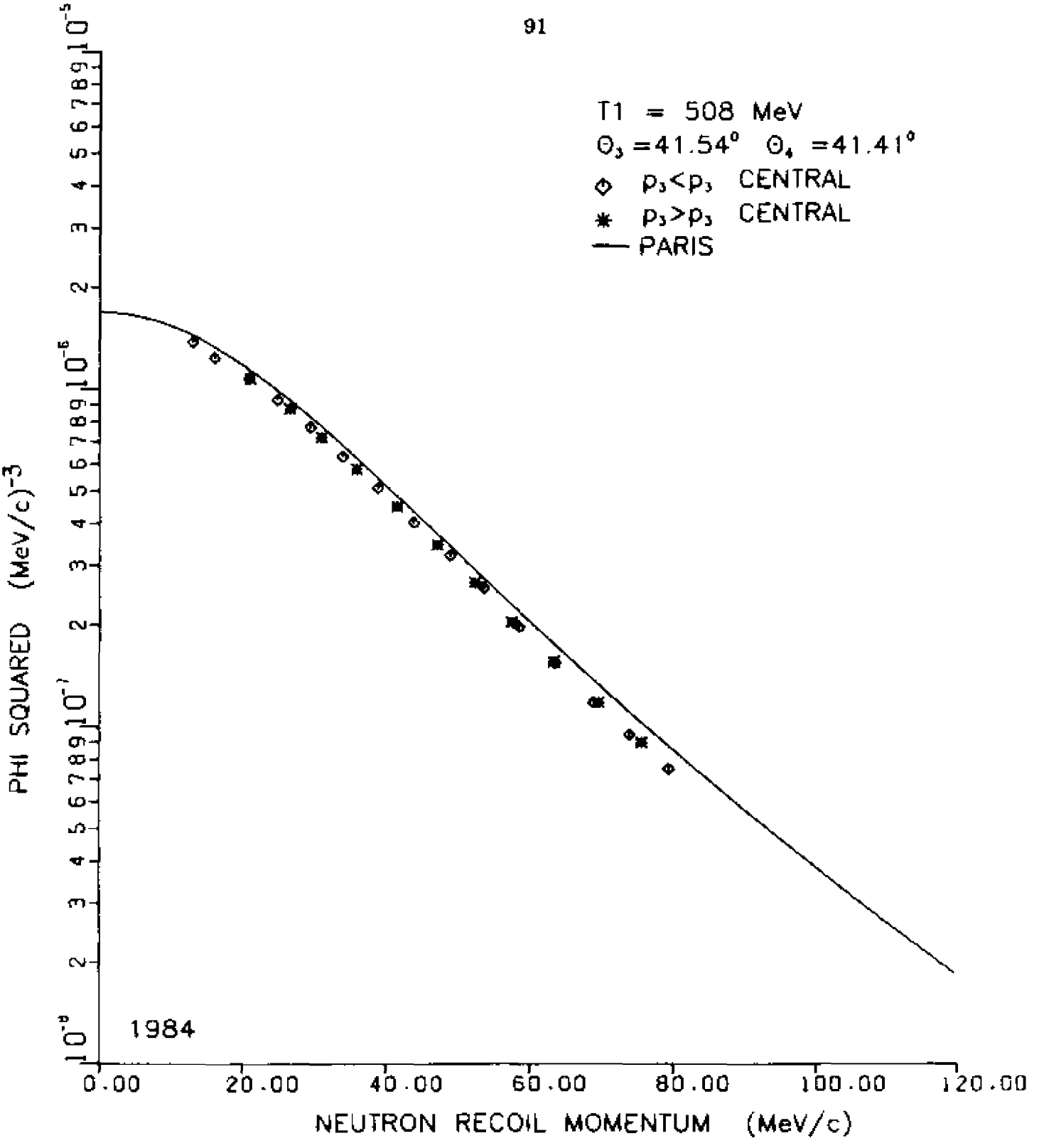
T1 = 508 MeV
Θ3 =41.54° Θ4 =41.41°
◇ p3<p3 CENTRAL
✱ p3>p3 CENTRAL
— PARIS
PHI SQUARED (MeV/c)-3
1984
0.00
20.00
40.00
60.00
80.00
100.00
120.00
NEUTRON RECOIL MOMENTUM (MeV/c)

FIGURE 5.5

and for the small solid angle Θ_3 = 41.36°. A misadjustment of the two solid angle defining counters ΔE_{B0} and ΔE_{B1} of 0.1° is directly seen in the display of the $(X_0 - Y_0)$ position detector. The uncertainty of ±1 MeV in the energy of the beam translates into an angle uncertainty of ±0.07°. Thus the correction applied is within experimental uncertainty. The same correction was also used for all the other angles.

In fig. 5.6 we display the ratio R of the measured cross section to the IA cross section vs. neutron recoil momenta for the same data. The error bars are statistical only. The IA cross section is for the Paris wave function as shown in eqn. (4.22). The curve labelled as "6 graphs" is the result of the multiple scattering calculation, as described in chapter 4. The ratio R for this curve is calculated as shown in formula (4.23). The data are still below expectation when multiple scattering is taken into account.

The best way to estimate the discrepancy between data and theory is to compare values of the probability P of finding a proton between given limits of internal momentum. We define P to be

$$P = \int_{q_{min}}^{q_{max}} \phi^2(\vec{q})\, q^2\, dq \;, \quad q = |\vec{P}_5| \qquad (5.11)$$

For the data in fig. 5.6, with q_{min} = 16 and q_{max} = 56 MeV/c we find P = 0.298. The corresponding value for the Paris momentum density between the same limits of q is 0.322; so about (7.4 ±0.4)% of the proton momentum density is missing over this range of internal momentum. When the multiple scattering results are taken into account the missing

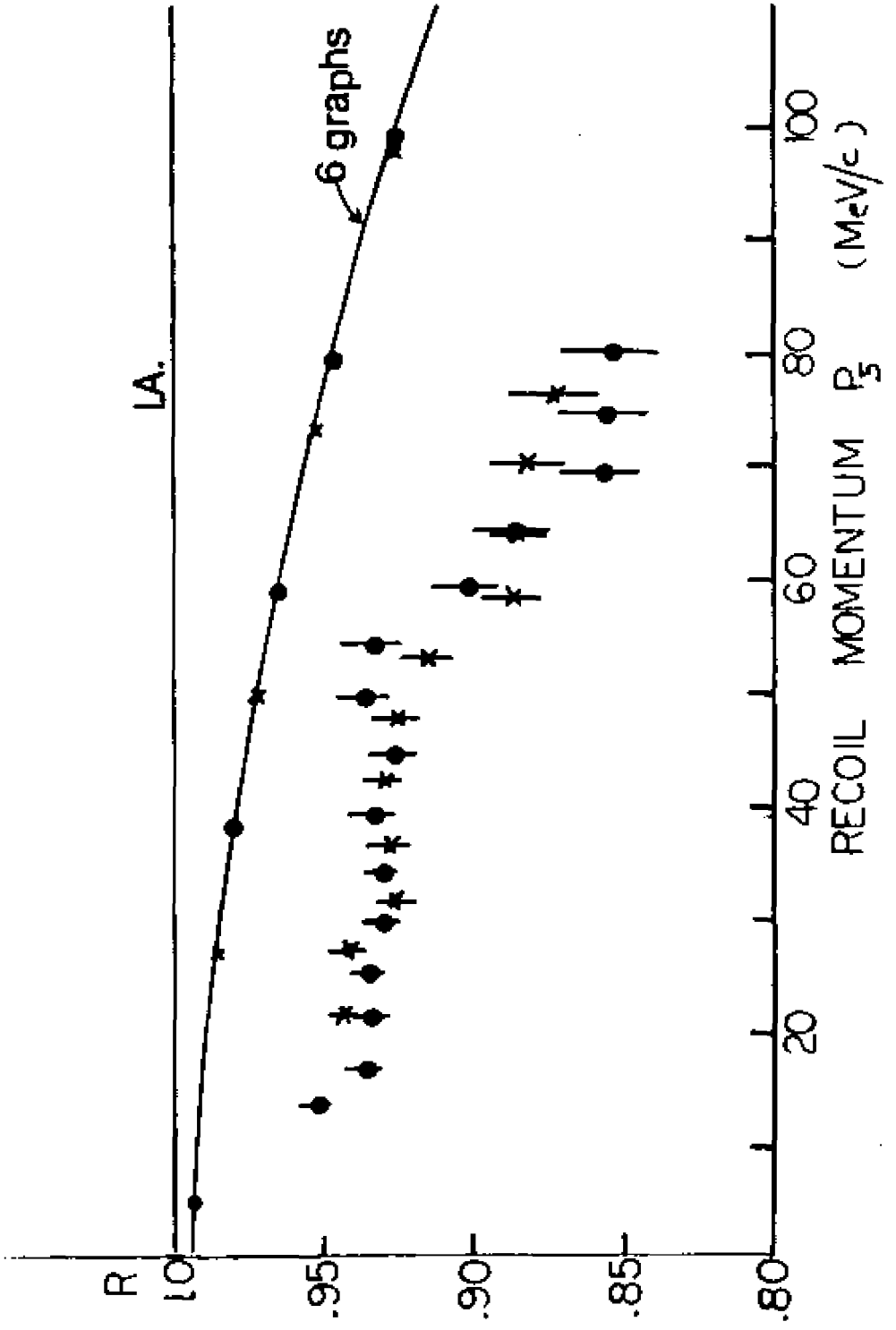
6 graphs
I.A.
R
1.0
.95
.90
.85
.80
20
40
60
80
100
RECOIL MOMENTUM P_5 (MeV/c)

FIGURE 5.6

strength is reduced to (5.7 ±0.4)%. The error quoted is statistical only. The systematic error on P is mostly due to uncertainty in p_5 and we estimate it to be ±1.9%. The systematic uncertainty on Φ^2in fig. 5.4 and R in fig. 5.6 is ±1.8%, again mostly due to the uncertainty in p_5.

The data shown in fig. 5.7 as R vs. p_5 are a subset of the data in fig. 5.3 through 5.5. These data are for solid angle $\Delta\Omega_3$ = 0.107 msr and $\Delta\Omega_4$ = 1.19 msr; $\Delta\Omega_3$ is defined by counter E_{B0} on the MRS side. (see section 2.5). The ratio R for these data and the multiple scattering curve are calculated as explained above. The error bars are statistical only. The data are low by 2.0% to 6.9%, compared to the Paris wave function and by 0.3% to 5.6%, compared to the multiple scattering calculation. When the probability P is compared with the Paris wave function, the data are found to be low by (6.1 ±0.5)%; when compared with the multiple scattering calculation the data are low by (4.6 ±0.5)%. The systematic uncertainty is again 1.9%. Comparing the data in fig. 5.6 and fig. 5.7 indicates good agreement below p_5 ~ 60 MeV/c, but different behavior above 60 MeV/c. The difference may be due to non-linearity in the MRS momentum calibration which was not corrected for, or to MRS transmission inefficiencies. Both effects affect the data from the larger solid angle most.

We also have data in the same range of neutron recoil momenta, from a measurement of $d^5\sigma$ for the asymmetric angle pair 30°.1 - 53.75°; the solid angles were $\Delta\Omega_3$ = 0.528 msr and $\Delta\Omega_4$ = 0.792 msr. The data are plotted as Φ^2 vs. neutron recoil momenta p_5 in fig. 5.8. The error bars shown are statistical only. Again, the agreement with the shape of

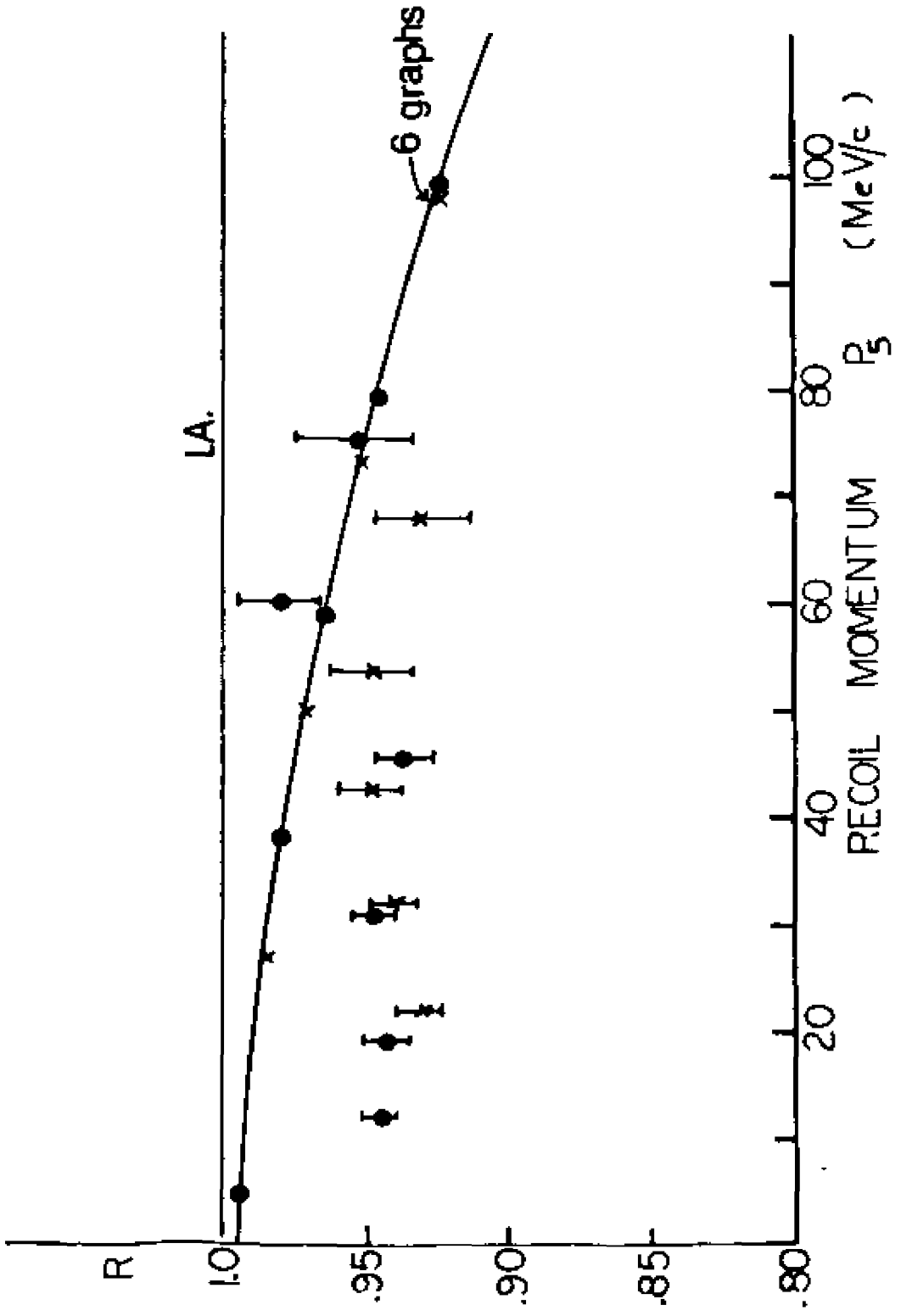
6 graphs
L.A.
R
1.0
.95
.90
.85
.80
20
40
60
80
100
RECOIL MOMENTUM P_5 (MeV/c)

FIGURE 5.7

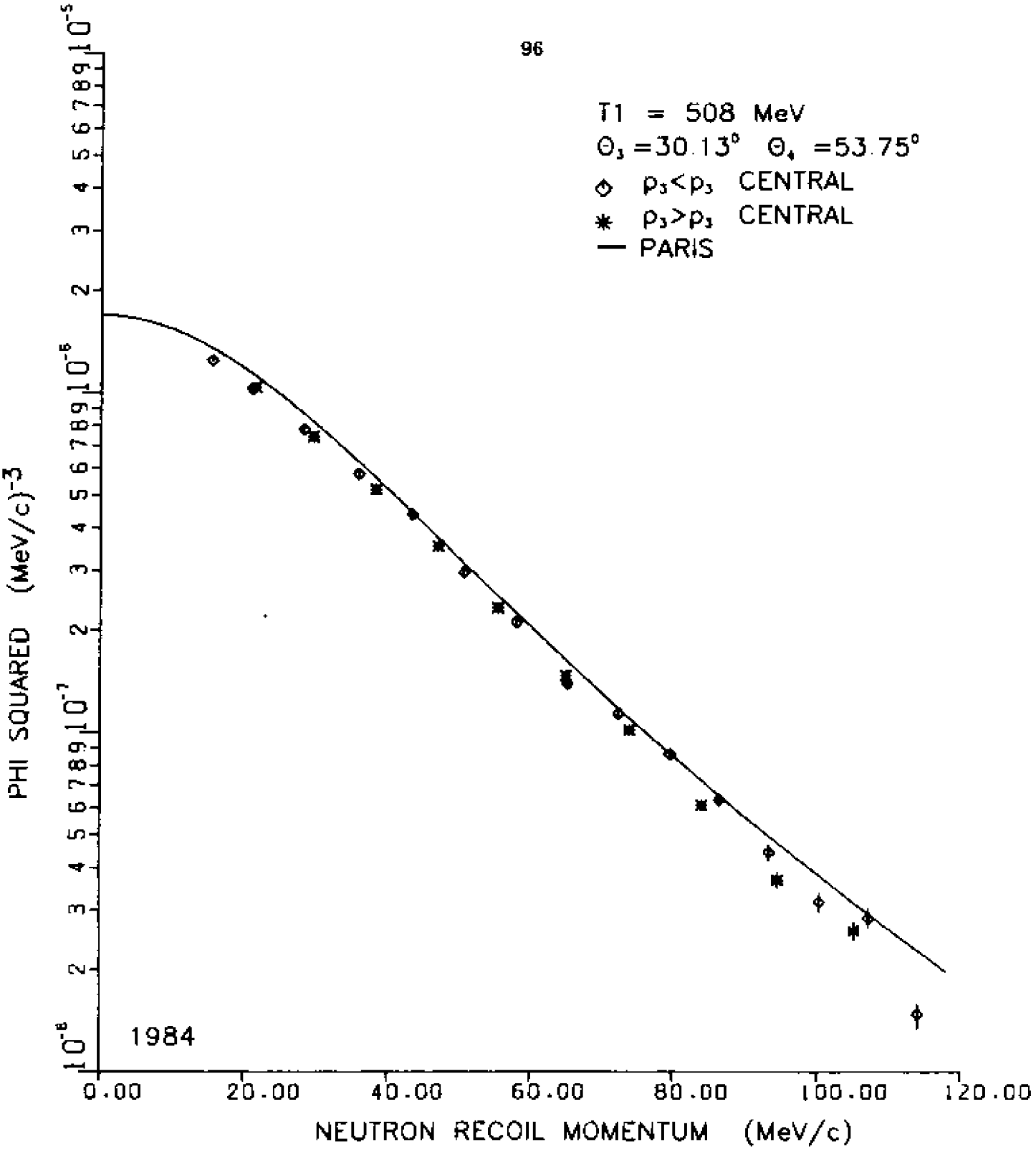
T1 = 508 MeV
Θ3 =30.13° Θ4 =53.75°
p3<p3 CENTRAL
p3>p3 CENTRAL
PARIS
PHI SQUARED (MeV/c)-3
NEUTRON RECOIL MOMENTUM (MeV/c)
1984
0.00
20.00
40.00
60.00
80.00
100.00
120.00

FIGURE 5.8

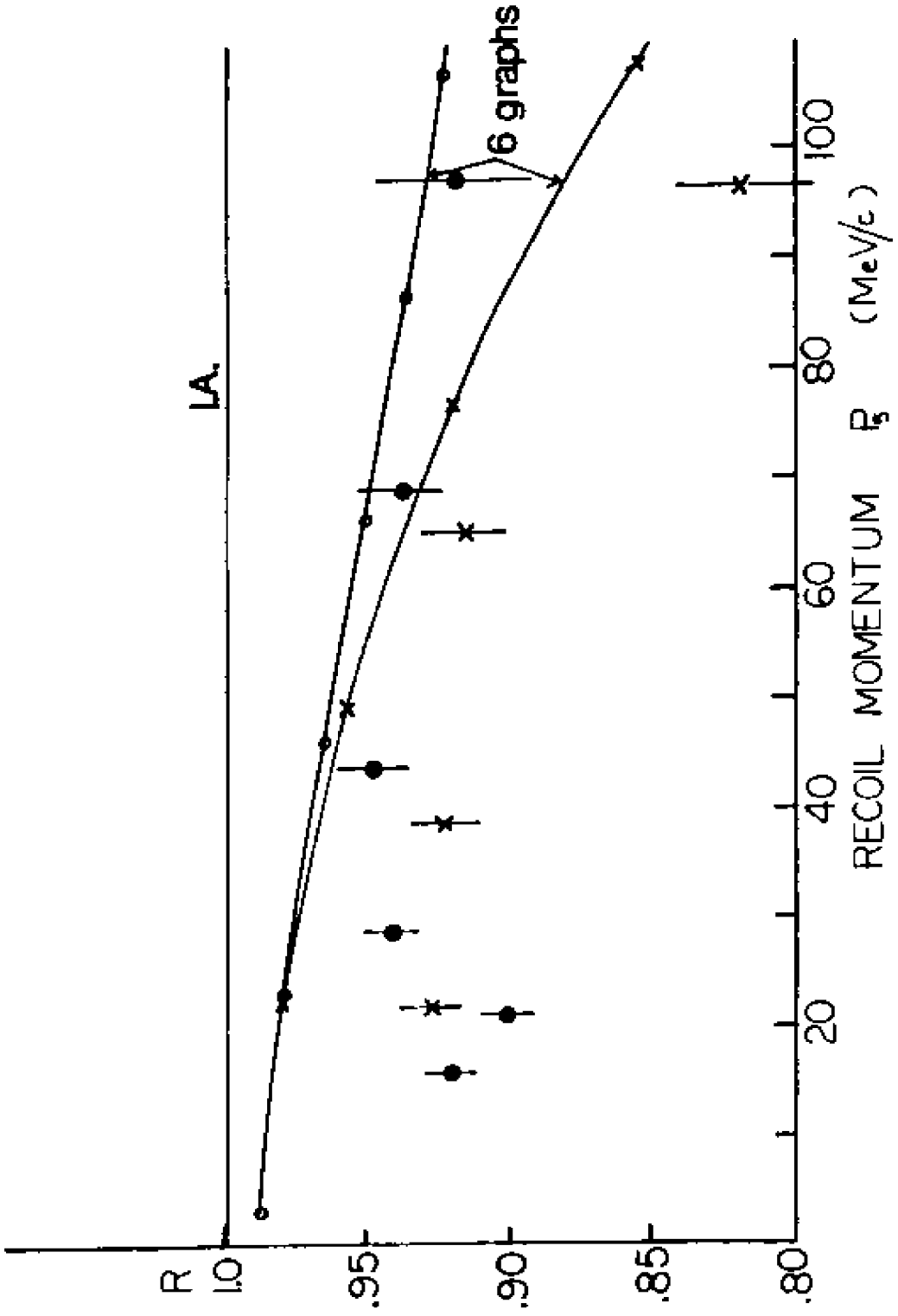
6 graphs
LA.
R
1.0
.95
.90
.85
.80
20
40
60
80
100
RECOIL MOMENTUM P_5 (MeV/c)

FIGURE 5.9

the theoretical momentum density is good, but the Φ^2 values are too small by 5% to 18%. We also display these data as R vs. the neutron recoil momenta in fig. 5.9. Notice the two branches (asymmetric kinematics) for the multiple scattering results. Comparing the data plotted by dots with the upper curve, and the crosses with the lower curve, the discrepancy with the data is 1% to 6%. These data are in good agreement with the data at the symmetric angle pair 41.4°. The P-value is low by (6.4 ±.5)%, when compared to the Paris wave function; the missing strength is reduced to (5.1 ±.5)% when P is compared with the multiple scattering result. Here the systematic uncertainty is 2.7%, larger than at 41.4° because the target thickness uncertainty does not cancel out (see sec. 3.6).

The two results from the 41.4° data are compatible with the 30.1° - 53.75° (see Table 5.1) result. The average of these three results gives a missing strength of 5.1% ±(0.7% standard deviation). This important result will be discussed further when we conclude.

Next, we discuss two other sets of small recoil momentum data. Fig. 5.10 shows the data for the 44.1° symmetric angle pair. Here the solid angles were $\Delta\Omega_3$ = 0.528 msr and $\Delta\Omega_4$ = 1.19 msr. Plotted in fig. 5.10 are Φ^2-values vs. p_5. When compared to the Paris Φ^2, the solid curve, we observe that the data are in excess of the IA by about 2% on the average. The multiple scattering correction is -1% to -3%. So when the data are compared with the multiple scattering results, they are found to be in excess by 3% on the average. The error bars shown are the statistical uncertainties only.

Table 5.1

Integrated probability P for n - recoils in range 16 to 56 MeV/c

Proton Angles	P_{data}	P^{IA}_{Paris}	P - defect when compared to IA (%)	P - defect when compared to 6 graphs (%)
41°	0.298	0.322	7.4 ±0.3* (±1.9)**	5.7 ±0.3
41°****	0.334	0.353	6.1 ±0.5 (±1.9)	4.6 ±0.5
30°-53.8°	0.326	0.353	6.4 ±0.5 (±2.7)	5.1 ±0.5
average			6.6 ±0.7***	5.1 ±0.7

*statistical error only

**systematic uncertainty

***standard deviation

****smaller solid angle on MRS-side

The data shown in fig. 5.11 as Φ^2-values vs. p_5 are for the 38.1° symmetric angle pair. The solid angles were as in fig. 5.10. These data are low by (16.5 ±4.3)% (standard deviation) on average over the region of neutron recoil momenta of interest, when compared with the Paris Φ^2, the solid curve. Compared to the dashed curve, the multiple scattering result, the data are low by (13.2 ±4.6)% (standard deviation) on average. The obvious difference between this result and the 44°-result will be discussed in the following section.

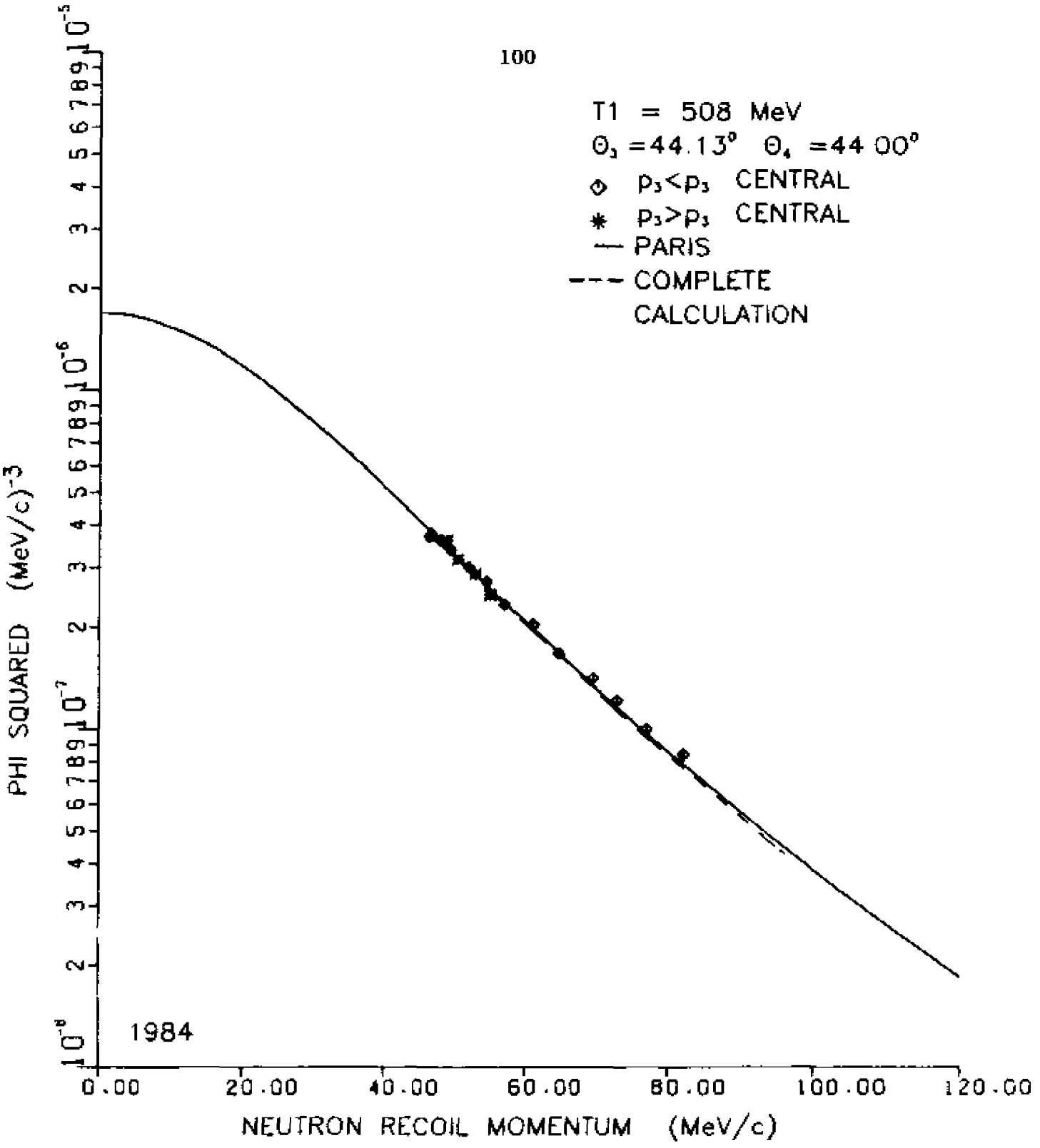
T1 = 508 MeV
Θ_3 = 44.13° Θ_4 = 44.00°
$p_3 < p_3$ CENTRAL
$p_3 > p_3$ CENTRAL
PARIS
COMPLETE CALCULATION
PHI SQUARED (MeV/c)$^{-3}$
10^{-5}
10^{-6}
10^{-7}
10^{-8}
1984
0.00
20.00
40.00
60.00
80.00
100.00
120.00
NEUTRON RECOIL MOMENTUM (MeV/c)

FIGURE 5.10

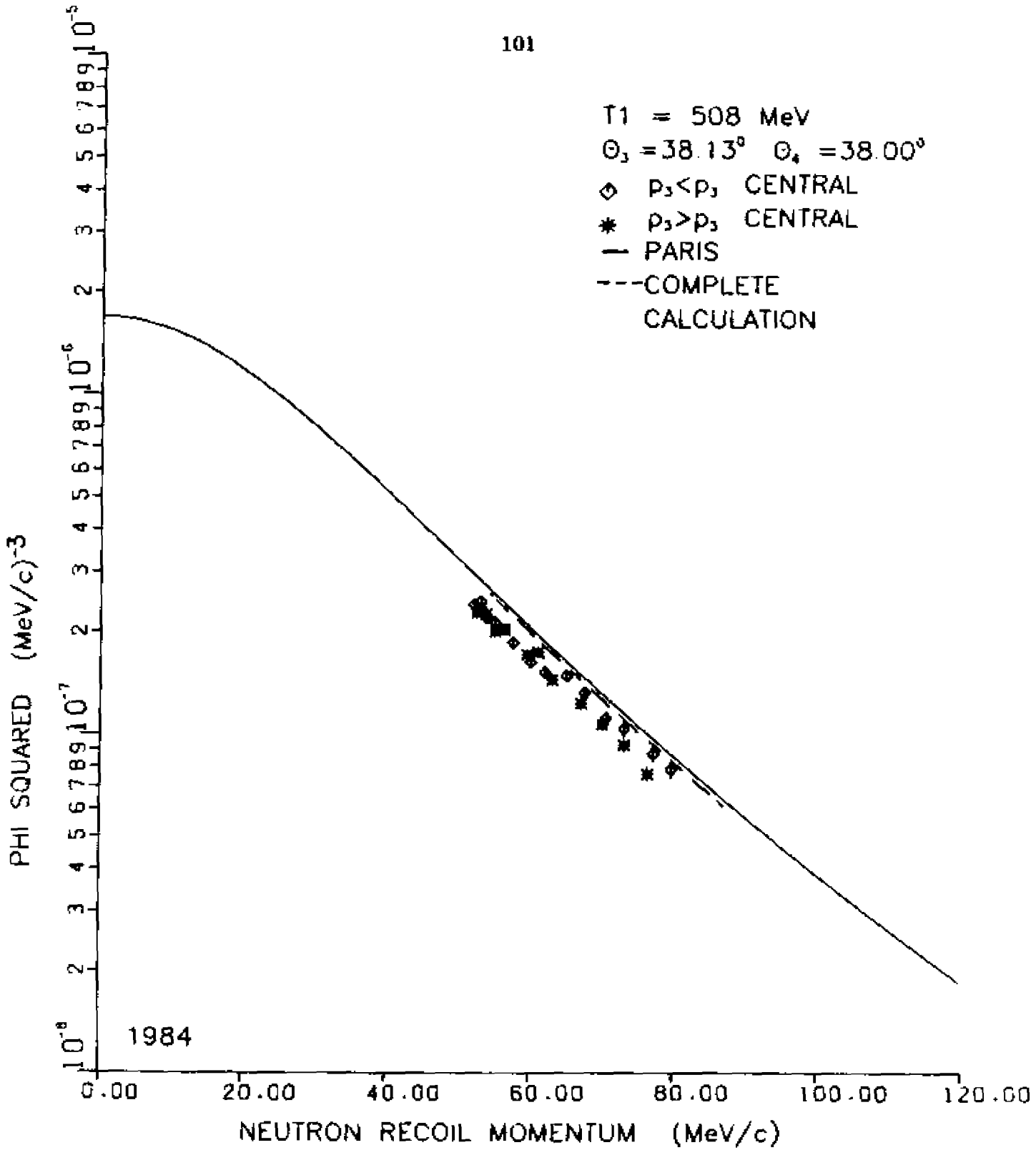
T1 = 508 MeV
Θ_3 = 38.13° Θ_4 = 38.00°
◇ $p_3 < p_3$ CENTRAL
✱ $p_3 > p_3$ CENTRAL
— PARIS
---COMPLETE CALCULATION
PHI SQUARED (MeV/c)$^{-3}$
10^{-5}
10^{-6}
10^{-7}
10^{-8}
1984
0.00
20.00
40.00
60.00
80.00
100.00
120.00
NEUTRON RECOIL MOMENTUM (MeV/c)

FIGURE 5.11

5.4 LARGE NEUTRON RECOIL AND ASYMMETRIC ANGLES DATA

In all previous (p, 2p) experiments it was observed that at neutron recoil momenta larger than 200 MeV/c, the cross section and momentum distribution stop decreasing with increasing recoil momentum. Our large neutron recoil data are in agreement with these results. The multiple scattering calculation does explain a large part of this enhancement for very large recoil momenta and another part is explained by the calculation of a non-IA graph which includes virtual excitation of the $\Delta(1232)$ resonance, as shown recently by Al Yano (Ya-85), and in the past by Wilkin (Cr-69, Al-77).

Fig. 5.12 shows the distribution of Φ^2-values as a function of neutron recoil momenta for symmetric angle pairs 47°, 50° and 52°. Comparing the data with the Paris Φ^2-distribution, the solid curve, we see that the 47° data are low by (7.3 ±6.0)% (standard deviation) on average in the neutron recoil range 106 to 140 MeV/c. When the multiple scattering correction is taken into account (the dashed curve), the data are low by (2.4 ±7.0)% (standard deviation) on average over the same recoil range. The data for 50° and 52° show two separate branches for $p_3 < \overline{p_3}$ (p_5 = minimum recoil) and $p_3 > \overline{p_3}$. We do not expect to see two branches for symmetric kinematics as discussed in section 5.2, and without a missing-mass cut, we find that the two branches agree rather well. It is interesting that both at 50° and 52°, the complete calculation including multiple scattering gives a cross section smaller than the IA value. However, the data show a different behavior; at 50° the Φ^2-values are indeed below the Φ^2_{Paris}, but at 52° they are above. The

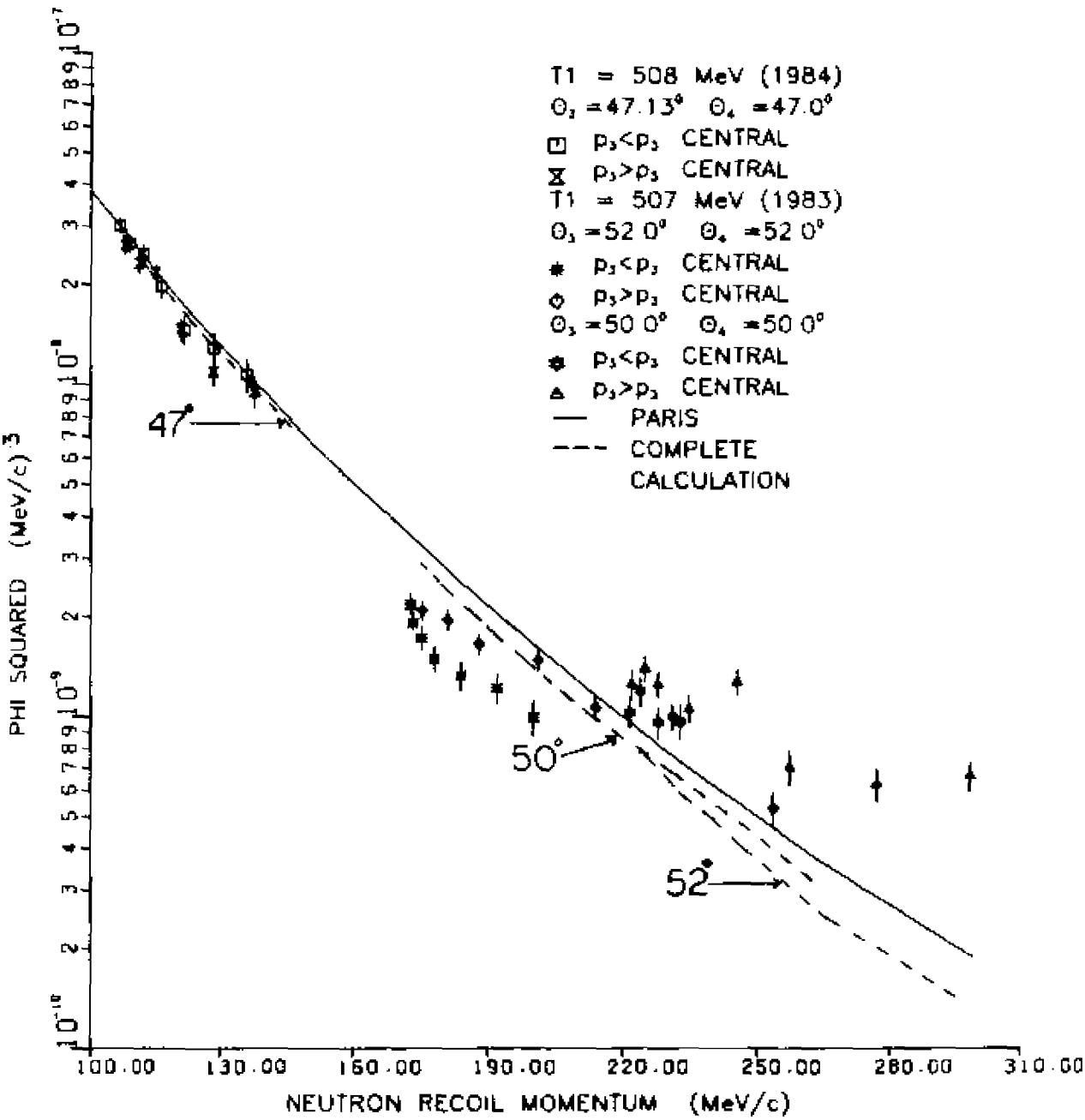
T1 = 508 MeV (1984)
Θ3 =47.13° Θ4 =47.0°
p3<p3 CENTRAL
p3>p3 CENTRAL
T1 = 507 MeV (1983)
Θ3 =52.0° Θ4 =52.0°
p3<p3 CENTRAL
p3>p3 CENTRAL
Θ3 =50.0° Θ4 =50.0°
p3<p3 CENTRAL
p3>p3 CENTRAL
PARIS
COMPLETE CALCULATION
47°
50°
52°
PHI SQUARED (MeV/c)^3
NEUTRON RECOIL MOMENTUM (MeV/c)
100.00
130.00
160.00
190.00
220.00
250.00
280.00
310.00

FIGURE 5.12

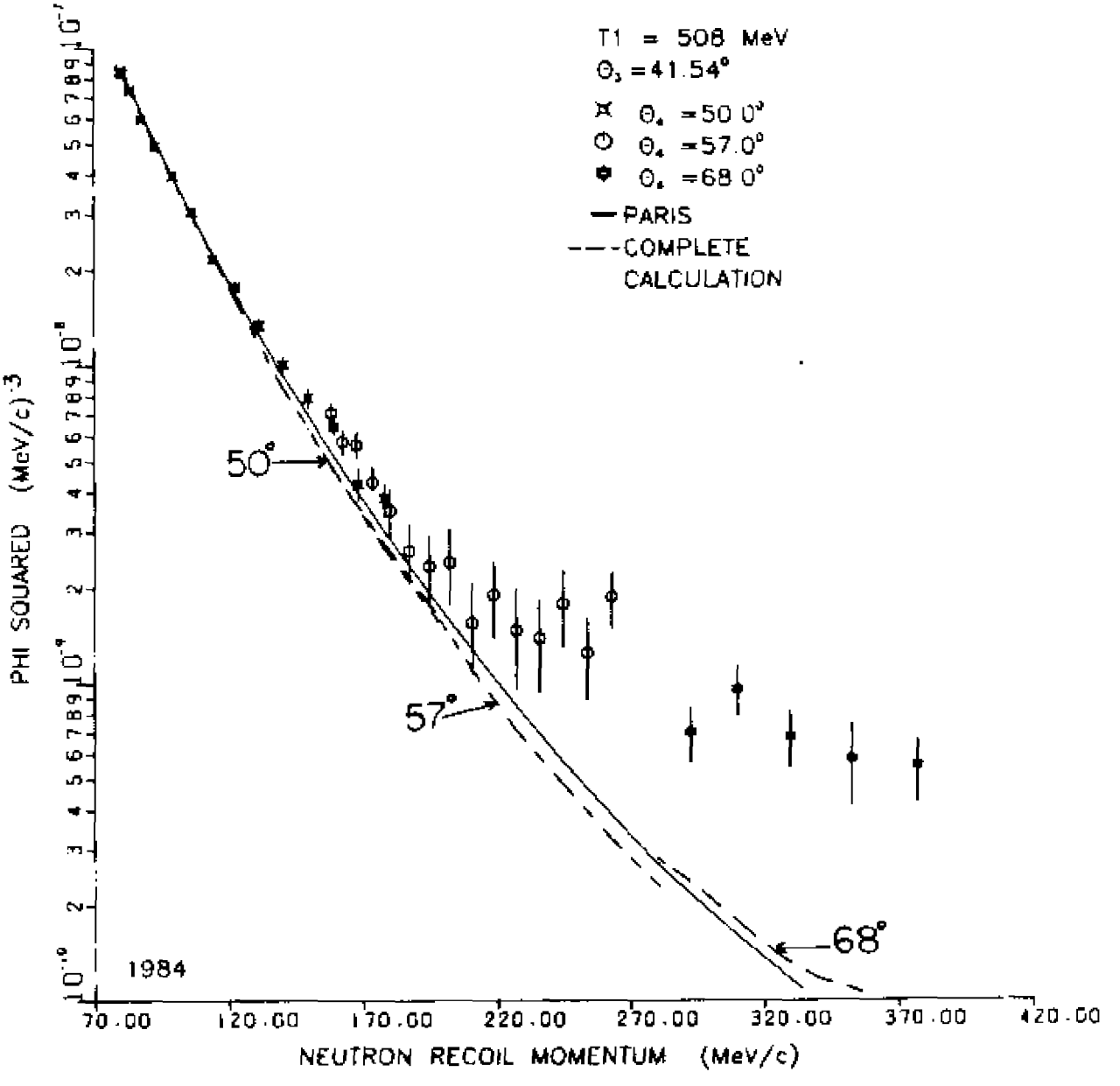
T1 = 508 MeV
$\Theta_3 = 41.54°$
$\Theta_4 = 50.0°$
$\Theta_4 = 57.0°$
$\Theta_4 = 68.0°$
PARIS
COMPLETE CALCULATION
50°
57°
68°
1984
PHI SQUARED (MeV/c)$^{-3}$
NEUTRON RECOIL MOMENTUM (MeV/c)
70.00
120.00
170.00
220.00
270.00
320.00
370.00
420.00

FIGURE 5.13

minimum recoil for 50° data is 174 MeV/c and for 52° data it is 222 MeV/c; so we do see that the data start deviating from the IA prediction starting at recoil momentum of about 200 MeV/c.

The data displayed in fig. 5.13 as Φ^2-values vs. p_5 are for the asymmetric angle pairs 41.54° - 50°, 41.50° - 57° and 51.54° - 68°. Here the solid curve represents the Φ^2_{Paris} distribution, and the dashed curve is from the multiple scattering calculation. We see that the data at small recoil start below the Φ^2_{Paris}, then cross over and remain in excess. For the angles 41.54° - 50° the correction due to multiple scattering is -1.8% to -11.3% for the recoil momenta of 78 to 180 MeV/c. For the angles 41.54° - 57° the correction for the recoil range 157 to 261 MeV/c varies from -7.6% to -16.0%. For the angles 41.54° - 68° the correction turns positive and ranges from +8.3% to +41%; the corresponding p_5 values are 287 to 383 MeV/c. The Φ^2 distribution obtained from the 3 angle pairs varies smoothly and continuously over the large recoil range covered, 78 to 383 MeV/c. Again, a distinct departure from the IA prediction can be seen, starting at about 200 MeV/c recoil momentum.

Next, fig. 5.14 shows the data for asymmetric angle pairs 30.14° - 44°, 30.14° - 61° and 30.14° - 68° in the form of the Φ^2 distribution as a function of p_5. Again the solid curve is Φ^2_{Paris} and the dashed line is from the multiple scattering calculation. The data for 30.14° -44° are as much as 19% below Φ^2_{Paris} at the minimum recoil of 66 MeV/c and then cross over and are in excess by as much as one and half times Φ^2_{Paris} at the recoil of 184 MeV/c. The data for 30.14° - 61°

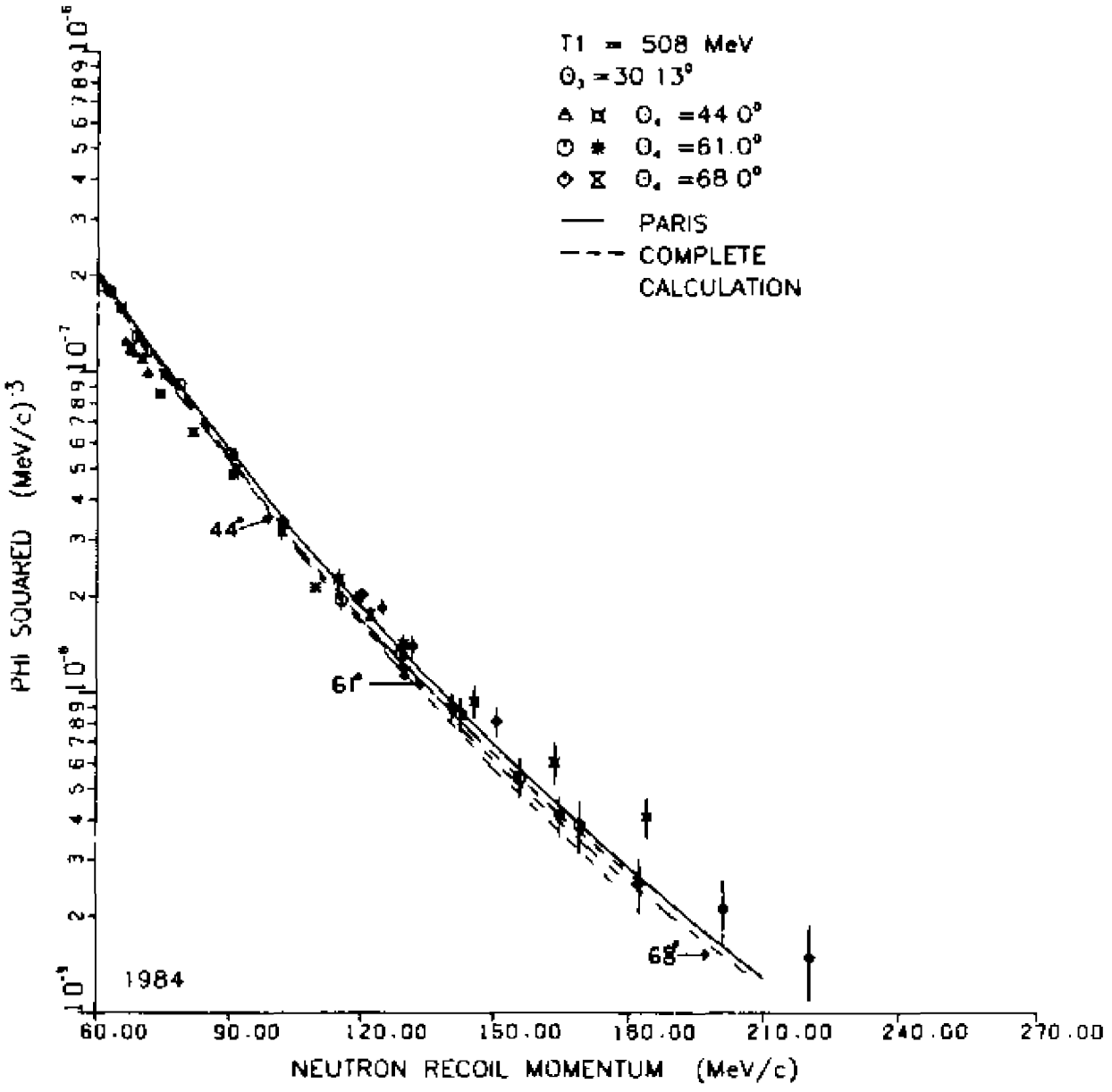
T1 = 508 MeV
θ, = 30 13°
θ, = 44 0°
θ, = 61.0°
θ, = 68 0°
PARIS
COMPLETE CALCULATION
PHI SQUARED (MeV/c)⁻³
NEUTRON RECOIL MOMENTUM (MeV/c)
60.00
90.00
120.00
150.00
180.00
210.00
240.00
270.00
44°
61°
68°
1984

FIGURE 5.14

agree well with Φ^2_{Paris} over the whole recoil range of 61 MeV/c to 169 MeV/c. The data for 30.14° - 68° also agree well with Φ^2_{Paris} except the last two data points. The multiple scattering values are below Φ^2_{Paris} for all three angle pairs and range from, -6.0% to -2.00% for 30.14° - 44°, -2.5% to -7.5% for 30.14° - 61° and -1.5 to -10% for 30.14° - 68°.

When the Φ^2 distributions obtained from these data are compared with the Φ^2 obtained from the data of other angles, we see that the Φ^2-values from 38° - 38° and 30.14° - 44° data agree where they overlap; the Φ^2-values obtained at 44° - 44°, 41.54° - 61° and 30.14° - 61° also agree where they overlap. This may not be fortuitous. The first set of angles is characterized by $\Theta_3 + \Theta_4 < 83.0°$ and second by $\Theta_3 + \Theta_4 > 83.0°$; or equivalently, the first set has $p_{5_{||}} < 0$ (i.e. anti-parallel to $\vec{p}_1$), the second $p_{5_{||}} > 0$ (i.e. parallel to $\vec{p}_1$). This behavior might be related to relativistic effects not included in the relativistic treatment of the kinematics. Several prescriptions to treat the problem of the off-shellness of the struck nucleon exist in the literature (for example Gugelot (Gu-84), Kobushkin (Ko-82), Bertocchi (Be-76)). All have in common that they lead to an internal momentum which is smaller than p_5 when $p_5 > 0$, and larger in absolute value than p_5 when $p_5 < 0$. Although we will not attempt here a detailed analysis of this sort, these relativistic effects will tend to bring the two sets of data mentioned in close agreement.

Fig. 5.15 shows the Φ^2 distribution for the 57° and 66° symmetric angle pairs. The error bars are for statistical uncertainty only. When the data are compared to Φ^2_{Paris}, the solid curve, the

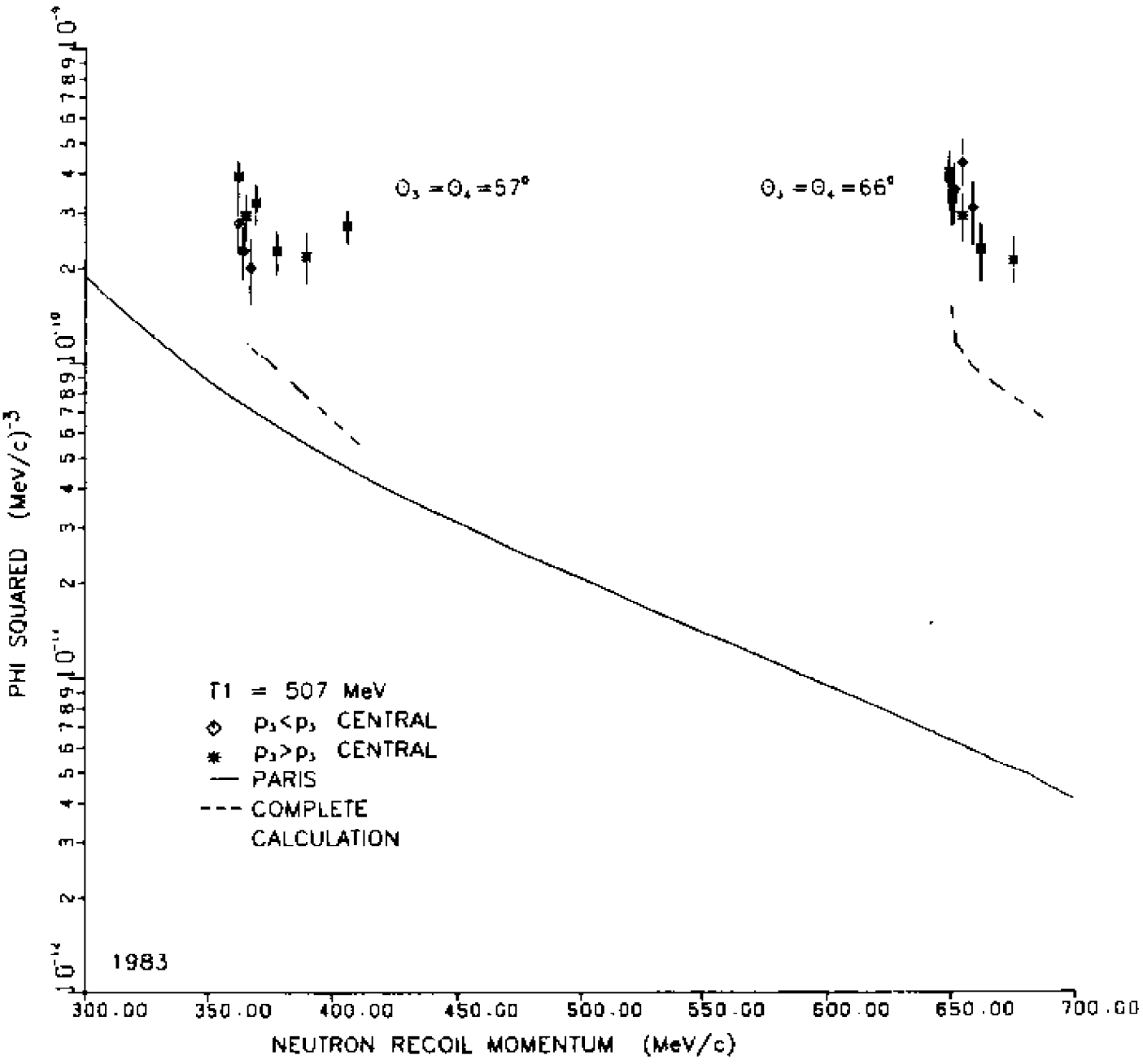
PHI SQUARED (MeV/c)$^{-3}$
$\Theta_3 = \Theta_4 = 57°$
$\Theta_3 = \Theta_4 = 66°$
T1 = 507 MeV
$p_3 < p_3$ CENTRAL
$p_3 > p_3$ CENTRAL
PARIS
COMPLETE CALCULATION
1983
300.00
350.00
400.00
450.00
500.00
550.00
600.00
650.00
700.00
NEUTRON RECOIL MOMENTUM (MeV/c)

FIGURE 5.15

discrepancy with the data is large for both angle pairs. The dashed curve, obtained from the multiple scattering calculation, does contribute the same fraction of the Φ^2-data at 57° and 66°. The Φ^2 values at 57° and at 41.54° - 68° agree well with each other in the overlapping region of recoil momenta.

Finally in fig. 5.16 we show the Φ^2-values at the minimum recoil momentum for all the symmetric angle pairs we measured. The data points for the angle pairs 41.54° - 41.41°, 38° and 50° are below the Φ^2_{Paris}, represented by the solid curve. The data at 44° and 47° angle pair are right on the curve and the data at 52°, 57° and 66° are systematically higher than Φ^2_{Paris}. The dashed curve represents the multiple scattering calculation results and the dashed-dotted curve labelled "Δ" is the calculation of the non-IA graph shown in fig. 5.16, which includes a pn^+n vertex and Δ-excitation through exchange of the pion, followed by de-excitation of the Δ through a second pion (or rho) exchange (Ya-85). The multiple scattering calculation by itself explains a large part of the data for large recoil momenta, and so does the result of the "Δ" calculation. It is possible that if we combined the amplitudes of these two processes, the result would agree with experiment. This is a difficult task which will not be attempted here.

5.5 COMPARISON WITH (e, e'p) AND PREVIOUS (p, 2p) DATA

Fig. 5.17 displays the data of the present experiment, the $^2H(e, e'p)n$ experiment of Bernheim et al (Be-81) and the $^2H(p, 2p)$ experiment of Witten et al. (Wi-75) as Φ^2 vs. p_5. The solid curve is

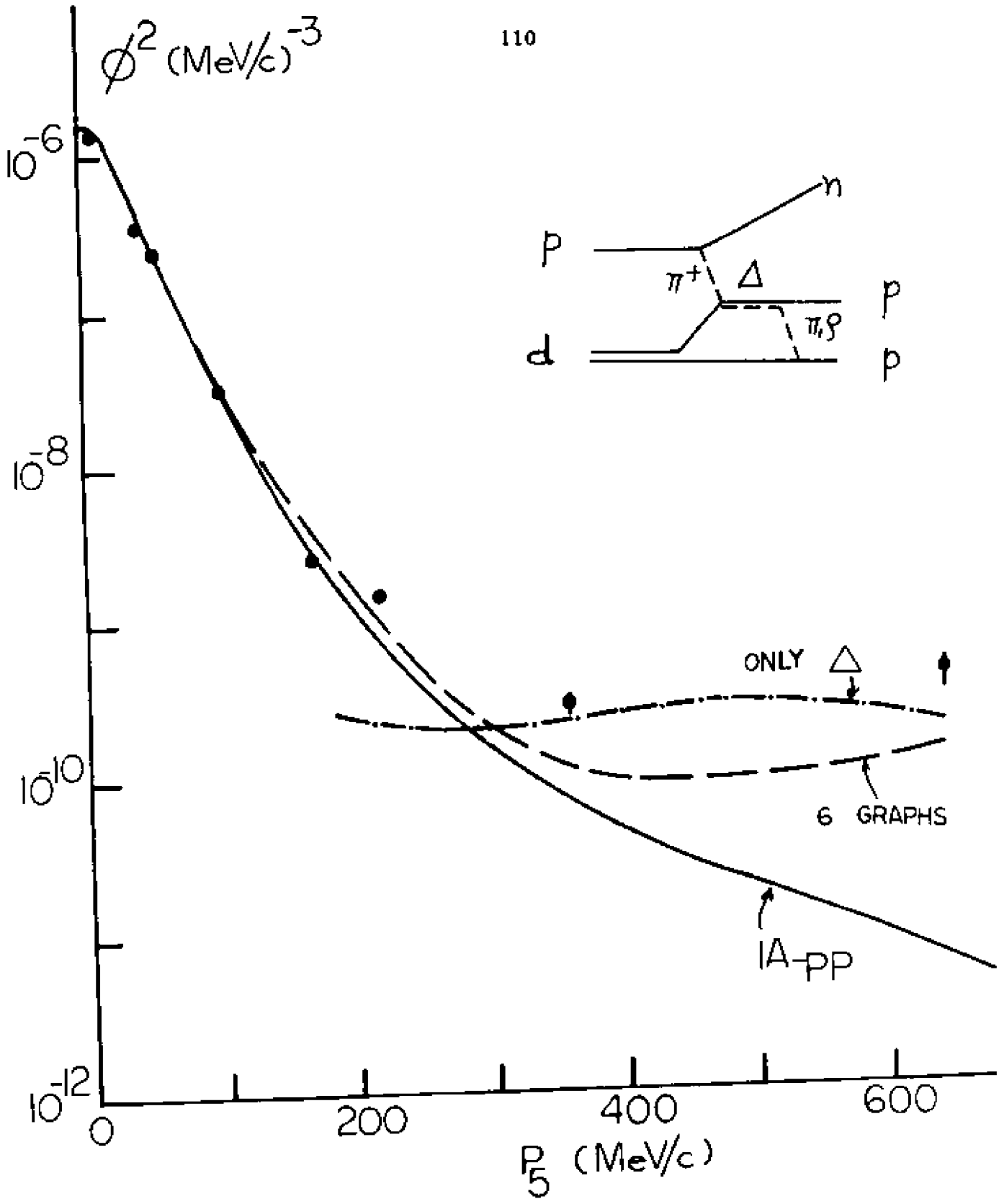
ϕ^2 (MeV/c)$^{-3}$
10^{-6}
10^{-8}
10^{-10}
10^{-12}
0
200
400
600
P_5 (MeV/c)
n
p
π^+
Δ
p
d
π, ρ
p
ONLY Δ
6 GRAPHS
IA-PP

FIGURE 5.16

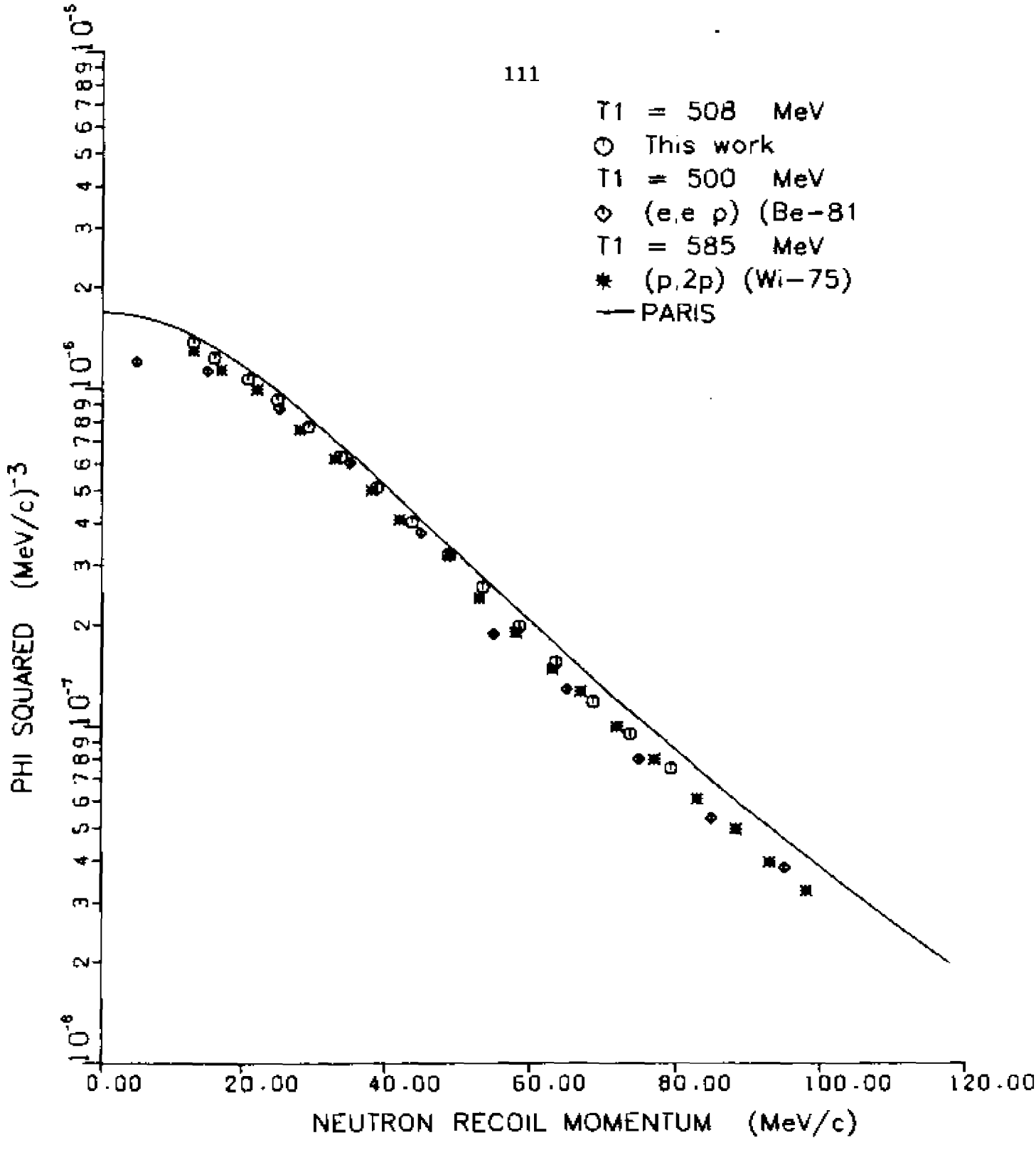
T1 = 508 MeV
This work
T1 = 500 MeV
(e,e p) (Be-81
T1 = 585 MeV
(p,2p) (Wi-75)
PARIS
PHI SQUARED (MeV/c)^-3
NEUTRON RECOIL MOMENTUM (MeV/c)
0.00
20.00
40.00
60.00
80.00
100.00
120.00

FIGURE 5.17

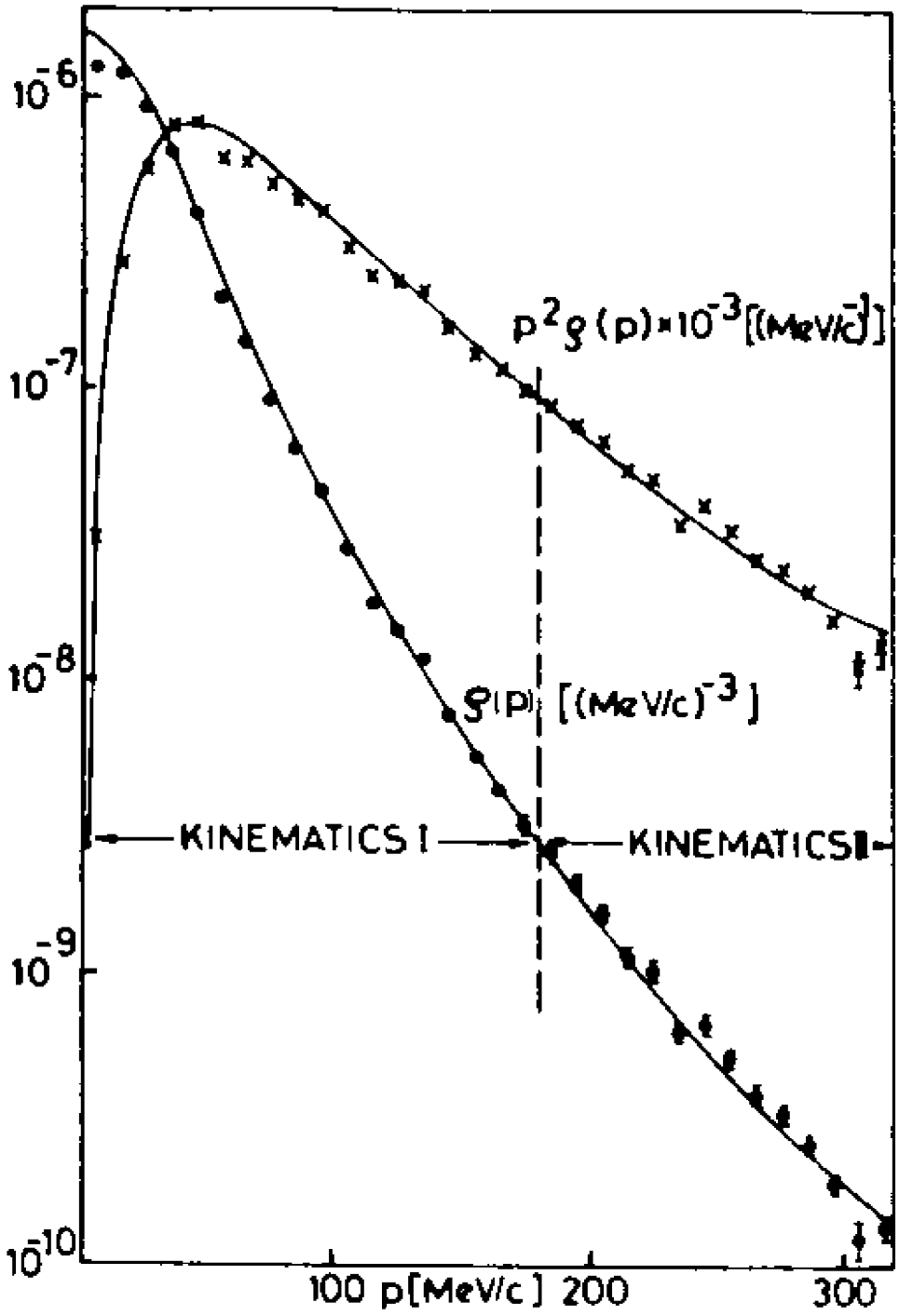
10^{-6}
10^{-7}
10^{-8}
10^{-9}
10^{-10}
$p^2 \varrho(p) \times 10^{-3}$ [(MeV/c)]
$\varrho(p)$ [(MeV/c)$^{-3}$]
KINEMATICS I
KINEMATICS II
100 p[MeV/c] 200
300

FIGURE 5.18

the Paris deuteron momentum density. The (e, e'p) data are systematically low by 18 to 20% compared to the Φ^2_{Paris}, for p_5 between 0 and 100 MeV/c, and are low by 10 to 12% when compared with our data. The same (e, e'p) data are shown in fig. 5.18 (fig. 7 from Ar-82) after several corrections such as final state interactions, meson exchange currents and isobar configurations are taken into account. Even after all the corrections mentioned above, the (e,e'p) data as seen in fig. 5.19 (which is fig. 5 in (Ar-82)) are low by a few percents in their "kinematics-I region," but one has to consider the systematic uncertainties before drawing any conclusions.

The (p, 2p) data of Witten et al. (Wi-75) at 585 MeV are typically 13% below the IA. Another (p, 2p) experiment at 800 MeV (Fe-78) also showed similar discrepancy when compared to the IA; the data are 11% too low (see Table 1.1). These two results must be compared with ours, which are 7% below the IA. The systematic uncertainties for the other (p, 2p) data is typically 10-15%, for our data it is 1.8%. Thus, our results are compatible within systematic errors with the old ones, but the reality of the missing strength is now confirmed at the 2% level.

The data for $p_5 > 100$ MeV/c are displayed in fig. 5.20 as Φ^2 vs p_5. Included here are the (e,e'p) data of Bernheim et al. (Be-81), which reach up to p_5 of 335 MeV/c and of Mehnert (Me-84) from 335 to 645 MeV/c, (p, 2p) data of Witten et al (Wi-75) up to p_5 of 420 MeV/c and our (p, 2p) data up to p_5 of 674 MeV/c. The very first thing we notice is that the (e, e'p) data more or less follow the IA curve all the way

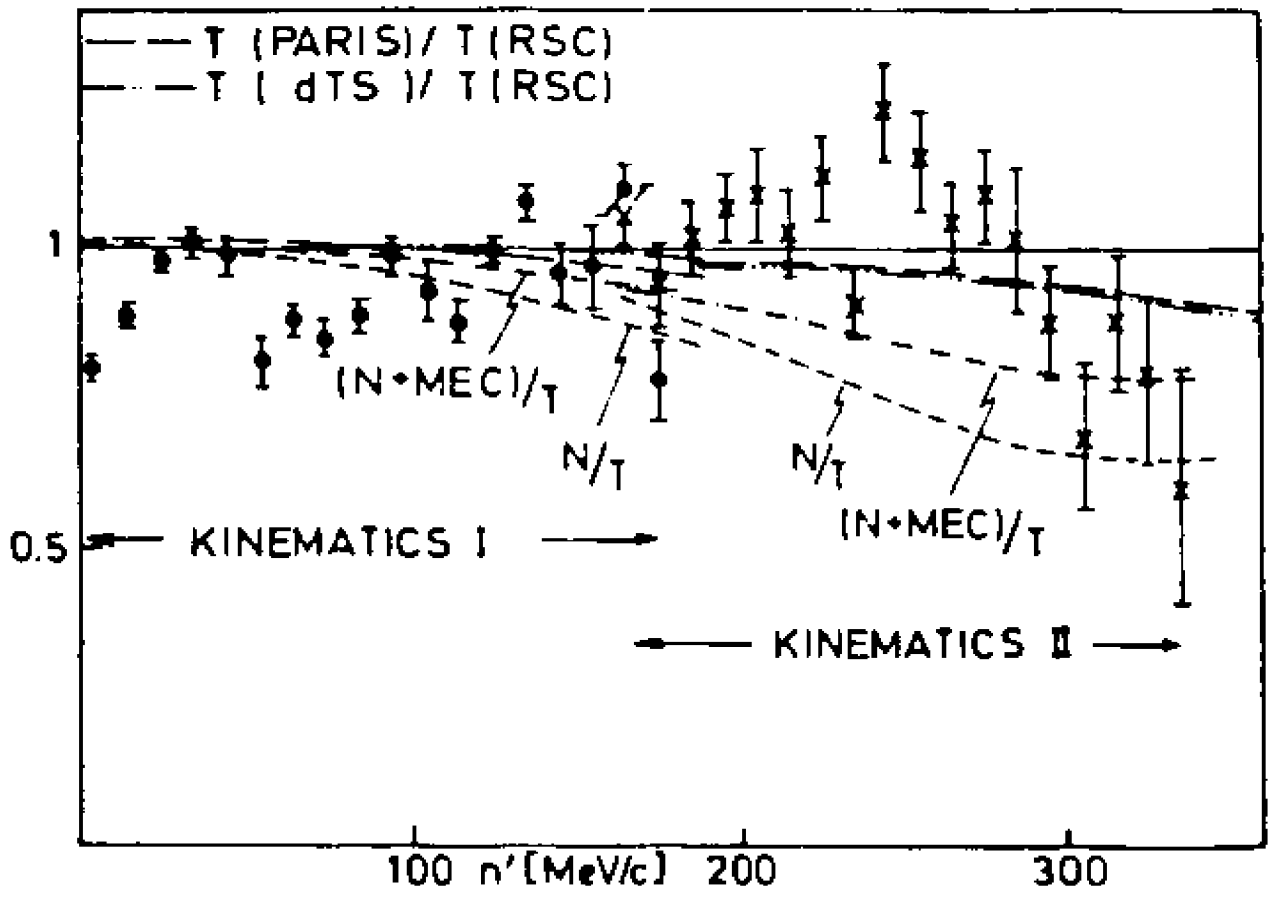
T (PARIS)/ T(RSC)
T (dTS)/ T(RSC)
1
0.5
(N+MEC)/T
N/T
N/T
(N+MEC)/T
KINEMATICS I
KINEMATICS II
100 n'(MeV/c) 200
300

FIGURE 5.19

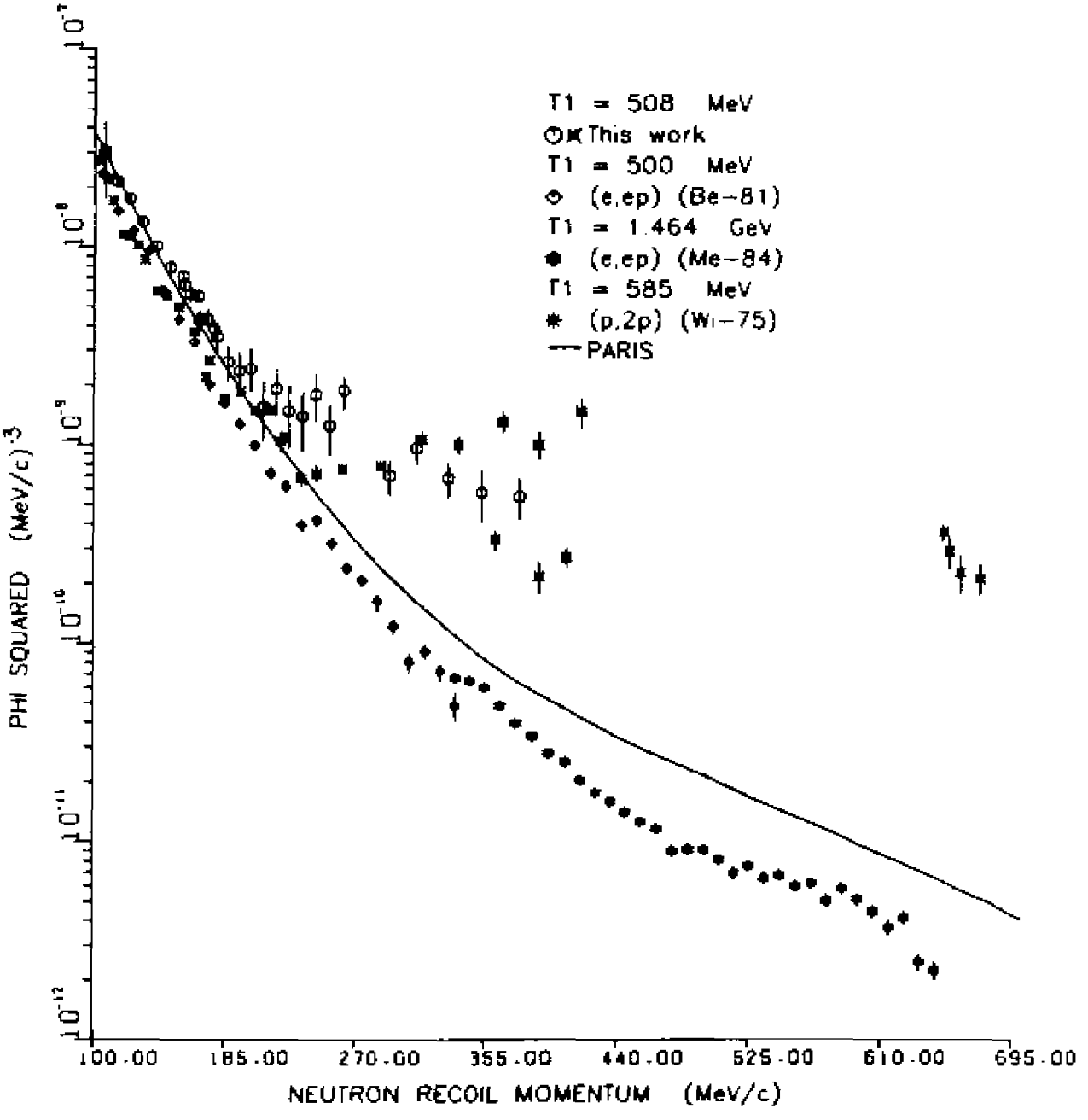
T1 = 508 MeV
This work
T1 = 500 MeV
(e,ep) (Be-81)
T1 = 1.464 Gev
(e,ep) (Me-84)
T1 = 585 MeV
(p,2p) (W-75)
PARIS
PHI SQUARED (MeV/c)-3
NEUTRON RECOIL MOMENTUM (MeV/c)
100.00
185.00
270.00
355.00
440.00
525.00
610.00
695.00

FIGURE 5.20

up to 645 MeV/c. They do not show any sudden departure from the IA prediction as the (p, 2p) data do starting at 200 MeV/c. The two (p, 2p) experiments are of a different nature; the data of Witten et al (Wi-75) were obtained keeping the angles fixed and changing the energy sharing among the two protons; the data of the present experiment were obtained changing the angles of the two protons symmetrically with respect to the incident beam direction. The data from both experiments show a distinct deviation from the IA prediction starting at about 200 MeV/c, suggesting that the IA no longer describe the (p, 2p) data in this recoil region. The asymmetric kinematic data, which reaches up to 380 MeV/c recoil show the same kind of behavior, also starting at 200 MeV/c (see fig. 5.13). The enhancement in Φ^2 starting at recoil momentum above 200 MeV/c had already been clearly seen in the (p, 2p) data at 600 MeV of Perdrisat et al (Pe-69). Similar behavior is also exhibited by the data of Felder et al (Fe-76), starting at the recoil of 200 MeV/c. It thus appears that in the energy range 500 to 800 MeV, the same abrupt deviation from the IA starts at the same neutron recoil momentum, 200 MeV/c.

CONCLUSIONS

The two results of this experiment will be discussed here.

First, as was shown in Chapter V, for n-recoil smaller than 100 MeV/c, the cross section data are lower than the IA prediction. The results are collected together in Table 5.1. The missing probability to find the proton in the deuteron is 6.6% relative to the IA, 5.1% when rescattering and final state interaction cross sections are included. (Systematic uncertainty are given in the Table.) So what are the possible causes for the missing strength in the small n-recoil range? Here we mention and discuss 3 possible origins for this missing strength.

(1) Referring to the multiple scattering expansion described in Chapter IV, both the single scattering and the double scattering terms are affected by the use of on-shell amplitudes instead of half-off-shell ones, although in different ways. Calculations of half-off-shell NN amplitudes have in the past been limited (Mo-69) to energies of 300 to 400 MeV by the difficulty of obtaining NN potential parameters above the pion production threshold. A calculation by the TRIUMF theory group (Fe-85), based on new Paris potential parameters, might soon be available. It is thus possible that the missing strength now well established for the $^{2}H(p, 2p)n$ reaction, will prove explainable when proper off-shell amplitudes are used in the evaluation of the theoretical cross section. It is, however, not possible at the present, to predict

whether this next step on the theoretical side will improve, or on the contrary make the agreement with the data worse.

(2) The data from this work have been compared with the Paris potential deuteron wave function, which contains 5.7% D-state. A deuteron wave function containing a larger D-state component, like the Reid soft-core (Re-68) potential with 6.47% D-state, will decrease the discrepancy between theory and data by 2%. Conversely, the Bonn potential which gives about 4.7% for the D-state probability, leads to a discrepancy larger by 4%. Although the results of this experiment are clearly sensitive to the D-state probability, it cannot be said that a better knowledge of the actual D-state probability has been gained. A more direct measurement of this important property of the deuteron might have to come from a determination of the momentum density in the region 200 - 600 MeV/c, where the D-state is dominant. The (p, 2p) data clearly indicate that this is a region where the pion degrees of freedom become important. It might be that in this region, non-nucleonic parts of the wave function become too important to allow an experimental determination of P_D. It is in fact questionable whether this quantity is actually accessible to an experimental determination (Fr-79).

As a conclusion, the present data could support a deuteron with a D-state probability somewhat larger than that of the Reid soft-core potential.

(3) The deuteron is expected to contain isobar components like $\Delta\Delta$, $NN^*(1520)$ NN^* (1688) and more (We-78), with a summed probability of 1 - 2%. The spin and parity of these isobars require an orbital

angular momentum for the NN*-states with L ≥ 1; even for the ΔΔ state which can have L = 0, L = 2 and 4 are more probable. All these states have momentum densities vanishing at q = 0, and as a consequence their presence tends to decrease the value of Φ^2 (p_5 = 0). No unambiguous experimental evidence for the reality of such components exists as of yet. Our results requires that the total isobaric component in the deuteron be at least 6%, which appears unlikely.

Finally, a 6-quark bag component has been postulated (Ko-82) to explain an anomaly in the deuteron breakup cross sections at 0° for 8.9 GeV/c deuterons by Ableev et al. (Ab-83). The parameters Ableev found necessary for this 6-quark component to explain the anomaly result in a decrease of Φ^2 (q = 0) by 4%. Although this number comes closest to the 6% observed in our experiment, much stronger evidence is required to rule out other possibilities.

To conclude, none of the above possibilities by itself, appears likely to explain the missing strength observed previously as well as in this experiment. But obviously, further calculations are required.

Second, it has been observed in all the previous (p, 2p) experiments as well as in the present one that for recoil momenta p_5 > 200 MeV/c, Φ^2 stops decreasing, suggesting breakdown of the IA so that Φ^2 is no longer a momentum distribution.

As best seen in fig. 5.16, the inclusion of the pn scattering term of the IA, and of rescattering and final state interaction improves the agreement (curve labelled "6 graphs") with our data in the region of

n-recoil larger than 200 MeV/c. In the same figure, it is also apparent that the Δ excitation mechanism calculated by Yano, by itself almost fits the data. Futhermore, relativistic effects connected to binding (see section 5.4) lead to values of the internal momenta smaller than p_5, and therefore explain some of the apparent excess in Φ^2 we observe.

Obviously, cross section measurements are insufficient to disentangle the several possible causes for the excess of Φ^2 in the large recoil region. It is possible that future polarization experiments (Wi-79), either with polarized protons, or vector- and tensor polarized deuterons, will bring the additional information needed for a complete understanding of the deuteron structure.

Appendix A

τ EXPANSION IN TERMS OF τ^i AND τ_i

From eqns. (4.4) and (4.5) we find the following operator equation:

$$\tau^i - \tau_i - \sum_{j\neq i} \tau_i G \tau^j = V_i + \sum_{j=1}^{3} V_i G \tau^j - V_i - V_i G \tau_i - \sum_{j\neq i} V_i G \tau^j - \sum_{j\neq i} V_i G \tau_i G \tau^j$$

$$= V_i G \left(\tau^i - \tau_i - \sum_{j\neq i} \tau_i G \tau^j \right)$$

Since $V_i G$ is not the identity operator, we must have

$$\tau^i = \tau_i + \sum_{j \neq i} \tau_i G \tau^j \qquad \text{(A2)}$$

Eqns. (A2) are the Faddeev equations. Equation (4.6) follows from above:

$$\tau = \sum_{i=1}^{3} \tau^i = \sum_{i=1}^{3} \left[\tau_i + \sum_{j \neq i} \tau_i G \tau^j \right]$$

$$= \tau_1 + \tau_2 + \tau_3 + \tau_1 G \tau^2 + \tau_1 G \tau^3)$$

$$+ \tau_2 G \tau^1 + \tau_2 G \tau^3 + \tau_3 G \tau^1 + \tau_3 G \tau^2$$

again using eqn. A2 gives:

$$\tau = \tau_1 + \tau_2 + \tau_3 + \tau_1 G \left[\tau_2 + \tau_2 G \tau^3 + \tau_2 G \tau^1 \right]$$

$$+ \tau_1 G \left[\tau_3 + \tau_3 G \tau^1 + \tau_3 G \tau^2 \right] + \tau_2 G \left[\tau_1 + \tau_1 G \tau^2 + \tau_1 G \tau^3 \right]$$

$$+ \tau_2 G \left[\tau_3 + \tau_3 G \tau^1 + \tau_3 G \tau^2 \right] + \tau_2 G \left[\tau_1 + \tau_1 G \tau^2 + \tau_1 G \tau^3 \right]$$

$$+ \tau_3 G \left[\tau_2 + \tau_2 G \tau^1 + \tau_2 G \tau^3 \right] \qquad \text{(A3)}$$

Equation (4.6a) follows from (A3) if one leaves terms with more than one G out, i.e. keeps only graphs with 2 interactions.

Appendix B

INTEGRAL d^2q AND KINEMATICS

Energy and momentum are conserved at both vertices for the rescattering and final state interaction diagrams. I show here how the momentum $|\vec{q}|$ was calculated at the second vertex from the energy and momentum conservation for diagram 4.2b.

$$\vec{P}_{35} = \vec{p}_3 + \vec{p}_5 \tag{B1}$$

$$E_{35} = E(\vec{p}3) + E(\vec{p}_5)$$

$$= E(\vec{p}_3 + \vec{p}_5 - \vec{q}) + E(\vec{q})$$

$$= \sqrt{(\vec{p}_3 + \vec{p}_5 - \vec{q})^2 + m^2} + \sqrt{q^2 + m^2} \tag{B2}$$

Taking the square of (B2) on both sides will give

$$E_{35}^2 = (\vec{P}_{35} - \vec{q})^2 + m^2 + q^2 + m^2 + 2\sqrt{m^2+(\vec{P}_{35} - \vec{q})^2} * \sqrt{q^2 + m^2} \tag{B3}$$

(B3) is a quadratic equation in q, and solving that equation will give

$$q = \frac{\left[P_{35}\cos\theta_q M_{35}^2 - E_{35}\sqrt{M_{35}^4 - 4m^2(E_{35}^2 - P_{35}^2\cos\theta_q)}\right]}{2(E_{35}^2 - P_{35}^2\cos^2\theta_q)} \tag{B4}$$

We see from (B4) that q is only dependent upon θ_q. Since the integral is two dimensional, we can transform d^2q to $d\theta_q$.

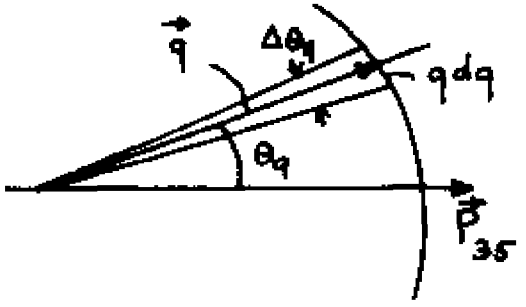

$$d^2q_\perp = 2\pi q \sin\theta_q \, q d\theta_q$$

$$= 2\pi q^2 \sin\theta_q \, d\theta_q .$$

Appendix C

THE NUCLEON-NUCLEON AMPLITUDES FOR THE THREE PARTICLE SPIN STATES

In this part I give the nucleon-nucleon amplitudes for all possible three-particle spin states. These amplitudes are taken from Jon Wallace's thesis (Wa - 71) and they are corrected for a few errors in sign.

$$\langle 1|F^{pN}|1\rangle = M^{pN}_{11}(\theta,\phi) = \langle 2|F^{pN}|2\rangle$$

$$\langle 1|F^{pN}|2\rangle = 0 = \langle 2|F^{pN}|1\rangle$$

$$\langle 1|F^{pN}|3\rangle = \sqrt{2/3}\, M^{pN}_{10}(\theta,\phi) = -\langle 2|F^{pN}|4\rangle e^{-2i\phi}$$

$$\langle 3|F^{pN}|1\rangle = \sqrt{2/3}\, M_{01}(\theta,\phi) = -\langle 4|F^{pN}|2\rangle e^{-2i\phi}$$

$$\langle 1|F^{pN}|4\rangle = \sqrt{1/3}\, M^{pN}_{1-1}(\theta,\phi) = \langle 2|F^{pN}|3\rangle e^{-4i\phi}$$

$$= \langle 4|F^{pN}|1\rangle e^{-4i\phi}$$

$$= \langle 3|F^{pN}|2\rangle$$

$$\langle 3|F^{pN}|3\rangle = (2/3)\, M^{pN}_{00} + (1/3)\, M^{pN}_{11} = \langle 4|F^{pN}|4\rangle$$

$$\langle 3|F^{pN}|4\rangle = \sqrt{2}/3\; M^{pN}_{10} - \sqrt{2}/3\, M^{pN}_{01} e^{-2i\phi} = -\langle 4|F^{pN}|3\rangle e^{-2i\phi}$$

N = p , n

$$\langle 1|F^{PP}|5\rangle = \sqrt{1/3}\, M^{PP}_{10}(\theta,\phi) = -\langle 2|F^{PP}|6\rangle e^{-2i\phi}$$

$$\langle 5|F^{PP}|1\rangle = \sqrt{1/3}\, M^{PP}_{01}(\theta,\phi) = -\langle 6|F^{PP}|2\rangle e^{2i\phi}$$

$$\langle 1|F^{PP}|6\rangle = -\sqrt{2/3}\, M^{PP}_{1-1}(\theta,\phi) = \langle 2|F^{PP}|5\rangle e^{-4i\phi}$$
$$= \langle 6|F^{PP}|1\rangle e^{-4i\phi} = \langle 5|F^{PP}|2\rangle$$

$$\langle 3|F^{PP}|5\rangle = \sqrt{2}/3\left(M^{PP}_{00}(\theta,\phi) - M_{11}(\theta,\phi)\right) = \langle 4|F^{PP}|6\rangle$$
$$= \langle 5|F^{PP}|3\rangle = \langle 6|F^{PP}|4\rangle$$

$$\langle 3|F^{PP}|6\rangle = \tfrac{1}{3}\left(M^{PP}_{10}(\theta,\phi) + 2M^{PP}_{01}(\theta,\phi)e^{-2i\phi}\right) = -\langle 4|F^{PP}|5\rangle e^{-2i\phi}$$

$$\langle 6|F^{PP}|3\rangle = \tfrac{1}{3}\left(M^{PP}_{01}(\theta,\phi) + 2M^{PP}_{10}(\theta,\phi)e^{2i\phi}\right) = -\langle 5|F^{PP}|4\rangle e^{2i\phi}$$

$$\langle 5|F^{PP}|5\rangle = \tfrac{1}{3}M^{PP}_{00}(\theta,\phi) + \tfrac{2}{3}M^{PP}_{11}(\theta,\phi) = \langle 6|F^{PP}|6\rangle$$

$$\langle 5|F^{PP}|6\rangle = \frac{\sqrt{2}}{3}\left(M^{PP}_{01}(\theta,\phi)e^{-2i\phi} - M^{PP}_{10}(\theta,\phi)\right) = -\langle 6|F^{PP}|5\rangle e^{-2i\phi}$$

$$\langle 7|F^{PP}|7\rangle = M^{PP}_{55}(\theta,\phi) = \langle 8|F^{PP}|8\rangle$$

$$\langle 7|F^{PP}|8\rangle = 0 \qquad = \langle 8|F^{PP}|7\rangle$$

$$\left\langle \begin{matrix}4\\6\end{matrix}\middle|F^{PP}\middle|\begin{matrix}7\\8\end{matrix}\right\rangle = 0 \qquad = \left\langle \begin{matrix}7\\8\end{matrix}\middle|F^{PP}\middle|\begin{matrix}4\\6\end{matrix}\right\rangle$$

$$\langle 1|F^{pn}|5\rangle_4 = -\sqrt{\tfrac{1}{12}}\, M^{pn}_{10}(\theta,\phi) = -\langle 2|F^{pn}|6\rangle_4 e^{-2i\phi}$$

$$\langle 5|F^{pn}|1\rangle_4 = -\sqrt{\tfrac{1}{12}}\, M^{pn}_{01}(\theta,\phi) = -\langle 6|F^{pn}|2\rangle_4 e^{-2i\phi}$$

$$\langle 1|F^{pn}|6\rangle_4 = \sqrt{\tfrac{1}{6}}\, M^{pn}_{1-1}(\theta,\phi) = \langle 2|F^{pn}|5\rangle_4 e^{-4i\phi}$$
$$= \langle 6|F^{pn}|1\rangle_4 e^{-4i\phi} = \langle 5|F^{pn}|2\rangle_4$$

$$\langle 3|F^{pn}|5\rangle_4 = \sqrt{\tfrac{1}{18}}\left(M^{pn}_{11}(\theta,\phi) - M^{pn}_{00}(\theta,\phi)\right) = \langle 4|F^{pn}|6\rangle_4$$
$$= \langle 5|F^{pn}|3\rangle_4 = \langle 6|F^{pn}|4\rangle_4$$

$$\langle 3|F^{pn}|6\rangle_4 = -\tfrac{1}{6}\left(2M^{pn}_{01}(\theta,\phi)e^{-2i\phi} + M^{pn}_{10}(\theta,\phi)\right) = -\langle 4|F^{pn}|5\rangle_4 e^{-2i\phi}$$

$$\langle 6|F^{pn}|3\rangle_4 = -\tfrac{1}{6}\left(2M^{pn}_{10}(\theta,\phi)e^{2i\phi} + M^{pn}_{01}(\theta,\phi)\right) = -\langle 5|F^{pn}|4\rangle_4 e^{2i\phi}$$

$$\langle 5|F^{pn}|5\rangle_4 = \frac{1}{12}\left(M^{pn}_{oo}(\theta,\varphi) + 2M^{pn}_{11}(\theta,\varphi) + 9M^{pn}_{ss}(\theta,\varphi)\right) = \langle 6|F^{pn}|6\rangle_4$$

$$\langle 5|F^{pn}|6\rangle_4 = \frac{\sqrt{2}}{12}\left(M^{pn}_{o1}(\theta,\varphi)e^{-2i\varphi} - M^{pn}_{10}(\theta,\varphi)\right) = -\langle 6|F^{pn}|5\rangle_4 e^{-2i\varphi}$$

$$\langle 7|F^{pn}|7\rangle_4 = \frac{1}{4}\left(2M^{pn}_{11}(\theta,\varphi) + M^{pn}_{oo}(\theta,\varphi) + M^{pn}_{ss}(\theta,\varphi)\right) = \langle 8|F^{pn}|8\rangle_4$$

$$\langle 7|F^{pn}|8\rangle_4 = \frac{\sqrt{2}}{4}\left(M^{pn}_{o1}(\theta,\varphi)e^{-2i\varphi} - M^{pn}_{10}(\theta,\varphi)\right) = -\langle 8|F^{pn}|7\rangle_4 e^{-2i\varphi}$$

$$\langle 1|F^{pn}|7\rangle_4 = -\frac{1}{2}M^{pn}_{10}(\theta,\varphi) = -\langle 2|F^{pn}|8\rangle_4 e^{-2i\varphi}$$

$$\langle 7|F^{pn}|1\rangle_4 = -\frac{1}{2}M^{pn}_{o1}(\theta,\varphi) = -\langle 8|F^{pn}|2\rangle_4 e^{2i\varphi}$$

$$\langle 2|F^{pn}|7\rangle_4 = \sqrt{\frac{1}{2}}M^{pn}_{1,-1}(\theta,\varphi)e^{4i\varphi} = \langle 1|F^{pn}|8\rangle_4 e^{4i\varphi}$$

$$= \langle 7|F^{pn}|2\rangle_4 e^{4i\varphi} = \langle 8|F^{pn}|1\rangle_4$$

$$\langle 3|F^{pn}|7\rangle_4 = \sqrt{\frac{1}{6}}\left(M^{pn}_{11}(\theta,\varphi) - M^{pn}_{oo}(\theta,\varphi)\right) = \langle 4|F^{pn}|8\rangle_4$$

$$= \langle 7|F^{pn}|3\rangle_4 = \langle 8|F^{pn}|4\rangle_4$$

$$\langle 4|F^{pn}|7\rangle_4 = \frac{1}{2\sqrt{3}}\left(M^{pn}_{10}(\theta,\varphi)e^{2i\varphi} + 2M^{pn}_{o1}(\theta,\varphi)\right) = -\langle 3|F^{pn}|8\rangle_4 e^{2i\varphi}$$

$$\langle 7|F^{pn}|4\rangle_4 = \frac{1}{2\sqrt{3}}\left(M^{pn}_{o1}(\theta,\varphi)e^{-2i\varphi} + 2M^{pn}_{10}(\theta,\varphi)\right) = -\langle 8|F^{pn}|3\rangle_4 e^{-2i\varphi}$$

$$\langle 5|F^{pn}|7\rangle_4 = \frac{1}{4\sqrt{3}}\left(2M^{pn}_{11}(\theta,\varphi) + M^{pn}_{oo}(\theta,\varphi) - 3M^{pn}_{ss}(\theta,\varphi)\right) = \langle 6|F^{pn}|8\rangle_4$$

$$= \langle 7|F^{pn}|5\rangle_4 = \langle 8|F^{pn}|6\rangle_4$$

$$\langle 6|F^{pn}|7\rangle_4 = \frac{1}{2\sqrt{6}}\left(M^{pn}_{10}(\theta,\varphi)e^{2i\varphi} - M^{pn}_{o1}(\theta,\varphi)\right) = -\langle 5|F^{pn}|8\rangle_4 e^{2i\varphi}$$

$$\langle 7|F^{pn}|6\rangle_4 = \frac{1}{2\sqrt{6}}\left(M^{pn}_{o1}(\theta,\varphi)e^{-2i\varphi} - M^{pn}_{10}(\theta,\varphi)\right) = -\langle 8|F^{pn}|5\rangle_4 e^{-2i\varphi}$$

$$\left\langle \begin{matrix}1\\6\end{matrix}\middle|F^{pn}\middle|\begin{matrix}1\\6\end{matrix}\right\rangle_3 = \left\langle \begin{matrix}1\\6\end{matrix}\middle|F^{pn}\middle|\begin{matrix}1\\6\end{matrix}\right\rangle_4$$

$$\left\langle \begin{matrix}7\\8\end{matrix}\middle|F^{pn}\middle|\begin{matrix}7\\8\end{matrix}\right\rangle_3 = \left\langle \begin{matrix}7\\8\end{matrix}\middle|F^{pn}\middle|\begin{matrix}7\\8\end{matrix}\right\rangle_4$$

$$\left\langle \begin{matrix}1\\6\end{matrix}\middle|F^{pn}\middle|\begin{matrix}7\\8\end{matrix}\right\rangle_3 = -\left\langle \begin{matrix}1\\6\end{matrix}\middle|F^{pn}\middle|\begin{matrix}7\\8\end{matrix}\right\rangle_4$$

$$\left\langle \begin{matrix}7\\8\end{matrix}\middle|F^{pn}\middle|\begin{matrix}1\\6\end{matrix}\right\rangle_3 = -\left\langle \begin{matrix}7\\8\end{matrix}\middle|F^{pn}\middle|\begin{matrix}1\\6\end{matrix}\right\rangle_4$$

The index $\langle\ \rangle_i$ refers to the non-interacting particle.

Appendix D

a, b, c, d COEFFICIENTS

This appendix contains the a, b, c, and d coefficients which appear in eqn. 4.18 to 4.21. These are also taken out of Jon Wallace's thesis and are also corrected for a few sign errors.

$$a_{\substack{L,1\alpha \\ L,-1\beta}}(\theta,\varphi,\theta',\varphi') = \sum_{L'} \langle L|F^{pp}(\theta,\varphi)|L'\rangle\langle L'|F^{pn}(\theta',\varphi')|\tfrac{1}{2}\rangle_4$$

$$a_{\substack{L,0\alpha \\ L,0\beta}}(\theta,\varphi,\theta',\varphi') = \sum_{L'}\Big[\langle L|F^{pp}(\theta,\varphi)|L'\rangle\langle L'|F^{pn}(\theta',\varphi')|\tfrac{3}{4}\rangle_4\tfrac{\sqrt{6}}{3} - \langle L|F^{pp}(\theta,\varphi)|L'\rangle\langle L'|F^{pn}(\theta',\varphi')|\tfrac{5}{6}\rangle_4\tfrac{\sqrt{3}}{6} + \langle L|F^{pp}(\theta,\varphi)|L'\rangle\langle L'|F^{pn}(\theta',\varphi')|\tfrac{7}{8}\rangle_4\tfrac{1}{2}\Big]$$

$$a_{\substack{L,-1\alpha \\ L,1\beta}}(\theta,\varphi,\theta',\varphi') = \sum_{L'}\Big[\langle L|F^{pp}(\theta,\varphi)|L'\rangle\langle L'|F^{pn}(\theta',\varphi')|\tfrac{4}{3}\rangle_4\tfrac{\sqrt{3}}{3} + \langle L|F^{pp}(\theta,\varphi)|L'\rangle\langle L'|F^{pn}(\theta',\varphi')|\tfrac{6}{5}\rangle\tfrac{\sqrt{6}}{6} - \langle L|F^{pp}(\theta,\varphi)|L'\rangle\langle L'|F^{pn}(\theta',\varphi')|\tfrac{8}{7}\rangle_4\tfrac{\sqrt{2}}{2}\Big]$$

$$b_{\substack{L,1\alpha \\ L,-1\beta}}(\theta,\varphi,\theta',\varphi') = \sum_{L'} \langle L|F^{pn}|L'\rangle_4\langle L'|F^{pp}|\tfrac{1}{2}\rangle$$

$$b_{\substack{L,0\alpha \\ L,0\beta}}(\theta,\varphi,\theta',\varphi') = \sum_{L'}\Big[\langle L|F^{pn}|L'\rangle_4\langle L'|F^{pp}|\tfrac{3}{4}\rangle\tfrac{\sqrt{6}}{3} - \langle L|F^{pn}|L'\rangle_4\langle L'|F^{pp}|\tfrac{5}{6}\rangle\tfrac{\sqrt{3}}{6} + \langle L|F^{pn}|L'\rangle_4\langle L'|F^{pp}|\tfrac{7}{8}\rangle\tfrac{1}{2}\Big]$$

$$b_{\substack{L,-1\alpha \\ L,1\beta}}(\theta,\varphi,\theta',\varphi') = \sum_{L'}\Big[\langle L|F^{pn}|L'\rangle_4\langle L'|F^{pp}|\tfrac{4}{3}\rangle\tfrac{\sqrt{3}}{3} + \langle L|F^{pn}|L'\rangle_4\langle L'|F^{pp}|\tfrac{6}{5}\rangle\tfrac{\sqrt{6}}{6} - \langle L|F^{pn}|L'\rangle_4\langle L'|F^{pp}|\tfrac{8}{7}\rangle\tfrac{\sqrt{2}}{2}\Big]$$

$$c_{L,1\alpha}(\theta\phi\theta'\phi') = \sum_{L'} \langle L|F^{pn}|L'\rangle_3 \langle L'|F^{pp}|\tfrac{1}{2}\rangle$$

$$c_{\substack{L,0\alpha\\L,0\beta}}(\theta\phi\theta'\phi') = \sum_{L'}\Big[\langle L|F^{pn}|L'\rangle_3\langle L'|F^{pp}|\tfrac{3}{4}\rangle\frac{\sqrt{2}}{3} - \langle L|F^{pn}|L'\rangle_3\langle L'|F^{pp}|\tfrac{5}{6}\rangle\frac{\sqrt{3}}{6} + \langle L|F^{pn}|L'\rangle_3\langle L'|F^{pp}|\tfrac{7}{8}\rangle\tfrac{1}{2}\Big]$$

$$c_{\substack{L,-1\alpha\\L,1\beta}}(\theta\phi\theta'\phi') = \sum_{L'}\Big[\langle L|F^{pn}|L'\rangle_3\langle L'|F^{pp}|\tfrac{4}{3}\rangle\frac{\sqrt{3}}{3} + \langle L|F^{pn}|L'\rangle_3\langle L'|F^{pp}|\tfrac{6}{5}\rangle\frac{\sqrt{2}}{6} - \langle L|F^{pn}|L'\rangle_3\langle L'|F^{pp}|\tfrac{8}{7}\rangle\frac{\sqrt{2}}{2}\Big]$$

$$d_{\substack{L,1\alpha\\L,-1\beta}}(\theta\phi\theta'\phi') = \sum_{L'}\langle L|F^{pn}|L'\rangle_3\langle L'|F^{pn}|\tfrac{1}{2}\rangle_4$$

$$d_{\substack{L,0\alpha\\L,0\beta}}(\theta\phi\theta'\phi') = \sum_{L'}\Big[\langle L|F^{pn}|L'\rangle_3\langle L'|F^{pn}|\tfrac{3}{4}\rangle_4\frac{\sqrt{2}}{3} - \langle L|F^{pn}|L'\rangle_3\langle L'|F^{pn}|\tfrac{5}{6}\rangle_4\frac{\sqrt{3}}{6} + \langle L|F^{pn}|L'\rangle_3\langle L'|F^{pn}|\tfrac{7}{8}\rangle_4\tfrac{1}{2}\Big]$$

$$d_{\substack{L,-1\alpha\\L,1\beta}}(\theta\phi\theta'\phi') = \sum_{L'}\Big[\langle L|F^{pn}|L'\rangle_3\langle L'|F^{pn}|\tfrac{4}{3}\rangle_4\frac{\sqrt{3}}{3} + \langle L|F^{pn}|L'\rangle_3\langle L'|F^{pn}|\tfrac{6}{5}\rangle_4\frac{\sqrt{2}}{6} - \langle L|F^{pn}|L'\rangle_3\langle L'|F^{pn}|\tfrac{8}{7}\rangle_4\frac{\sqrt{2}}{2}\Big]$$

REFERENCES

Ab - 83 V. G. Ableev et al., Nucl. Phys. A393 (1983) 491.

Al - 77 B.S. Aladashvili et al., J. Phys. G, Nucl. Phys., Vol 3, No. 9, (1977) 1225.

An - 85 K. A. Aniol et al., B.A.P.S. 30 (1985) 701.

Ar - 82 H. Arenhovel, Nucl. Phys. A384 (1982) 287.

Ar - 83 R. A. Arndt et al., Phys. Rev. D28 (1983) 97. Phase shifts obtained through a computer interactive dial in system (SAID) sp85 0-1 GeV.

Be - 76 L. Bertocchi, Nuovo Cimento 36A N1 (76) 1.

Be - 77 W. Bertozzi et al., Nucl. Instrum. Methods 141 (1977) 457.

Be - 81 M. Bernheim et al., Nucl. Phys. A365 (1981) 349.

Br - 84 A. Bracco et al., Nucl. Instrum. Methods 219 (1984) 329.

Ch - 52 G. F. Chew and G. C. Wick, Phys. Rev. 85, 636 (1952).

Ch - 82 P. Chatelain et al., J. Phys. G8 (1982) 643.

Cr - 69 N. S. Craigie and C. Wilkin, Nucl. Phys. B14 (1969) 477.

Ep - 84 M. B. Epstein et al., PANIC 84, Heidelberg Paper C2.

Fe - 76 R. D. Felder et al., Nucl. Phys. A264 (1976) 397.

Fe - 85 H. Fearing, Private communication. TRIUMF (1985).

Fr - 79 J. L. Friar, Phys. Rev C20 (1979) 325.

Fu - 73 M. Furic et al., Phys. LeH. 47B (1973) 241.

Gl - 59 R. J. Glauber, in Lecture in Theoretical Physics, ed. W. E. Brittin and L. G. Dunham (Inter Science Publishers, Inc., New York, 1959) Vol. I p. 315.

Go - 64 M. L. Goldberger and K. M. Watson, Collision Theory (John Wiley and sons, Inc., New York, 1964).

Go - 78 C. A. Goulding et al., Nucl. Instr. and Methods 148 (1978) 11.

Gu - 84 P. C. Gugelot, Phy Rev. C30, 654 (1984).

Ho - 84 H. G. Hoffmann, unpublished LAMPF Report (1984).

Ja - 66 G. Jacob and Th.A.J. Maris, Rev. Mod. Phys. 38, 121 (1966).

Ko - 82 A. P. Kobushkin and L. Vizireva, J. Phys. G8 (1982) 893.

La - 81 M. Lacombe et al., Phys. Lett. 101B (1981) 139.

Ma - 84 R. Machleidt, Lecture Notes in Physics, Vol 197 (Springer Verlag, Berlin, 1984) P. 352.

Me - 84 W. Mehnert, Ph.D. thesis, University of Bonn (1984) unpublished.

Mo - 60 T. R. Mongan, Phys. Rev. 180 (1969) 1514.

Ot - 84 D. Ottewell et al., Nucl. Phys. A412 (1984) 189.

Pe - 69 C. F. Perdrisat et al., Phys. Rev. 187, 1201 (1969).

Pe - 85 C. F. Perdrisat et al., Phys. Lett. B156, (1985) 38.

Pu - 84 V. Punjabi et al., B.A.P.S. 29, (1984) 646.

Pu - 85 V. Punjabi et al., B.A.P.S. 30, (1985) 795.

Pu - 85A V. Punjabi et al., B.A.P.S. 30, (1985) 1247.

Re - 68 R. V. Reid, Ann. of Phys. 50 (1968) 411.

Se - 84 H. J. Sebel, Report, Techn. Univ., Delft, unpublished.

St - 57 H. P. Stapp et al., Phys. Rev. 105, 302 (1957).

St - 81 A. W. Stetz, TRIUMF Design Note, TRI-DN-81-8, Sept. 81.

Ti - 84 J. Tinsley and J. Rogers, TRIUMF Design Note, TRI-DN-84-29, May 1984.

Tu - 84 S. Turck-Chieze et al., Phys. Lett. 142B (1984) 145.

Wa - 71 J. M. Wallace, Ph.D. thesis, Harvard University (1971), unpublished.

Wa - 72 J. M. Wallace, Phys. Rev. C5, (1972) 609.

We - 78 H. J. Weber and H. Arenhovel, Phys. Rep. 36C, (1978) 227.

Wi - 75 T. R. Witten et al., Nucl. Phys. A254 (1975) 269.

Wi - 79 C. Wilkin, Journees d'Etude SATURNE, Roscoff 1979, p. 47.

Wo - 68 D. Y. Wong, Three Particle Scattering in Quantum Mechanics, ed. J. Gillespie and J. Nuttall (W. A. Benjamin, Inc., New York, 1968) p. 297.

Wu - 48 T. Y. Wu and J. Ashkin, Phys. Rev. 73, 986 (1948).

Ya - 85 A. F. Yano, Phys. Lett. 156B (1985) 33.

FIGURE CAPTIONS

Fig. 1.1 Picturial Representation of the IA for the $^{2}H(p, 2p)n$ reaction.

Fig. 2.1 Layout of the proton beam line 4B at TRIUMF.

Fig. 2.2 Diagram of the liquid ^{2}H- and ^{1}H cryostat assembly.

Fig. 2.3 Layout of the experimental setup showing the scattering chamber, the six counter telescopes 1 to 6 on the RHS, and ΔE_{B0}, ΔE_{B1} and the MRS on the LHS.

Fig. 2.4 Diagram of the MRS showing the front end chambers (FEC), the quadrupole Q, dipole D, the vertical drift chambers (VDC's) and focal plane scintillators.

Fig. 2.5a Configuration of the 'U' and 'X' coordinates in the VDC's.

Fig. 2.5b Configuration of the vertical drift chambers showing the E-field in the drift regions and a typical particle trajectory.

Fig. 2.6 Simplified schematics for the medium resolution spectrometer (MRS) electronics.

Fig. 2.7 Schematic of the electronics used to generate the RHS trigger signal from 1 of the 6 RHS telescopes.

Fig. 2.8 Schematic of the electronics to detect a coincidence (L.R) between RHS trigger and either ΔE_{B1} or ΔE_{B0} on the LHS. The latch disables data acquisition until reset by "computer reset."

Fig. 3.1 One-dimensional histogram of the time-of-flight through the magnetic spectrometer from the ΔE_B counter to the focal plane scintillators. The arrows indicate the cuts to choose "proton" events and reject the "random" events. The number of events in the "proton" region has been divided by a factor of 200.

Fig. 3.2 One-dimensional histogram of the time-of-flight from the left (ΔE_B) to the right (ΔE_R) counters. The arrows indicate the cuts to separate "real"- and "random" events (separated by 43 ns). The number of events in the "reals" region has been divided by a factor of 50.

Fig. 3.3 Geometry in focal plane showing the focal plane XF, X_1 and X_2 coordinates and the constants F, G and H. Also shown are the angles Θ between particle trajectory and X_1 plane and δ between focal plane and VDC's. $\delta \approx 0$ in our case.

Fig. 3.4a The focal plane coordinate, XF (Channels) vs. P_3. Calibration of focal plane. (1983 data)

Fig. 3.4b Plot of NaI pulse height vs. T_4. Energy calibration for NAI crystal. (1983 data)

Fig. 3.5 Two-dimensional plot of the X_0 and Y_0 coordinates at the entrance of the MRS. Arrows shown are the cuts on the X_0 and Y_0 - coordinates to define the solid angle $\Delta\Omega_3$. (1983 data) Any wire hit is shown, regardless of frequency.

Fig. 3.6 Two-dimensional plot of the X_0-Y_0 coordinates at the drift chamber FEC. The solid angle $\Delta\Omega_3$ is defined by the plastic scintillator ΔE_{B1} of 3.5 cm. diameter. The projection of this counter is clearly seen. The FEC was located 40cm downstream from ΔE_{B1}.

Fig. 3.7 Plot of the X_0-Y_0 coordinates at the FEC chamber for the smaller solid angle defined by counter ΔE_{B0} of 1.7 cm diameter. The distance between ΔE_{B0} and the chamber was 29 cm.

Fig. 3.8 Two-dimensional energy spectrum for the two detected protons in $^2H(p, 2p)n$. The locus corresponds to quasi-free scattering.

Fig. 3.9 One dimensional spectrum of missing mass m_5. The arrows show the cut to select real events with a recoiling neutron and reject randoms.

Fig. 3.10 Same as 3.8 but including the missing mass cut.

Fig. 4.1a and 4.1b Impulse approximation diagrams for (a) pp scattering, and (b) pn scattering.

Fig. 4.2a Rescattering diagram: pn interaction followed by pp rescattering.

Fig. 4.2b Rescattering diagram: pp interaction followed by pn rescattering.

Fig. 4.2c Final state interaction diagram: pp interaction followed by pn interaction of the two target nucleons.

Fig. 4.2d Final state interaction diagram: pn interaction followed by pn interaction of the two target nucleons.

Fig. 4.3 Percentage correction (R-1) to IA for pp scattering, vs. recoil momentum p_5 for the 41.41° symmetric angle pair. ■□ corresponds to diagram 4.2a, ▲Δ to 4.2b, ▼∇ to 4.2c and ◆◇ to 4.2d. The solid curve is the global result including all six diagrams in figures 4.1 and 4.2. Filled symbols are for $p_3 < p_3$ ($p_5 = 0$).

Fig. 4.4 Percentage correction (R-1) for the symmetric angle pairs 38°, 44° and 47°. Only the global results are shown here. The dots are for $p_3 < p_3$ (minimum of p_5).

Fig. 4.5 Same as 4.3 for the asymmetric angle pair 30° - 53.75°. Only the global curve is shown. The dots correspond to $p_3 < p_3$ ($p_5 = 0$).

Fig. 4.6 The solid curve is the ratio R of the calculated cross section including all six diagrams to the IA (pp only) cross section at the minimum recoil for the symmetric angle pairs. The dashed curve is IA (pp + np) divided by IA (pp only).

Fig. 5.1 Schematic of kinematics: p_1 is beam momentum, p_3 and p_4 are the momenta of the detected protons; Θ_3 and Θ_4 are the angles between incident beam and the center of the detectors on LHS and RHS. α, Θ_X and P_{45} are calculated quantities as described in section 5.1.

Fig. 5.2 Plot of p_5 calculated from (5.10), vs. value of p_5 obtained from a Monte Carlo simulation of the experimental geometry, p_5 (MC).

Fig. 5.3 Two-dimensional spectrum of cross section vs. T_3, kinetic energy of one of the detected proton, for the symmetric angle pair 41.41° and $\Delta\Omega_3$ = 0.528 msr.

Fig. 5.4 Plot of momentum density Φ^2 vs. p_5(MC) for 41.41° symmetric angle pair and $\Delta\Omega_3$ = 0.528 msr. The curve is for Paris Φ^2.

Fig. 5.5 Spectrum of R = ($d^5\sigma$ (measured)/$d^5\sigma$ (Paris)) vs. T_3 for $\Delta\Omega_3$ = 0.0328 msr and 41.41° symmetric angle pair. The reduced solid angle favors the correlated pairs from p^1H.

Fig. 5.6 Plot of R vs. p_5 (MC) for the same data as in 5.4. The curve corresponds to the multiple scattering result, and shows that the net effect is a negative correction to the IA.

Fig. 5.7 Same as fig. 5.6 but for $\Delta\Omega_3$ = 0.107 msr.

Fig. 5.8 Same as fig. 5.4 but for asymmetric angle pair 30° - 53.75°.

Fig. 5.9 Same as fig 5.6, for geometry of fig. 5.8.

Fig. 5.10 Momentum density Φ^2 vs. p_5 (MC), for $\Delta\Omega_3$ = 0.528 msr and symmetric angle pair 44°. The dashed curve represents the correction due to rescattering and final state interaction, and the solid curve is the Paris Φ^2.

Fig. 5.11 Same as fig. 5.10, for the symmetric angle pair 38°.

Fig. 5.12 Same as fig. 5.10, for symmetric angle pairs 47°, 50° and 52°.

Fig. 5.13 Momentum density Φ^2 vs. calculated p_5, for $\Delta\Omega_3$ = 0.528 msr and asymmetric angle pairs 41.41° - 50°, 41.41° - 57° and 41.41° - 68°. The solid curve is for Φ^2 Paris. The dashed curves show the multiple scattering results.

Fig. 5.14 Same as fig. 5.13, for asymmetric angle pairs 30° - 44°, 30° - 61° and 30° - 68°.

Fig. 5.15 Same as fig. 5.13, for symmetric angle pairs 57° and 66°.

Fig. 5.16 Momentum density Φ^2 vs. minimum recoil momentum for all the symmetric angle pairs. The solid curve is Φ^2_{Paris}. The dashed curve is the multiple scattering result and the dashed-dot curve is for the calculation of "Δ" excitation.

Fig. 5.17 Spectrum of momentum density Φ^2 vs. recoil momentum p_5 from 0 to 100 MeV/c for our (p, 2p) data, the (e, e'p) data of Bernheim et al. (Be-81), and the (p, 2p) data of Witten et al (Wi-75). Solid curve represents the Paris Φ^2.

Fig. 5.18 The momentum distribution of the Reid soft-core (RSC) potential compared to the (e, e'p) data of ref. (Be-81), after correction for FSI, meson exchange current and isobar component by Arenhovel (figure 7 in Ar-82).

Fig. 5.19 Ratios of experiment to total theory based on RSC potential (from Ar-82, figure 5) for the data of (Be-81); kinematics I corresponds to the same n-recoil range as in figures 5.6, 5.7 and 5.9).

Fig. 5.20 Plot of Φ^2 vs. recoil momentum p_5 from 100 to 700 MeV/c. ○ corresponds to our asymmetric 41°-data, ✕ to our symmetric data at 47°, 50°, 52°, 57° and 66°, ◇ to (e, e'p) data of Bernheim et al., ✦ to (e, e'p) data of Mehnert (Me-85) and ✱ to (p, 2p) data of Witten et al. The solid curve is the Φ^2 Paris.

TABLE CAPTION

Tables 1 through 16 contain all the results of this experiment, that were analyzed at the College of William and Mary. In the Tables, T1 corresponds to beam energy. THETA3 and THETA4 are the angles with respect to the incident beam on LHS and RHS, respectively. $d\sigma_{CM}^{PP}$ is the elastic pp (on-shell) cross section. $\Delta\Omega_3$ and $\Delta\Omega_4$ are the solid angles defined by the ΔE_{B0} or ΔE_{B1} (1984) counters and by software cuts (1983) on LHS and by the ΔE_R counter on RHS. T3 is the kinetic energy of the detected proton on the LHS. KIN P5 is the p_5 calculated from eqn. (5.10). MC P5 is the p_5 obtained from the Monte Carlo simulation of the experimental geometry. $d^5\sigma$ is the measured five-fold differential cross-section and $d^5\sigma$ is the absolute statistical error. K is the kinematic factor. Φ^2 is the momentum space density and Φ^2 the corresponding absolute statistical error. Energies in MeV, momenta in Mev/c, solid angles in msr, $d^5\sigma$ in mb/sr^2MeV, $d\sigma_{CM}^{PP}$ in mb/sr, K in 10^6 MeV^2, Φ^2 in MeV^{-3}. Absolute uncertainties are statistical only.

TABLE 1

KINEMATICS, CROSS SECTION AND MOMENTUM DENSITY

T1=508.00 THETA3=41.54 THETA4=41.41

$d\sigma^{pp}_{cm}$ =3.440 $\Delta\Omega_3$=0.528 $\Delta\Omega_4$=1.188

T3	KIN P5	MC P5	$d^5\sigma$	$\Delta d^5\sigma$	E	ϕ^2	$\Delta\phi^2$
213.75	80.00	79.30	0.5423	0.0100	2.106	0.0750	0.0014
216.25	74.90	73.80	0.6915	0.0120	2.121	0.0951	0.0016
218.75	69.90	68.80	0.8668	0.0130	2.136	0.1184	0.0018
221.25	64.80	63.50	1.1450	0.0150	2.150	0.1554	0.0020
223.75	59.70	58.50	1.4710	0.0170	2.165	0.1983	0.0023
226.25	54.60	53.50	1.9310	0.0190	2.179	0.2585	0.0026
228.75	49.50	48.80	2.4260	0.0220	2.194	0.3227	0.0029
231.25	44.30	43.80	3.0460	0.0240	2.208	0.4025	0.0032
233.75	39.20	38.80	3.8860	0.0270	2.222	0.5102	0.0036
236.25	34.00	33.80	4.8750	0.0310	2.237	0.6316	0.0040
238.75	28.80	29.30	5.9490	0.0340	2.251	0.7713	0.0043
241.25	23.50	24.80	7.2070	0.0370	2.265	0.9283	0.0048
243.75	18.30	20.80	8.3750	0.0400	2.280	1.0720	0.0050
246.25	13.00	16.00	9.7200	0.0430	2.294	1.2370	0.0054
248.75	7.70	13.00	10.8600	0.0450	2.308	1.3730	0.0057
251.25	2.50	11.30	11.8780	0.0470	2.323	1.4930	0.0059
253.75	3.30	11.50	12.0480	0.0480	2.337	1.5040	0.0059
256.25	8.60	13.30	11.5630	0.0470	2.351	1.4350	0.0058
258.75	14.00	16.00	10.4670	0.0440	2.366	1.2920	0.0055
261.25	19.50	21.00	8.7590	0.0410	2.380	1.0740	0.0050
263.75	25.00	26.50	7.1750	0.0370	2.395	0.8745	0.0045
266.25	30.60	30.80	5.9460	0.0340	2.410	0.7201	0.0041
268.75	36.20	35.80	4.8190	0.0300	2.425	0.5803	0.0036
271.25	41.90	41.50	3.7530	0.0270	2.440	0.4491	0.0032
273.75	47.60	47.00	2.9100	0.0240	2.455	0.3461	0.0028
276.25	53.30	52.30	2.2660	0.0210	2.470	0.2679	0.0025
278.75	59.20	57.50	1.7380	0.0180	2.485	0.2043	0.0022
281.25	65.00	63.30	1.3400	0.0160	2.501	0.1564	0.0019
283.75	71.00	69.50	1.0190	0.0140	2.517	0.1182	0.0016
286.25	77.00	75.50	0.7810	0.0120	2.533	0.0900	0.0014

TABLE 2

KINEMATICS, CROSS SECTION AND MOMENTUM DENSITY

T1=508.00 THETA3=41.36 THETA4=41.41

$d\sigma^{pp}_{cm}$ =3.440 $\Delta\Omega_3$=0.107 $\Delta\Omega_4$=1.188

T3	KIN P5	MC P5	$d^5\sigma$	$\Delta d^5\sigma$	K	ϕ^2	$\Delta\phi^2$
216.25	76.30	75.00	0.75140	0.01500	2.112	0.1033	0.0021
223.75	61.10	59.70	1.54630	0.02200	2.156	0.2082	0.0030
231.25	45.80	44.80	3.00630	0.03100	2.198	0.3969	0.0041
238.75	30.30	30.10	5.91100	0.04300	2.241	0.7657	0.0055
245.00	17.30	18.60	9.11100	0.06500	2.277	1.1630	0.0081
250.00	6.70	11.80	11.13000	0.07200	2.305	1.4030	0.0092
253.75	1.50	10.80	13.06500	0.11000	2.326	1.6310	0.0140
256.25	6.80	12.00	13.34500	0.11200	2.340	1.6560	0.0140
258.75	12.20	14.80	11.28000	0.10200	2.355	1.3920	0.0130
262.50	20.40	21.50	8.53500	0.06300	2.376	1.0430	0.0074
267.50	31.50	31.40	5.93300	0.05300	2.405	0.7167	0.0064
272.50	42.80	42.10	3.76100	0.04200	2.435	0.4489	0.0050
277.50	54.20	53.30	2.30600	0.03300	2.465	0.2669	0.0040
283.75	68.80	67.80	1.18900	0.02000	2.503	0.1381	0.0023

TABLE 3

KINEMATICS, CROSS SECTION AND MOMENTUM DENSITY

T1=508.00 THETA3=30.13 THETA4=53.75

$\Delta\Omega_3$ =0.528 $\Delta\Omega_4$ =0.792

T3	KIN P5	MC P5	$d^5\sigma$	$\Delta d^5\sigma$	K	$d\sigma^{pp*}_{cm}$	ϕ^2	$\Delta\phi^2$
300.25	114.00	114.00	0.1066	0.0100	2.106	3.439	0.0148	0.0014
303.75	107.20	107.20	0.2050	0.0140	2.121	3.438	0.0283	0.0019
307.25	100.30	100.30	0.2301	0.0150	2.136	3.438	0.0316	0.0021
310.75	93.40	93.40	0.3251	0.0170	2.150	3.443	0.0443	0.0024
314.25	86.50	86.50	0.4680	0.0210	2.165	3.445	0.0633	0.0028
317.75	79.50	79.50	0.6417	0.0240	2.179	3.449	0.0862	0.0032
321.25	72.40	72.50	0.8516	0.0280	2.194	3.454	0.1135	0.0037
324.75	65.20	65.20	1.0512	0.0310	2.208	3.459	0.1390	0.0040
328.25	58.00	58.00	1.6100	0.0370	2.222	3.471	0.2109	0.0049
331.75	50.70	50.70	2.2769	0.0450	2.237	3.480	0.2957	0.0058
335.25	43.30	43.30	3.3996	0.0550	2.251	3.491	0.4376	0.0070
338.75	35.80	35.80	4.5205	0.0630	2.265	3.503	0.5763	0.0080
342.25	28.20	28.20	6.1969	0.0730	2.280	3.517	0.7788	0.0092
345.75	20.60	21.00	8.1962	0.0840	2.294	3.533	1.0236	0.0105
349.25	13.00	15.50	10.0597	0.0930	2.308	3.550	1.2426	0.0114
352.75	5.90	11.20	12.3843	0.1030	2.323	3.563	1.5148	0.0126
356.25	5.50	11.00	13.0267	0.1060	2.337	3.585	1.5733	0.0151
359.75	12.80	15.40	11.0899	0.0980	2.351	3.609	1.3218	0.0116
363.25	21.00	21.50	8.8162	0.0870	2.366	3.634	1.0363	0.0103
366.75	29.50	29.50	6.3952	0.0740	2.380	3.663	0.7470	0.0085
370.25	38.40	38.20	4.5309	0.0630	2.395	3.685	0.5176	0.0072
373.75	47.40	47.00	3.1422	0.0530	2.410	3.718	0.3530	0.0059
377.25	56.70	55.50	2.1003	0.0430	2.425	3.738	0.2327	0.0048
380.75	66.40	65.00	1.3530	0.0350	2.440	3.777	0.1470	0.0038
384.25	76.30	74.00	0.9518	0.0290	2.455	3.805	0.1016	0.0031
387.75	86.70	84.00	0.5850	0.0230	2.470	3.850	0.0610	0.0024
391.25	97.50	94.50	0.3599	0.0180	2.485	3.883	0.0367	0.0019
394.75	108.80	105.20	0.2614	0.0160	2.501	3.919	0.0260	0.0016

* TO CALCULATE , USED RENORMALISATION FACTOR 3.585/3.874

TABLE 4

KINEMATICS, CROSS SECTION AND MOMENTUM DENSITY

T1=508.00 THETA3=44.13 THETA4=44.00

$d\sigma^{PP}_{CM}$ =3.110 $\Delta\Omega_3$ =0.528 $\Delta\Omega_4$ =1.188

T3	KIN P5	MC P5	$d^5\sigma$	$\Delta d^5\sigma$	K	ϕ^2	$\Delta\phi^2$
221.25	84.10	82.00	0.5975	0.0260	2.285	0.0841	0.0037
223.75	79.60	77.00	0.7147	0.0290	2.303	0.0998	0.0040
226.25	75.20	73.00	0.8782	0.0310	2.320	0.1217	0.0043
228.75	71.00	69.50	1.0297	0.0340	2.338	0.1416	0.0046
231.25	66.90	64.50	1.2236	0.0360	2.356	0.1670	0.0050
233.75	63.10	61.00	1.5019	0.0400	2.374	0.2034	0.0054
236.25	59.50	57.00	1.7317	0.0430	2.392	0.2328	0.0057
238.75	56.30	54.50	2.0429	0.0460	2.410	0.2726	0.0062
241.25	53.40	52.00	2.2760	0.0480	2.428	0.3014	0.0064
243.75	51.10	49.50	2.5760	0.0510	2.446	0.3386	0.0067
246.25	49.30	48.00	2.7603	0.0520	2.464	0.3602	0.0069
250.00	47.90	46.75	2.9188	0.0370	2.492	0.3766	0.0049
253.75	47.90	46.50	2.8952	0.0530	2.519	0.3696	0.0068
256.25	48.80	49.00	2.8419	0.0530	2.538	0.3600	0.0067
258.75	50.50	50.50	2.5173	0.0490	2.557	0.3166	0.0062
261.25	52.90	53.00	2.2942	0.0470	2.576	0.2864	0.0059
263.75	55.80	55.00	2.0077	0.0440	2.595	0.2488	0.0054

TABLE 5

KINEMATICS, CROSS SECTION AND MOMENTUM DENSITY

T1=508.00 THETA3=38.13 THETA4=38.00

$d\sigma^{PP}_{CM}$ =3.710 $\Delta\Omega_3$ =0.528 $\Delta\Omega_4$=1.188

T3	KIN P5	MC P5	$d^5\sigma$	$\Delta d^5\sigma$	K	ϕ^2	$\Delta\phi^2$
218.75	80.10	79.50	0.5698	0.0340	1.955	0.0786	0.0045
221.25	76.80	77.00	0.6385	0.0350	1.966	0.0875	0.0047
223.75	73.50	73.00	0.7601	0.0380	0.977	0.1036	0.0051
226.25	70.40	70.50	0.8247	0.0390	1.987	0.1119	0.0052
228.75	67.50	67.50	0.9795	0.0410	1.995	0.1323	0.0055
231.25	64.80	65.00	1.1086	0.0440	2.008	0.1488	0.0058
233.75	62.20	62.00	1.1408	0.0440	2.018	0.1524	0.0058
236.25	59.90	60.00	1.2271	0.0460	2.029	0.1630	0.0059
238.75	57.90	57.50	1.4069	0.0480	2.039	0.1860	0.0063
241.25	56.20	56.30	1.5490	0.0500	2.049	0.2038	0.0066
243.75	54.80	55.00	1.6285	0.0520	2.059	0.2132	0.0067
246.25	53.70	53.80	1.6926	0.0520	2.069	0.2205	0.0068
248.75	53.10	53.00	1.8970	0.0550	2.079	0.2459	0.0071
251.25	52.80	52.00	1.8608	0.0540	2.089	0.2401	0.0069
253.75	53.00	52.50	1.7688	0.0530	2.099	0.2271	0.0067
256.25	53.60	53.00	1.8493	0.0540	2.109	0.2364	0.0068
258.75	54.70	53.80	1.7769	0.0530	2.119	0.2260	0.0067
261.25	56.10	55.00	1.5807	0.0500	2.128	0.2002	0.0062
263.75	57.90	56.30	1.6079	0.0500	2.138	0.2027	0.0062
266.25	60.00	59.50	1.3651	0.0460	2.148	0.1713	0.0058
268.75	62.50	61.00	1.3933	0.0470	2.157	0.1741	0.0058
271.25	65.30	63.00	1.1642	0.0430	2.167	0.1448	0.0053
273.75	68.30	67.00	0.9941	0.0390	2.177	0.1231	0.0048
276.25	71.60	70.00	0.8665	0.0370	2.186	0.1068	0.0045
278.75	75.10	73.00	0.7576	0.0340	2.196	0.0930	0.0042
281.25	78.80	76.30	0.6233	0.0320	2.206	0.0762	0.0038

TABLE 6

KINEMATICS, CROSS SECTION AND MOMENTUM DENSITY

T1=508.00 THETA3=47.13 THETA4=47.00

$\Delta\Omega_3$ =0.528 $\Delta\Omega_4$ =1.188

T3	KIN P5	MC P5	$d^5\sigma$	$\Delta d^5\sigma$	K	$d\sigma^{pp}_{cm}$	ϕ^2	$\Delta\phi^2$
215.00	137.80	135.80	0.07440	0.00810	2.395	2.710	0.01065	0.00130
220.00	130.60	128.50	0.09040	0.00850	2.440	2.690	0.01280	0.00140
225.00	124.20	122.00	0.10310	0.00920	2.485	2.660	0.01450	0.00140
230.00	118.60	116.50	0.14070	0.01000	2.531	2.650	0.01960	0.00160
235.00	114.00	112.00	0.17730	0.01200	2.577	2.630	0.02470	0.00170
240.00	110.60	108.80	0.19250	0.01200	2.623	2.630	0.02650	0.00170
247.50	108.30	106.40	0.22410	0.00920	2.695	2.630	0.02990	0.00180
255.00	109.10	107.60	0.20280	0.01200	2.770	2.620	0.02620	0.00170
260.00	111.80	111.00	0.18170	0.01100	2.822	2.620	0.02310	0.00150
265.00	116.10	115.25	0.16440	0.01100	2.876	2.630	0.02170	0.00140
270.00	122.10	121.25	0.12320	0.00920	2.932	2.650	0.01460	0.00130
275.00	129.60	128.50	0.09560	0.00810	2.992	2.680	0.01090	0.00100
280.00	138.50	137.50	0.08740	0.00780	3.055	2.720	0.00950	0.00100

TABLE 7

KINEMATICS, CROSS SECTION AND MOMENTUM DENSITY

T1=507.00 THETA3=50.00 THETA4=50.00

$\Delta\Omega_3$ =0.570 $\Delta\Omega_4$ =0.829

T3	KIN P5	MC P5	$d^5\sigma$	$\Delta d^5\sigma$	K	$d\sigma^{pp}_{cm}$	ϕ^2	$\Delta\phi^2$
207.50	201.00	200.00	0.00551	0.00068	2.460	2.250	0.00099	0.00012
214.50	192.00	192.00	0.00682	0.00071	2.540	2.200	0.00122	0.00013
221.50	185.00	184.00	0.00749	0.00075	2.620	2.150	0.00133	0.00013
228.50	179.00	178.00	0.00865	0.00079	2.680	2.150	0.00149	0.00014
235.50	176.00	175.00	0.01030	0.00084	2.770	2.150	0.00172	0.00014
242.50	174.00	173.00	0.01160	0.00088	2.860	2.100	0.00192	0.00015
249.50	174.00	172.50	0.01360	0.00096	2.940	2.100	0.00218	0.00015
256.50	177.00	175.00	0.01370	0.00095	3.035	2.150	0.00209	0.00014
263.50	183.00	181.00	0.01330	0.00095	3.140	2.150	0.00196	0.00014
270.50	192.00	188.00	0.01200	0.00088	3.230	2.200	0.00166	0.00012
277.50	203.00	201.00	0.01130	0.00087	3.380	2.250	0.00148	0.00011
284.50	218.00	213.80	0.00880	0.00078	3.540	2.300	0.00107	0.00009
291.50	236.00	231.30	0.00909	0.00082	3.720	2.400	0.00100	0.00009
298.50	259.00	253.70	0.00545	0.00064	3.960	2.530	0.00053	0.00006

TABLE 8

KINEMATICS, CROSS SECTION AND MOMENTUM DENSITY

T1=507.00 THETA3=52.00 THETA4=52.00

$\Delta\Omega_3$ =0.570 $\Delta\Omega_4$ =0.829

T3	KIN P5	MC P5	$d^5\sigma$	$\Delta d^5\sigma$	K	$d\sigma^{pp}_{cm}$	ϕ^2	$\Delta\phi^2$
214.50	235.00	233.00	0.00500	0.00061	2.640	1.950	0.00097	0.00012
221.50	229.00	228.00	0.00515	0.00058	2.740	1.950	0.00096	0.00011
228.50	225.00	224.00	0.00639	0.00067	2.825	1.900	0.00119	0.00012
235.50	223.00	221.50	0.00571	0.00062	2.920	1.900	0.00103	0.00011
242.50	223.00	222.00	0.00717	0.00070	3.020	1.900	0.00125	0.00012
249.50	225.00	225.00	0.00824	0.00074	3.120	1.900	0.00139	0.00012
256.50	230.00	228.00	0.00791	0.00073	3.240	1.950	0.00125	0.00011
263.50	237.00	235.00	0.00714	0.00069	3.390	2.000	0.00105	0.00010
270.50	248.00	245.50	0.00900	0.00076	3.540	2.000	0.00127	0.00011
277.50	262.00	257.50	0.00536	0.00063	3.730	2.050	0.00070	0.00008
284.50	279.00	277.00	0.00546	0.00064	3.965	2.200	0.00063	0.00007
291.50	302.00	299.00	0.00674	0.00071	4.320	2.350	0.00066	0.00007

TABLE 9

KINEMATICS, CROSS SECTION AND MOMENTUM DENSITY

T1=508.00 THETA3=41.54 THETA4=50.00

$\Delta\Omega_3$ =0.528 $\Delta\Omega_4$ =0.792

T3	KIN P5	$d^5\sigma$	$\Delta d^5\sigma$	K	$d\sigma^{pp}_{cm}$	ϕ^2	$\Delta\phi^2$
215.00	177.90	0.02370	0.00250	2.090	2.990	0.00379	0.00044
220.00	168.30	0.02680	0.00290	2.126	2.970	0.00423	0.00048
225.00	158.90	0.04060	0.00300	2.161	2.940	0.00639	0.00053
230.00	149.50	0.05060	0.00350	2.196	2.930	0.00785	0.00059
235.00	140.30	0.06530	0.00380	2.232	2.910	0.01003	0.00062
240.00	131.40	0.08690	0.00430	2.267	2.890	0.01330	0.00069
245.00	122.70	0.11590	0.00500	2.303	2.880	0.01750	0.00071
250.00	114.30	0.14480	0.00540	2.338	2.875	0.02150	0.00078
255.00	106.40	0.20800	0.00600	2.374	2.870	0.03050	0.00088
260.00	99.10	0.27300	0.00680	2.411	2.860	0.03960	0.00100
265.00	92.60	0.34240	0.00720	2.447	2.850	0.04910	0.00110
270.00	87.10	0.42350	0.00440	2.485	2.850	0.05980	0.00120
275.00	83.00	0.53060	0.00850	2.523	2.850	0.07370	0.00130
280.00	80.30	0.60710	0.00910	2.561	2.850	0.08320	0.00140
285.00	79.60	0.62730	0.00940	2.601	2.850	0.08460	0.00140

TABLE 10

KINEMATICS, CROSS SECTION AND MOMENTUM DENSITY

T1=508.00 THETA3=41.54 THETA4=57.00

$\Delta\Omega_3$=0.528 $\Delta\Omega_4$=0.792

T3	KIN P5	$d^5\sigma$	$\Delta d^5\sigma$	K	$d\sigma^{pp}_{cm}$	ϕ^2	$\Delta\phi^2$
215.00	262.70	0.01010	0.00190	2.012	2.690	0.00186	0.00039
220.00	253.50	0.00930	0.00210	2.051	2.650	0.00124	0.00036
225.00	244.50	0.00700	0.00190	2.090	2.610	0.00177	0.00048
230.00	235.60	0.00758	0.00240	2.129	2.575	0.00138	0.00045
235.00	227.00	0.00933	0.00320	2.169	2.545	0.00146	0.00051
240.00	218.40	0.01050	0.00160	2.208	2.510	0.00189	0.00051
245.00	210.20	0.00863	0.00130	2.248	2.485	0.00154	0.00051
250.00	202.00	0.01350	0.00210	2.289	2.455	0.00239	0.00064
255.00	194.30	0.01350	0.00220	2.330	2.435	0.00233	0.00058
260.00	186.90	0.01490	0.00200	2.371	2.415	0.00260	0.00054
265.00	180.00	0.02010	0.00230	2.413	2.395	0.00347	0.00059
270.00	173.50	0.02490	0.00240	2.455	2.375	0.00426	0.00054
275.00	167.60	0.03300	0.00250	2.499	2.360	0.00560	0.00054
280.00	162.40	0.03430	0.00260	2.543	2.350	0.00574	0.00054
285.00	158.00	0.04300	0.00300	2.589	2.350	0.00707	0.00052

TABLE 11

KINEMATICS, CROSS SECTION AND MOMENTUM DENSITY

T1=508.00 THETA3=41.54 THETA4=68.00

$\Delta\Omega_3$=0.528 $\Delta\Omega_4$=0.792

T3	KIN P5	$d^5\sigma$	$\Delta d^5\sigma$	K	$d\sigma^{pp}_{cm}$	ϕ^2	$\Delta\phi^2$
222.50	377.10	0.00241	0.00047	1.849	2.380	0.00055	0.00013
237.50	352.80	0.00261	0.00054	1.975	2.305	0.00057	0.00017
252.50	330.10	0.00359	0.00071	2.106	2.245	0.00068	0.00014
267.50	309.70	0.00466	0.00074	2.245	2.185	0.00095	0.00017
282.50	292.50	0.00360	0.00050	2.395	2.160	0.00069	0.00014

TABLE 12

KINEMATICS, CROSS SECTION AND MOMENTUM DENSITY

T1=508.00 THETA3=30.13 THETA4=44.00

$\Delta\Omega_3$ =0.528 $\Delta\Omega_4$ =0.792

T3	KIN P5	$d^5\sigma$	$\Delta d^5\sigma$	K	$d\sigma^{PP}_{CM}$	ϕ^2	$\Delta\phi^2$
309.00	71.70	0.70900	0.01800	1.910	3.744	0.09910	0.00250
316.00	68.05	0.83020	0.01900	1.926	3.745	0.11510	0.00270
323.00	66.65	0.89920	0.02000	1.941	3.748	0.12360	0.00280
330.00	67.80	0.87060	0.02000	1.956	3.754	0.11860	0.00280
335.25	70.30	0.81650	0.02800	1.968	3.759	0.11040	0.00380
340.50	74.40	0.63890	0.01700	1.979	3.767	0.08570	0.00250
347.50	81.70	0.49000	0.01600	1.995	3.779	0.06500	0.00230
354.50	91.10	0.38100	0.01500	2.013	3.794	0.04990	0.00210
361.50	102.20	0.24590	0.01200	2.031	3.881	0.03180	0.00180
368.50	114.90	0.17260	0.00980	2.053	3.831	0.02260	0.00160
375.50	129.30	0.11320	0.00840	2.080	3.852	0.01420	0.00130
382.50	145.30	0.00767	0.00720	2.114	3.874	0.00937	0.00110
389.50	163.30	0.05097	0.00510	2.163	3.897	0.00606	0.00090
396.50	183.90	0.03586	0.00420	2.238	3.919	0.00410	0.00060

TABLE 13

KINEMATICS, CROSS SECTION AND MOMENTUM DENSITY

T1=508.00 THETA3=30.13 THETA4=61.00

$\Delta\Omega_3$ =0.528 $\Delta\Omega_4$ =0.792

T3	KIN P5	$d^5\sigma$	$\Delta d^5\sigma$	K	$d\sigma^{PP}_{CM}$	ϕ^2	$\Delta\phi^2$
302.00	169.00	0.02284	0.00330	1.926	3.091	0.00384	0.00070
309.00	155.60	0.03272	0.00430	1.956	3.101	0.00540	0.00080
316.00	142.20	0.05288	0.00540	1.987	3.111	0.00856	0.00110
323.00	128.80	0.08291	0.00660	2.017	3.132	0.01312	0.00120
330.00	115.50	0.12560	0.00740	2.048	3.161	0.01938	0.00130
337.00	102.50	0.22470	0.01000	2.079	3.199	0.03378	0.00180
344.00	90.10	0.38140	0.01300	2.111	3.246	0.05562	0.00210
351.00	78.70	0.65020	0.01700	2.144	3.302	0.09179	0.00260
358.00	69.20	0.94370	0.02000	2.178	3.369	0.12850	0.00300
365.00	62.80	1.36510	0.02300	2.215	3.448	0.17870	0.00330
372.00	61.10	1.47140	0.02400	2.256	3.536	0.18450	0.00330
379.00	65.40	1.32470	0.02300	2.301	3.637	0.15840	0.00300
386.00	75.40	0.87020	0.01800	2.355	3.748	0.09880	0.00230
393.00	90.50	0.44870	0.01300	2.424	3.869	0.04800	0.00160
400.00	109.90	0.21280	0.00940	2.516	3.999	0.02130	0.00100

TABLE 14

KINEMATICS, CROSS SECTION AND MOMENTUM DENSITY

T1=508.00 THETA3=30.13 THETA4=68.00

$\Delta\Omega_3$ =0.528 $\Delta\Omega_4$ =0.792

T3	KIN P5	$d^5\sigma$	$\Delta d^5\sigma$	K	$d\sigma^{pp}_{CM}$	ϕ^2	$\Delta\phi^2$
307.25	220.00	0.00789	0.00180	1.889	2.799	0.00149	0.00040
317.25	201.10	0.01135	0.00220	1.942	2.837	0.00211	0.00050
328.25	182.30	0.01473	0.00240	1.995	2.897	0.00254	0.00050
338.75	164.40	0.02537	0.00320	2.050	2.983	0.00413	0.00060
347.50	150.40	0.05261	0.00520	2.098	3.074	0.00814	0.00090
354.50	140.20	0.06147	0.00530	2.137	3.162	0.00912	0.00090
361.50	131.40	0.09946	0.00710	2.179	2.264	0.01400	0.00110
368.50	124.50	0.13870	0.00750	2.225	3.380	0.01840	0.00110
375.50	120.00	0.16140	0.00860	2.275	3.511	0.02020	0.00110
382.50	118.90	0.16800	0.00870	2.332	3.656	0.01970	0.00095
389.50	121.80	0.16050	0.00850	2.401	3.817	0.01750	0.00088
396.50	129.60	0.11510	0.00710	2.490	3.992	0.01160	0.00069

TABLE 15

KINEMATICS, CROSS SECTION AND MOMENTUM DENSITY

T1=507.00 THETA3=57.00 THETA4=57.00

$\Delta\Omega_3$ =0.570 $\Delta\Omega_4$ =0.829

T3	KIN P5	$d^5\sigma$	$\Delta d^5\sigma$	K	$d\sigma^{pp}_{cm}$	ϕ^2	$\Delta\phi^2$
202.00	367.00	0.00102	0.00024	2.684	1.900	0.00020	0.00005
209.00	364.00	0.00119	0.00022	2.807	1.880	0.00022	0.00004
219.50	362.00	0.00190	0.00022	3.015	1.880	0.00033	0.00004
230.00	365.00	0.00181	0.00031	3.259	1.900	0.00029	0.00005
237.00	369.00	0.00213	0.00032	3.459	1.930	0.00032	0.00005
244.00	377.00	0.00167	0.00026	3.709	2.000	0.00023	0.00003
251.00	389.00	0.00185	0.00034	4.050	2.100	0.00022	0.00004
258.00	406.00	0.00272	0.00033	4.582	2.200	0.00027	0.00003

TABLE 16

KINEMATICS, CROSS SECTION AND MOMENTUM DENSITY

T1=507.00 THETA3=66.00 THETA4=66.00

$\Delta\Omega_3$ =0.570 $\Delta\Omega_4$ =0.829

T3	KIN P5	$d^5\sigma$	$\Delta d^5\sigma$	K	$d\sigma^{pp}_{cm}$	ϕ^2	$\Delta\phi^2$
129.00	658.00	0.00161	0.00039	1.598	3.250	0.00031	0.00007
135.00	654.00	0.00235	0.00042	1.698	3.200	0.00043	0.00008
141.00	651.00	0.00202	0.00044	1.809	3.150	0.00035	0.00008
150.00	649.00	0.00246	0.00032	2.009	3.130	0.00039	0.00005
159.00	650.00	0.00238	0.00043	2.267	3.150	0.00033	0.00006
165.00	654.00	0.00235	0.00042	2.517	3.200	0.00021	0.00005
171.00	661.00	0.00218	0.00048	2.911	3.280	0.00023	0.00005
177.00	674.00	0.00273	0.00052	3.793	3.400	0.00029	0.00004

VITA

Vina Alkesh Punjabi

Born in Gujarat, India, March 17, 1952. Graduated from high school in Gandevi, Gujarat, India in 1967. Received B.Sc. with distinction in June 1971 and M.Sc. in June 1973 from Gujarat University with a major in Physics.

In January 1980, the author started graduate study at the College of William and Mary in the Department of Physics, with a graduate assistantship. Received M.S. in Physics in May 1983 from the College of William and Mary. She is currently employed as a Research Associate in the Physics Department, College of William and Mary.